DEMONSTRATION OF A NOVEL LONGITUDINAL PHASE SPACE LINEARIZATION METHOD

Dissertation
zur Erlangung des Doktorgrades
an der Fakultät für Mathematik, Informatik und Naturwissenschaften
Fachbereich Physik
der Universität Hamburg

vorgelegt von

Ryan David Stark

Hamburg

2021

Gutachter der Dissertation:	Prof. Dr. Florian Grüner Prof. Dr. Wolfgang Hillert
Zusammensetzung der Prüfungskommission:	Prof. Dr. Günter Sigl Prof. Dr. Florian Grüner Prof. Dr. Wolfgang Hillert Dr. Klaus Flöttmann Dr. Jens Osterhoff
Vorsitzende/r der Prüfungskommission:	Prof. Dr. Günter Sigl
Datum der Disputation:	12.04.2021
Vorsitzender des Promotionsausschusses:	Prof. Dr. Günter Sigl
Leiter des Fachbereichs PHYSIK:	Prof. Dr. Wolfgang Hansen
Dekan der Fakultät MIN:	Prof. Dr. Heinrich Graener

EIDESSTATTLICHE VERSICHERUNG / DECLARATION ON OATH

Hiermit versichere ich an Eides statt, die vorliegende Dissertationsschrift selbst verfasst und keine anderen als die angegebenen Hilfsmittel und Quellen benutzt zu haben. Die eingereichte schriftliche Fassung entspricht der auf dem elektronischen Speichermedium. Die Dissertation wurde in der vorgelegten oder einer ähnlichen Form nicht schon einmal in einem früheren Promotionsverfahren angenommen oder als ungenügend beurteilt.

Hamburg, 15.02.2021

Ryan David Stark

ABSTRACT

The attainability of ultrashort electron bunches with extremely small longitudinal extent is crucial in many modern particle accelerator applications, such as free electron lasers and time-resolved electron diffraction, aimed at the studying ultrafast structural dynamics of matter. Whilst free-electron lasers require GeV electron beams with high peak currents to produce brilliant X-ray radiation for this purpose, ultrafast electron diffraction constitutes an alternative method where bunches with ultralow charge below 100 fC and comparatively low energy in the range of a few MeV are used to probe the sample. In this case, a high beam quality with ultralow transverse emittance and ultrashort bunch length on the femtosecond scale is also required.

The Relativistic Electron Gun for Atomic Exploration (REGAE), located at the Deutsches Elektronen-Synchrotron (DESY) in Hamburg and constructed in cooperation between the Max-Planck Society, the University of Hamburg and DESY, is a conventional ~ 5 MeV electron accelerator designed to deliver unique beam parameters which meet the demanding requirements of time-resolved electron diffraction experiments. The REGAE beamline also serves as a test facility for various accelerator-related concepts regarding diagnostic devices and beam dynamics studies. A unique radio frequency (rf) transverse deflecting structure with minimal level of aberrations in the deflecting fields and improved rf efficiency was installed at REGAE for the diagnostics of longitudinal properties of the electron bunch.

At REGAE, a compression of the electron bunches down to the ten femtosecond range can be achieved with the ballistic bunching mechanism. This method is feasible at low beam energies in the range of a few MeV. Apart from space charge effects, nonlinear contributions in the longitudinal phase space distribution can impose a decisive limit on the achievable bunch length compression. To overcome this problem, many large scale facilites such as the European XFEL and FLASH at DESY employ a dedicated higher harmonic cavity to linearize the longitudinal phase space. A novel linearization method, which is based on the controlled expansion of the electron bunch between cavities operated at the same fundamental frequency, has previously been developed. The concept does not require any further beamline components and is not limited to the compression of the bunch, but can also be applied to the energy coordinate of the longitudinal phase space.

A standard procedure for performing bunch length measurements is established and measurement data of the ballistic bunching mechanism are presented. Experimental results of this work confirm that the initial energy spread arising from rf curvature in the electron gun can be compensated, thus producing a quasi-monoenergetic beam which may be of particular interest in transmission electron microscopy applications. Measurement data obtained at the REGAE beamline which successfully demonstrate the applicability of the novel linearization concept are presented.

ZUSAMMENFASSUNG

Die Erzeugung von ultrakurzen Elektronenpaketen ist von ausschlaggebender Bedeutung bei diversen modernen Beschleunigeranwendungen, wie z.B. freie Elektronen-Laser und zeitaufgelöste Elektronendiffraktion, welche der Analyse der Strukturdynamik von Materie dienen. Während freie Elektronen-Laser GeV Strahlenergien mit hohem Spitzenstrom benötigen, um brillante Röntgenstrahlung für diese Zwecke zu erzeugen, werden in ultraschneller Elektronendiffraktion Elektronenpakete mit ultrakleiner Ladung unter 100 fC und vergleichsweise niedriger Energie im MeV-Bereich verwendet. In diesem Fall ist eine hohe Strahlqualität mit ultrakleiner Emittanz und ultrakurzen Elektronenpaketen im Femtosekunden-Bereich erforderlich.

Die Relativistic Electron Gun for Atomic Exploration (REGAE) am Deutschen Elektronen-Synchrotron (DESY) in Hamburg, konstruiert in einer Kooperation zwischen der Max-Planck Gesellschaft, der Universität Hamburg und DESY, ist ein konventioneller ~ 5 MeV Elektronenbeschleuniger, welcher die für zeitaufgelöste Elektronendiffraktion notwendigen besonderen Strahlparameter zur Verfügung stellt. REGAE dient auch der Untersuchung diverser Konzepte und Entwicklungen in Bezug auf Diagnostikelementen und Studien zu Strahldynamik. Eine speziell gefertigte hochfrequente (hf) transversal ablenkende Struktur mit minimalem Maß an Aberrationen in den ablenkenden Feldern und verbesserter HF-Effizienz wurde zur Charakterisierung longitudinaler Eigenschaften der Elektronenpakete bei REGAE eingebaut.

Bei REGAE wird die Kompression der Elektronenpakete bis in den zehn Femtosekunden Bereich mittels des "ballistic bunching" Mechanismus erzielt. Dies ist möglich aufgrund der niedrigen Strahlenergie im Bereich von einigen MeV. Nebst Raumladungseffekten können Nichtlinearitäten im longitudinalen Phasenraum die erreichbare Kompression entscheidend begrenzen. Große Beschleunigeranlagen wie der European XFEL und FLASH am DESY nutzen typischerweise höherharmonische Kavitäten um den longitudinalen Phasenraum zu linearisieren. Die dieser Arbeit vorangehende Entwicklung einer neuartigen Methode zur Linearisierung des longitudinalen Phasenraums basiert auf der kontrollierten Expansion der Elektronenpakete zwischen den Kavitäten, welche mit der gleichen Frequenz betrieben werden. Dieses Konzept ist nicht nur auf die Kompression der Elektronenpakete beschränkt, sondern kann auch auf die Energie-Koordinate des longitudinalen Phasenraums angewendet werden.

Eine Standardprozedur zur Vermessung der Länge der Elektronenpakete wurde etabliert und Messdaten zum "ballistic bunching" Mechanismus werden präsentiert. Experimentelle Befunde dieser Arbeit bestätigen, dass die initiale Energiebreite aufgrund der Feldkrümmung in der Elektronen-Gun kompensiert werden kann und somit ein quasi-monoenergetischer Elektronenstrahl produziert wird, für den Transmissionselektronenmikroskopie ein potentieller Anwendungsbereich ist. Bei REGAE aufgenommene Messdaten, welche die Anwendung der neuartigen Linearisierungsmethode demonstrieren, werden präsentiert.

CONTENTS

LIST OF FIGURES

LIST OF TABLES

1 INTRODUCTION

Many modern particle accelerator applications require high quality electron beams with precise tuning of the longitudinal beam parameters. The production of ultrashort electron bunches on the femtosecond scale is crucial for accelerator-based research experiments such as free-electron lasers (FELs) [1] and ultrafast electron diffraction (UED) [2, 3]. While FELs incorporate undulator magnets to produce high brightness X-ray beams, UED facilities directly use the electron beam to probe sample material. Ultimately, the objective is to gain further insights into atomic processes by observing the atomic motion on according timescales, thus effectively "making a molecular movie" [4]. While low energy diffractometers employing electron beam energies around 100 keV do exist [5], the necessity of achieving higher performances by reducing space charge effects has given rise to research facilities operating at energies of a few MeV [6]. The Relativistic Electron Gun for Atomic Exploration (REGAE), located at the Deutsches Elektronen-Synchrotron (DESY) is an example for such an accelerator beamline [7]. All measurements presented in the course of this thesis were carried out at the REGAE accelerator.

Since the longitudinal characteristics of the electron bunch are crucial to the success of such experiments, the measurement of these properties is of great importance. The reconstruction of the longitudinal phase space quantities can be carried out with a transverse deflecting structure (TDS) [8]. Upon passage through a TDS, the electron bunch is sheared in the transverse direction. Each particle receives a transverse kick dependent on its longitudinal position within the bunch. Thus, the longitudinal coordinate is mapped to a transverse coordinate and the longitudinal extent of the electron bunch becomes easily accessible. A uniquely designed TDS has been installed in the REGAE beamline [9]. By combining the TDS with an energy spectrometer, the longitudinal phase space can be imaged on a subsequent detector screen.

As experimental prerequisites continue to call for an ever decreasing longitudinal extent of the particle bunches, the exigency of performing reliable bunch length measurements compulsorily increases. Not only is the bunch length linked to the temporal resolution of a given experimental setup, but in order to further push the boundaries and produce even shorter bunches, an understanding of the current limitations is indispensable.

In principle, the minimum electron bunch length which can be achieved in an accelerator is dictated by space charge repulsion. However, nonlinear correlations in the longitudinal phase space distribution may also limit the attainable bunch compression [10]. Similar limitations apply to experiments which demand bunches with a small energy spread instead of a small longitudinal extent. For instance, the resolution in transmission electron microscopy experiments, which call for a transversely focused beam on the respective target, is governed by the existing energy spread combined with chromatic aberrations when using a long

bunch [11, 12]. Nonlinearities arising from the curvature of the accelerating field in the gun cavity limit the minimum achievable energy spread. A linearization of the phase space distribution is needed in order to overcome these constraints.

While large research facilities such as the European XFEL [13] and FLASH [14] at DESY employ a dedicated higher harmonic cavity to combat these undesired nonlinearities, this approach can entail high financial costs due to the complementary higher harmonic radio frequency (rf) system [15]. A novel method geared towards the linearization of the longitudinal phase space without the use of higher harmonics has been proposed in [16, 17]. This method is based on the controlled expansion of the bunch between two accelerating cavities operated at the same fundamental rf frequency, and is denoted as *stretcher mode*. The stretcher mode can be applied to both axes of the longitudinal phase space, thus further reducing either the longitudinal extent (bunch compression scheme) or the energy spread (energy spread compensation scheme) of the bunch.

The general applicability of this novel linearization concept has been experimentally demonstrated in the course of this thesis. A successful linearization in context of the energy spread compensation scheme has been accomplished. Similar results have been gathered for the bunch compression scheme. In both cases, first and second order contributions in the longitudinal phase space distribution have effectively been eliminated.

Section 2 of this thesis presents an outline of linear transverse beam dynamics in a charged particle accelerator. Longitudinal bunch dynamics are also discussed, along with beam dynamics in a transverse deflecting structure. A full description of the REGAE beamline is given in section 3. The TDS itself is described more thoroughly in section 4, which also includes experimental procedures and results of bunch length measurements performed with the TDS.

In section 5, the basic features of the stretcher mode are outlined and experimental findings obtained for the operation of REGAE using stretcher mode are presented. Both bunch compression and energy spread compensation scheme were verified as a valid linearization approach. Results depicting the linearized longitudinal phase space, where the curvature of the distribution has vanished, are shown explicitly.

A final discussion of the results is given in section 6.

1.1 REGAE

The core of this Ph.D. thesis is centered around REGAE [7, 18], located at the DESY complex in Hamburg. The REGAE beamline is a conventional linear accelerator designed to produce ultra-short electron bunches with low charge. Initially, the unique beam parameters of REGAE were intended to perform UED experiments [6], which were conducted by the group of Prof. Dr. R. J. D. Miller.

REGAE is a conventional machine which includes two rf structures, namely the electron gun cavity and the buncher cavity. A laser pulse shines on the photo cathode in the gun cavity and thus produces an electron bunch, which is accelerated to a maximum of 5 MeV in the rf resonator. The buncher cavity is located about 1.5 m behind the gun and imposes a correlated energy spread on

the electron distribution. Due to this energy spread, the electrons in the back are accelerated, while the electrons in the front are decelerated. Thus, the electron bunch is compressed. This method of bunch compression is known as the ballistic bunching mechanism [10, 19]. No mean energy is gained by the bunch in the buncher cavity. Bunch lengths below 10 fs have been measured using the ballistic bunching mechanism at the Pegasus laboratory at the University of California [20].

The REGAE accelerator is typically operated at low bunch charges around 100 fC. Machine operation at low charge values reduces space charge effects, which allows for a small spot size of the laser pulse on the cathode. The electron beam then has a very low transverse emittance, which leads to a large transverse coherence [6]. Together with the short bunch length, the high single shot quality makes REGAE a highly suitable machine for UED experiments [6, 7].

In addition to a multiplicity of low charge electron beam diagnostics, a transverse deflecting structure was was specifically designed for REGAE and installed in the beamline [9]. The TDS was utilized for bunch length measurements and for imaging the longitudinal phase space to study the stretcher mode linearization concept in the course of this Ph.D. thesis.

1.2 ASTRA

The program package ASTRA (A Space Charge Tracking Algorithm) was used as a simulation tool. ASTRA is a numerical code written in Fortran 90 and developed at DESY [21]. Within ASTRA, the user has the option to define and adjust external electromagnetic fields, along with a variety of other options [22]. These elements are taken into account upon propagation of the simulated particles through the specified beamline. Additionally, space charge effects arising from the Coulomb interaction between individual particles in the bunch may be incorporated into the simulation.

The actual tracking of the particles is based on a 4th order non-adaptive Runge-Kutta integration [22]. At each time step, the motion of the particles and the forces acting on them is calculated. For the calculation of space charge effects, the user can choose between a cylindrical symmetric algorithm or a full three-dimensional calculation. The three-dimensional calculation requires a greater number of macro-particles. This is necessary in order to avoid statistical problems. Furthermore, an advantage of the cylindrical algorithm is that mirror charges arising during the electron emission from the cathode are taken into account. Therefore, the cylindrical algorithm was used for simulations with space charge effects.

By importing external data files containing (measured) field maps, simulations of arbitrary beamlines containing user-specified elements can be performed.

2 FUNDAMENTALS

In this section, an overview of the fundamental physics required for this work is presented. A basic introduction into linear beam dynamics and the general description of particles in a bunch is given in the first part of this section. The second part features a brief outline on longitudinal beam dynamics. Both of these parts are based on [23, 24, 25]. Finally, the last part of this section contains a summary of beam dynamics in a transverse deflecting structure, which is essential for the bunch length measurements presented in the course of this thesis.

2.1 LINEAR BEAM DYNAMICS

It is common practice to describe the motion of a particle in the bunch with respect to the reference particle. The reference particle propagates along the design trajectory of the machine. Since REGAE is a linear accelerator, the design trajectory in absence of deflecting electromagnetic fields is a straight line and chosen to coincide with the z-axis of the coordinate system. It should be noted that the term "linear beam dynamics" refers to a theoretical formalism which only deals with linear manipulations of the particle beam. In general, a given particle in a bunch is characterized by its six-dimensional phase space vector

$$\vec{u} = \begin{pmatrix} x & p_x & y & p_y & \zeta & p_z \end{pmatrix}^{\mathrm{T}}, \tag{2.1}$$

where x is the horizontal and y vertical distance to the design trajectory along the z-axis, p_x and p_y are the corresponding momenta and the longitudinal coordinates ζ and p_z are given with respect to the longitudinal position and momentum of the reference particle. More specifically, the longitudinal coordinate ζ is given by the Galilean transformation $\zeta = z - ct$ to the co-moving frame of the reference particle. The reference particle corresponds to the center of the bunch at $\zeta = 0$. For beamline sections in which the energy is constant, the transverse components of the particle momentum $\vec{p}$ can be approximated by $p_x \approx |\vec{p}|x'$ and $p_y \approx |\vec{p}|y'$, where the divergences are given by the derivatives $x' = \mathrm{d}x/\mathrm{d}z$ and $y' = \mathrm{d}y/\mathrm{d}z$. Typically, the divergence values x' and y' are very small. The phase space vector is often given using the divergences instead of the actual momenta:

$$\vec{u} = \begin{pmatrix} x & x' & y & y' & \zeta & \delta p \end{pmatrix}^{\mathrm{T}}. \tag{2.2}$$

Here $\delta p = (|\vec{p}| - |\vec{p}_r|)/|\vec{p}_r|$ is the relative deviation between $\vec{p}$ and the momentum of the reference particle $\vec{p}_r$.

Any element in the beamline of a particle accelerator has an influence on the values of $\vec{u}$. For example, a free drift section leads to a shift in the transverse position of a particle, whereas a focusing element approximated as a thin lens will alter x' or y'. Each beamline component can be associated with a respective

transfer matrix $\mathcal{M}_i$. In linear beam dynamics, the equations of motion for a particle propagating through a beamline are solved by

$$\vec{u} = \mathcal{M} \cdot \vec{u_0}, \tag{2.3}$$

where $\vec{u_0}$ is the phase space vector at an initial position s_0, $\vec{u}$ denotes the phase space vector at an arbitrary final position s and the total transfer matrix $\mathcal{M}$ describes the propagation of the particle from z_0 to z. If multiple beamline components are considered along the propagation path, $\mathcal{M}$ is simply given by

$$\mathcal{M} = \prod_{i=1}^{n} \mathcal{M}_i. \tag{2.4}$$

If the motion of the particle in the transverse planes is assumed to be decoupled, the full transfer matrix simplifies to

$$\mathcal{M}_{\text{decoupled}} = \begin{pmatrix} \mathcal{M}_{11} & \mathcal{M}_{12} & 0 & 0 & 0 & \mathcal{M}_{16} \\ \mathcal{M}_{21} & \mathcal{M}_{22} & 0 & 0 & 0 & \mathcal{M}_{26} \\ 0 & 0 & \mathcal{M}_{33} & \mathcal{M}_{34} & 0 & \mathcal{M}_{36} \\ 0 & 0 & \mathcal{M}_{43} & \mathcal{M}_{44} & 0 & \mathcal{M}_{46} \\ \mathcal{M}_{51} & \mathcal{M}_{52} & \mathcal{M}_{53} & \mathcal{M}_{54} & \mathcal{M}_{55} & \mathcal{M}_{56} \\ 0 & 0 & 0 & 0 & 0 & \mathcal{M}_{66} \end{pmatrix}. \tag{2.5}$$

For this type of decoupled dynamics, the transverse equation of motion takes on the form

$$\frac{\mathrm{d}^2 x(z)}{\mathrm{d}z^2} + K_x(z)x(z) = 0, \tag{2.6}$$

with the magnet parameter $K_x(z)$, which can be used to describe the effect of deflecting and focusing/defocusing magnetic elements installed for the purpose of guiding the electron beam through the beamline with desired beam parameters. The above equation assumes that all particles propagate with the same momentum. The solution of equation 2.6 can be written as

$$\begin{pmatrix} x \\ x' \end{pmatrix} = \mathcal{M}_x \begin{pmatrix} x_0 \\ x'_0 \end{pmatrix} \tag{2.7}$$

with the transfer matrix [24]

$$\mathcal{M}_x = \begin{pmatrix} \cos\left(\sqrt{K_x(z)}z\right) & \frac{1}{\sqrt{K(z)}} \sin\left(\sqrt{K_x(z)}z\right) \\ -\sqrt{K_x(z)} \sin\left(\sqrt{K_x(z)}z\right) & \cos\left(\sqrt{K_x(z)}z\right) \end{pmatrix}. \tag{2.8}$$

Naturally, equation 2.8 also holds true for y and y'. It should be noted that a positive K corresponds to a focusing magnet, whereas a negative K leads to hyperbolic functions in equation 2.8 and describes a defocusing magnet.

In a free drift section of length L, $K_x(z) = 0$ holds true, which yields the transfer matrix

$$\mathcal{M}_{x,\text{drift}} = \begin{pmatrix} 1 & L \\ 0 & 1 \end{pmatrix}. \tag{2.9}$$

Using the thin lens approximation for a focusing magnet, the transfer matrix is given by [26]

$$\mathcal{M}_{x,\mathrm{f}} = \begin{pmatrix} 1 & 0 \\ -\frac{1}{f} & 1 \end{pmatrix}, \tag{2.10}$$

where f is the focal length of the magnet. The underlying approximation of equation 2.10 is valid if the focal length is much longer than the length of the magnet. In this case, the position of the particle inside the magnet remains constant.

For the description of an accelerator beamline, the following ansatz is commonly made [24]: the beamline is separated into segments with $K(z) = \text{const.}$ and the full transfer matrix is then pieced together by matrix multiplication according to equation 2.4. If a beamline element is characterized by $K(z) \neq \text{const.}$, it is possible to split the element into small slices where $K(z) = \text{const.}$ holds true. This procedure is only possible because the equation of motion as written in equation 2.6 is linear.

The formalism introduced above is applicable to the description of the motion of a single particle. In order to extend this description to a generalized ensemble of particles with an arbitrary distribution, not only the motion of individual particles but more importantly the quantities related to the evolution of the entire ensemble must be considered. This can be achieved with the help of the first moment and the second central moment of the given distribution. For a continuous normalized distribution $f(x)$ of a variable x with $x, f(x) \in \mathbb{R}$, the first raw moment μ_1' is equal to the mean and defined as

$$\mu_1' = \int_{-\infty}^{\infty} x f(x) \mathrm{d}x. \tag{2.11}$$

The mean is identical to the expected value of x. A feasible method of indicating the width of a distribution is the RMS-value[1] x_{RMS}, which is connected to the second central moment μ_2 via $x_{\mathrm{RMS}} = \sqrt{\mu_2}$. The second central moment itself can be written as

$$\mu_2 = \int_{-\infty}^{\infty} \left(x - \mu_1'\right)^2 f(x) \mathrm{d}x = \int_{-\infty}^{\infty} x^2 f(x) \mathrm{d}x - \left(\int_{-\infty}^{\infty} x f(x) \mathrm{d}x \right)^2 \tag{2.12}$$

and is also referred to as the variance $\mathrm{var}(x)$ of a distribution. From this point forward in this thesis, the operators $\langle \cdot \rangle$ and $\langle \cdot^2 \rangle$ mark the calculation of the mean and of the second central moment, respectively. In addition to this, the covariance $\mathrm{cov}(x, y) = \langle xy \rangle$ for two variables x and y is defined as

$$\langle xy \rangle = \int_{-\infty}^{\infty} \int_{-\infty}^{\infty} xy f(x,y) \mathrm{d}x \mathrm{d}y - \int_{-\infty}^{\infty} x f(x,y) \mathrm{d}x \int_{-\infty}^{\infty} y f(x,y) \mathrm{d}y. \tag{2.13}$$

It follows that $\mathrm{cov}(x, x) = \mathrm{var}(x)$. Alternatively, equations 2.11 and 2.12 may also be formulated for a discrete distribution, where N denotes the number of entries in the given sample:

$$\langle x \rangle = \frac{\sum_{i=1}^{N} x_i}{N} \tag{2.14a}$$

1 Root Mean Square.

$$\langle x^2 \rangle = \frac{\sum_{i=1}^{N} x_i^2}{N} - \left(\frac{\sum_{i=1}^{N} x_i}{N} \right)^2 . \tag{2.14b}$$

This is especially useful when dealing with pixel detectors, where the generated output is discrete.

2.1.1 Beam Emittance

As mentioned previously in section 2.1, each particle in the bunch can be described by its phase space vector as defined in equation 2.1. The complete particle bunch occupies a certain area in the six-dimensional phase space where each particle may be marked by a point. According to Liouville's theorem [27], the phase space distribution function is an invariant of motion, i.e. the point density around a given point which propagates through the six-dimensional phase space is constant over time. Due to the fact that Liouville's theorem is valid for any arbitrary subset of particles, it can be applied to the entire particle bunch. Since the number of particles in the bunch can be assumed to be constant throughout the beamline, this means that the phase space volume occupied by the bunch also remains constant. Liouville's theorem is only valid for Hamiltonian systems where the interactions between particles are neglected [28]. For N particles in a bunch, this means that

$$\int_{\mathbb{R}^6} N \mathrm{d}x \mathrm{d}y \mathrm{d}\zeta \mathrm{d}p_x \mathrm{d}p_y \mathrm{d}p_z = \text{const.} \tag{2.15}$$

holds true.

The emittance ϵ of a beam can be defined as a measure of the phase space volume:

$$\epsilon := \frac{\text{phase space volume}}{\pi}. \tag{2.16}$$

While it is possible to simply include all particles to calculate the phase space volume and thus define a "100 % emittance" ϵ_{100}, this may prove to be problematic if the phase space distribution of the bunch is irregular and contains irregular tails, as these would dominate the calculation of ϵ_{100} [23]. A more reliable and robust definition of the phase space volume is based on the use of statistical moments. These are often summarized in the beam matrix Σ_{beam}, which is given by

$$\Sigma_{\text{beam},jk} = \langle u_j u_k \rangle \qquad \text{with } j,k \in [1,6]. \tag{2.17}$$

Essentially, the beam matrix characterizes the phase space distribution of the particles at a given location s_0 with the help of the centroid and width of the beam in u_i and u_i' with $i = x, y, \zeta$.

$$\Sigma_{\text{beam}} = \begin{pmatrix} \langle x^2 \rangle & \langle x p_x \rangle & \langle xy \rangle & \langle x p_y \rangle & \langle x\zeta \rangle & \langle x p_z \rangle \\ \langle p_x x \rangle & \langle p_x^2 \rangle & \langle p_x y \rangle & \langle p_x p_y \rangle & \langle p_x \zeta \rangle & \langle p_x p_z \rangle \\ \langle yx \rangle & \langle y p_x \rangle & \langle y^2 \rangle & \langle y p_y \rangle & \langle y\zeta \rangle & \langle y p_z \rangle \\ \langle p_y x \rangle & \langle p_y p_x \rangle & \langle p_y y \rangle & \langle p_y^2 \rangle & \langle p_y \zeta \rangle & \langle p_y p_z \rangle \\ \langle \zeta x \rangle & \langle \zeta p_x \rangle & \langle \zeta y \rangle & \langle \zeta p_y \rangle & \langle \zeta^2 \rangle & \langle \zeta p_z \rangle \\ \langle p_z x \rangle & \langle p_z p_x \rangle & \langle p_z y \rangle & \langle p_z p_y \rangle & \langle p_z \zeta \rangle & \langle p_z^2 \rangle \end{pmatrix} \tag{2.18}$$

The expression for the beam matrix is fully given in equation 2.18. A common alternative way of portraying the beam matrix is

$$\Sigma_{\text{beam}} = \begin{pmatrix} \Sigma_{xx} & \Sigma_{xy} & \Sigma_{xz} \\ \Sigma_{yx} & \Sigma_{yy} & \Sigma_{yz} \\ \Sigma_{zx} & \Sigma_{zy} & \Sigma_{zz} \end{pmatrix}. \tag{2.19}$$

As previously mentioned, the beam matrix can be used to construct a statistical definition of the emittance. The full six-dimensional normalized RMS emittance $\epsilon_{\text{n,6D}}$ is defined via the determinant of the beam matrix,

$$\epsilon_{\text{n,6D}} = \frac{1}{m_0^3 c^3} \sqrt{\det\left(\Sigma_{\text{beam}}\right)}, \tag{2.20}$$

where m_0 denotes the rest mass of the particle and c is the speed of light.

If the subsets of the phase space possess no coupling, Liouville's theorem is also valid for the respective subspace and the beam matrix is reduced to a block diagonal matrix

$$\Sigma_{\text{beam}} = \begin{pmatrix} \Sigma_{xx} & 0 & 0 \\ 0 & \Sigma_{yy} & 0 \\ 0 & 0 & \Sigma_{zz} \end{pmatrix} \tag{2.21}$$

and the determinant of each block on the diagonal yields the respective emittance, as is shown in exemplary for x in the following equation [29]:

$$\epsilon_{\text{n},x} = \frac{1}{m_0 c} \sqrt{\det\left(\Sigma_{xx}\right)} = \frac{1}{m_0 c} \sqrt{\langle x^2 \rangle \langle p_x^2 \rangle - \langle x p_x \rangle^2}. \tag{2.22}$$

In addition to the normalized emittance, the geometrical emittance ϵ_x can be defined. The geometrical emittance can be derived from the normalized emittance via

$$\epsilon_x = \frac{m_0 c \epsilon_{\text{n},x}}{\langle p_z \rangle} = \frac{\epsilon_{\text{n},x}}{\langle (\beta\gamma) \rangle}, \tag{2.23}$$

where $\beta = \frac{v_z}{c}$ is the velocity v_z normalized to the speed of light and

$$\gamma = \frac{1}{\sqrt{1 - \beta^2}} \tag{2.24}$$

is the Lorentz factor. Unlike the normalized emittance, the geometrical emittance is not independent of the beam momentum. During acceleration, the geometrical emittance decreases with increasing momentum. This effect is referred to as adiabatic damping. Only the normalized emittance can be utilized to compare phase space volumes at different times without the influence of kinematic factors [23].

Similarly to the beginning of section 2.1, the momentum p_x can be replaced by the divergence x'. This leads to the expression

$$\epsilon_{\mathrm{tr},x} = \sqrt{\langle x^2 \rangle \langle x'^2 \rangle - \langle x x' \rangle^2}, \tag{2.25}$$

in which $\epsilon_{\mathrm{tr},x}$ is called the trace space emittance. Except for the cases of a significant energy spread being present or the beam being strongly convergent or divergent, $\epsilon_x = \epsilon_{\mathrm{tr},x}$ holds true [29].

In systems of linear, uncoupled beam transport, the emittance is a constant of motion and can in principle be utilized as a measure of the beam quality. While the general shape of the Liouville phase space volume is not necessarily specified, it can be shown that the emittance is related to an ellipse in each dimension irrespective of the concrete particle distribution [29]. An important difference between the emittance and the Liouville phase space is that in certain scenarios, for example passage through a nonlinear field, the emittance will increase even though the phase space volume will remain constant.

Generally speaking, the emittance can be divided into a statistical and a correlated emittance term as

$$\epsilon_x^2 = \epsilon_{x,\mathrm{st}}^2 + \epsilon_{x,\mathrm{cor}}^2. \tag{2.26}$$

The statistical emittance ϵ_{st} constitutes the minimum value of the beam emittance and is closely related to the Liouville phase space volume [30].

2.1.2 Courant-Snyder Invariant

Typically, the Courant-Snyder invariant [31] is derived by making the ansatz

$$x(z) = A\sqrt{\beta(z)}\cos\left(\psi(z) + \psi_0\right) \tag{2.27}$$

for the transverse coordinates. The parameter $\beta(z)$ is one of the three optical functions $(\alpha(z), \beta(z), \gamma(z))$, which are linked to each other via

$$\alpha(z) = -\frac{1}{2}\frac{\mathrm{d}\beta(z)}{\mathrm{d}z} \tag{2.28a}$$

$$\gamma(z) = \frac{1 + \alpha^2(z)}{\beta(z)}. \tag{2.28b}$$

Moreover, the optical functions satisfy $\beta\gamma - \alpha^2 = 1$. The parameters A and $\psi(z)$ will be identified more precisely below. Plugging the ansatz 2.27 into the equation of motion for the transverse coordinates (equation 2.6) yields the expression

$$\gamma(z)x(z) + 2\alpha(z)x(z)x'(z) + \beta(z)x'^2(z) = A^2. \tag{2.29}$$

The parameter A^2 is called the Courant-Snyder invariant. Equation 2.29 actually describes an ellipse which is centered at $(x, x') = (0, 0)$ and covers an area of πA^2. At a given position z_1, a particle is located on an ellipse in the trace space. Further downstream at a position z_2, the particle will be on an ellipse of different shape but with the same area. In the trace space, the evolution of an individual particle is determined by the evolution of its respective ellipse, which in turn is given by the evolution of $\beta(z)$, and by the phase advance $\psi(z)$ between the two points z_1 and z_2, which is defined as

$$\psi(z) = \int_{z_1}^{z_2} \frac{1}{\beta(z)} \mathrm{d}z. \tag{2.30}$$

and essentially defines the location of the particle on its ellipse [24, 23].

The Courant-Snyder invariant, as it is written in equation 2.29, only describes the trajectory of a single particle. In order to extend the invariant to the entire particle ensemble, the parameter A^2 can be linked to the trace space emittance via $A^2 = \epsilon_{\mathrm{tr},x}$ and the optical functions for the particle bunch can be formulated as

$$\alpha_x = -\frac{\langle xx' \rangle}{\epsilon_{\mathrm{tr},x}} \qquad \beta_x = \frac{\langle x^2 \rangle}{\epsilon_{\mathrm{tr},x}} \qquad \gamma_x = \frac{\langle x'^2 \rangle}{\epsilon_{\mathrm{tr},x}}. \tag{2.31}$$

All of the optical functions can be associated with geometric properties of the ellipse. The parameters $\sqrt{\beta_x}$ and $\sqrt{\gamma_x}$ correspond to the width in x and x', respectively. The tilt of the ellipse is given by the parameter α_x.

Furthermore, the optical functions can be summarized in the matrix Σ_β and linked to the beam matrix in trace space form $\Sigma_{\mathrm{tr},xx}$ via

$$\Sigma_{\mathrm{tr},xx} = \begin{pmatrix} \langle x^2 \rangle & \langle xx' \rangle \\ \langle xx' \rangle & \langle x'^2 \rangle \end{pmatrix} = \epsilon_{\mathrm{tr},x} \begin{pmatrix} \beta_x(z) & -\alpha_x(z) \\ -\alpha_x(z) & \gamma_x(z) \end{pmatrix} = \epsilon_{\mathrm{tr},x} \Sigma_{\beta_x}. \tag{2.32}$$

The transformation of the optical functions can be performed with help of a transfer matrix as introduced in section 2.1. If the optical functions at z_1 are known and denoted as $\Sigma_{\beta 1}$, then $\Sigma_{\beta 2}$ at a position z_2 can be calculated via

$$\Sigma_{\beta 2} = \mathcal{M}_{1,2} \cdot \Sigma_{\beta 1} \cdot \mathcal{M}_{1,2}^{\mathrm{T}}, \tag{2.33}$$

where $\mathcal{M}_{1,2}$ is the transfer matrix from z_1 to z_2 [23].

2.2 LONGITUDINAL BEAM DYNAMICS

In the previous section, the discussion was concentrated on linear beam dynamics in the transverse plane and the portrayal of an appropriate matrix formalism to describe the beam transport. The guiding of the charged particles along a desired path is achieved with transverse electromagnetic fields. However, these transverse fields do not directly contribute to the acceleration of the particles. For the purpose of acceleration, longitudinal fields are required.

In the following, only the longitudinal phase space, constructed from the longitudinal particle position ζ in the co-moving frame and the Lorentz factor γ

of the particle, is considered. The Lorentz factor essentially corresponds to the energy of the particle.

At REGAE, two rf cavities are installed for accelerating and compressing the bunch, i.e. for manipulations of its longitudinal phase space. Assuming an rf field with an electric field component

$$\mathcal{E}_z(z,t) = \mathcal{E}_0 \exp(i \cdot (\omega t - kz)) = \mathcal{E}_0 \exp(i\phi), \tag{2.34}$$

where $\mathcal{E}_0$ is the amplitude and $\phi = \omega t - kz$ is the phase with angular frequency ω and wave number k of the rf field, the momentum of the charged particle changes according to

$$\frac{\mathrm{d}p_z}{\mathrm{d}t} = e\mathcal{E}(z,t). \tag{2.35}$$

Integration of equation 2.35 through the accelerating cavity of length L_c yields the energy increase of the particle in terms of the Lorenz factor [25]:

$$\Delta\gamma = \frac{e}{m_e c^2} \int_{L_c} \mathcal{E}_z(z,t)\mathrm{d}z. \tag{2.36}$$

It should be noted that the integration along the longitudinal coordinate over the length of the cavity is merely a simplification and that the integral should actually be computed with respect to time instead. However, this can become tedious due to the time-dependency of both the electric field and the velocity of the particle [25].

Moreover, the gun cavity installed at REGAE displays complex dynamics due to the strong phase slippage [16]. This further complicates an analytical calculation of the energy gain in the gun. The energy gain can be obtained numerically from an ASTRA simulation. Alternatively, the final beam energy can be measured with the spectrometer setup as described in section 3.2.2.

The foremost purpose of the buncher cavity at REGAE is the compression of the electron bunch. In order to achieve this, the bunch needs to be imprinted with a negative energy correlation. This means that the electrons located in the tail of the bunch should have a higher energy than the electrons located in the front part of the bunch.

Both of the cavities at REGAE are standing wave cavities. Therefore, it is possible to write the longitudinal component of the electric field in the cavity as

$$\mathcal{E}_z(z,\phi) = \frac{1}{2}\mathcal{E}_0 \left(\sin(\phi + \phi_0) + \sin(\phi + 2kz + \phi_0)\right), \tag{2.37}$$

where $\phi = \omega t - kz$ defines the phase and $\phi_0 = \text{const.}$ is an additional phase offset [16]. The second term in the above equation describes the counterpropagating part of the standing wave inside the cavity. For particles propagating with $v_z = c$, $\phi = \text{const.}$ holds true. In this case, the integration in equation 2.36 can easily be carried out for a cavity of length $L_c \propto \frac{\pi}{2k}$ to obtain the energy gain

$$\begin{aligned}
\Delta\gamma &= \frac{e}{m_e c^2} \int_0^{L_c} \mathcal{E}_z(z,\phi)\mathrm{d}z \\
&= \frac{e\mathcal{E}_0}{2m_e c^2} \left[z\sin(\phi + \phi_0) - \frac{1}{2k}\cos(\phi + 2kz + \phi_0) \right]_0^{L_c} \\
&= \frac{e\mathcal{E}_0 L_c}{2m_e c^2} \sin(\phi + \phi_0)
\end{aligned} \tag{2.38}$$

of a particle traveling through the cavity. By defining $\phi = 0$ as the phase where the energy gain of the particle reaches its maximum, as is common practice, the phase offset ϕ_0 is fixed. Essentially, the amplitude and phase of the cavity are the only parameters which can be adjusted freely during machine operation.

The details of the bunch compression technique at REGAE are described in more detail below.

2.2.1 Ballistic Bunching Mechanism

As stated in the previous section, a negative energy correlation must be imprinted on the bunch to achieve a compression of the bunch length. At REGAE, this is implemented by means of the ballistic bunching mechanism [10, 19]. Due to the fact that the mean energy of the electron beam is comparatively low, the velocity difference arising from the negative energy correlation is, in comparison to the mean velocity of the electron bunch, large enough for the electrons in the tail of the bunch to outrun the preceding electrons within a reasonable distance.

Considering two particles propagating through a free drift segment from an initial position z_0 to z, the longitudinal shift between these particles is given by

$$\Delta\zeta(z) = \int_{z_0}^{z} \frac{\Delta\beta}{\beta} \mathrm{d}z = \frac{\Delta\beta}{\beta}(z - z_0), \tag{2.39}$$

where β denotes the average velocity of the bunch normalized to the speed of light and $\Delta\beta$ is the velocity difference between the particles [10]. In first order, the integral can be computed to yield

$$\Delta\zeta(z) = \frac{1}{\beta_r}\left[\frac{\mathrm{d}\beta}{\mathrm{d}\gamma}\bigg|_{\gamma_r} \delta\gamma\right]_{z_0} (z - z_0), \tag{2.40}$$

where the derivative $\frac{\mathrm{d}\beta}{\mathrm{d}\gamma}$ is to be evaluated at the energy γ_r of the reference particle, i.e. the central particle of the bunch at $\zeta = 0$ and of the linear approximation [17]. The energy deviation from γ_r is expressed by $\delta\gamma$. Similarly, β_r denotes the velocity of the reference particle and the squared brackets $[\cdot]_{z_0}$ signify the evaluation of the entire respective expression at $z = z_0$. The derivative can be calculated directly after inversion of equation 2.24. Thus, the longitudinal shift can ultimately be written as

$$\Delta\zeta(z) = \left[\frac{1}{\gamma_r^3\beta_r^2}\delta\gamma\right]_{z_0} (z - z_0). \tag{2.41}$$

Utilization of the ballistic bunching mechanism translates to operation of the buncher cavity at the zero-crossing, i.e. setting the cavity phase to $\phi_\mathrm{b} = -90\,\mathrm{deg}$. In the drift section behind the buncher cavity, the longitudinal shift evolves as specified above and the bunch length decreases until the longitudinal focus is reached, after which the bunch length starts to increase again. As a result of the fact that the expression in equation 2.41 scales inversely with γ^3, the longitudinal shift caused by the negative energy correlation imprinted by the buncher cavity is strongly suppressed for higher values of γ. This means that the ballistic bunching mechanism becomes inefficient for larger beam energies.

The achievable compression using the ballistic bunching mechanism can be strongly influenced by space charge forces [19, 32]. For a round beam of radius r_0 consisting of particles carrying a charge q propagating through a circular beam pipe with radius r_b in vacuum, the longitudinal space charge field E_{z0} in the center of the beam is given by

$$\mathcal{E}_{z0} = \mathcal{E}_{z,\mathrm{b}} - \frac{q}{4\pi\epsilon_0\gamma^2}\left(1 + 2\ln\left(\frac{r_\mathrm{b}}{r_0}\right)\right)\frac{\partial\lambda_\mathrm{p}(z)}{\partial z}, \tag{2.42}$$

where $\mathcal{E}_{z,\mathrm{b}}$ denotes the longitudinal field on the walls of the beam pipe and $\lambda_\mathrm{p}(z)$ is the local linear particle density normalized to the total number of charged particles in the beam [25]. While space charge fields vanish for a continuous particle beam with a uniform density distribution, realistic beams with variations in the line charge distribution will experience effects from longitudinal space charge fields [25]. Typically, this leads to an increase in bunch length by accelerating particles in the front part of the bunch and decelerating particles in the back part of the bunch.

While space charge effects typically scale with higher powers of $1/\gamma$ [25, 33] and are thus more dominant for low energy beams in the MeV range, as is the case at REGAE, these effects can be mitigated by decreasing the bunch charge. Performing measurements at ultralow bunch charges below $\sim 50\,\mathrm{fC}$ (at REGAE) significantly reduces space charge effects.

2.2.2 Nonlinear Effects

Despite the fact that an upright line is expected as the ideal desired distribution in the longitudinal phase space at the position of the longitudinal focus, it has been shown that a parabolic shape is observed in place of a straight line in phase space [16]. This arises from the nonlinearity of the energy correlation itself. In the gun cavity, the electron bunch occupies a certain phase interval on the longitudinal field component, which in turn displays an extent of curvature due to its sinusoidal shape. Combined with the substantial phase slippage between the electron bunch and the rf field, this results in the build-up of a nonlinear energy correlation. In addition to this, the nonlinear relation between the particle's energy γ and its velocity β (see equation 2.24) gives rise to a finite curvature in the subsequent drift section.

This can be exemplified by performing a Taylor expansion of equation 2.39 around the energy of the reference particle, which has the phase space coordinates $(\zeta = 0, \gamma = \gamma_r)$. This yields a modified expression of the form

$$\Delta\zeta(z) = \frac{1}{\beta_r}\left[\sum_{n=1}\frac{1}{n!}\frac{\mathrm{d}^n\beta}{\mathrm{d}\gamma^n}\bigg|_{\gamma_r}(\delta\gamma)^n\right]_{z_0}(z - z_0) \tag{2.43}$$

for the longitudinal shift in the third order accumulated in a free drift section [17]. It is assumed that the energy of particle remains constant throughout propagation through the drift. Computing the derivatives and breaking off the expansion at the third order yields

$$\Delta\zeta(z) = \left[\frac{1}{\gamma_r^3\beta_r^2}\delta\gamma + \frac{2 - 3\gamma_r^2}{2\gamma_r^6\beta_r^4}(\delta\gamma)^2 + \frac{2 - 5\gamma_r^2 + 4\gamma^4}{2\gamma_r^9\beta_r^6}(\delta\gamma)^3\right]_{z_0}(z - z_0). \tag{2.44}$$

On the one hand, the higher order terms quickly become negligible for high values of γ, leading to a suppression at high enough energies. On the other hand, almost any type of energy distribution will display higher order contributions and thus a nonvanishing curvature in the longitudinal phase space for low values of γ, i.e. for lower energies.

Naturally, an analogous description can be formulated for the impact a cavity has on the longitudinal phase space. In contrast to the drift section, which only leads to an alteration of the longitudinal coordinate ζ of a particle, the cavity is assumed to only affect the particle's energy. Furthermore, this energy change is assumed to be instantaneous, which corresponds to a form of thin lens approximation for the cavity. In order to perform a respective Taylor expansion of the energy gain in $\delta\phi$ around ϕ, where $\pm\delta\phi$ is the phase interval occupied by the bunch around the nominal accelerating phase ϕ, the distribution in the longitudinal phase space must be describable by a function, i.e. it must be free of ambiguities in ϕ. Making use of the fact that the accelerating phase ϕ corresponds to the reference particle located at $\zeta = 0$, the energy gain can be approximated by

$$\begin{aligned}\Delta\gamma &= \frac{e\mathcal{E}_0 L_c}{2m_e c^2}\sin(\phi+\delta\phi)\\ &\approx \frac{e\mathcal{E}_0 L_c}{2m_e c^2}\left(\sin(\phi)-\cos(\phi)\delta\phi-\frac{\sin(\phi)(\delta\phi)^2}{2}-\frac{\cos(\phi)(\delta\phi)^3}{6}\right)\end{aligned} \tag{2.45}$$

in third order. Since a particle with a longitudinal offset of ζ implies a phase deviation $\delta\phi = -k\zeta$ [16], the energy gain can be expressed as a function of the longitudinal coordinate ζ:

$$\begin{aligned}\Delta\gamma = &\frac{e\mathcal{E}_0 L_c \sin(\phi)}{2m_e c^2} - \frac{e\mathcal{E}_0 L_c k\cos(\phi)}{2m_e c^2}\zeta - \frac{e\mathcal{E}_0 L_c k^2\sin(\phi)}{4m_e c^2}\zeta^2\\ &+\frac{e\mathcal{E}_0 L_c k^3\cos(\phi)}{12m_e c^2}\zeta^3.\end{aligned} \tag{2.46}$$

Based on the expressions written in equations 2.44 and 2.46, the initial longitudinal phase space coordinates can be mapped to an arbitrary point behind the respective cavity. Thus, it is possible to establish a description of the longitudinal evolution of the bunch at the REGAE beamline, where the longitudinal phase space coordinates $[\zeta, \gamma(\zeta)]$ can be calculated at arbitrary points within the beamline. This description provides the basis of the phase space linearization method presented in [17], for which experimental studies are presented in section 5.

2.3 TRANSVERSE DEFLECTING STRUCTURE

Transverse rf deflecting structures provide a highly reliable and robust method for performing measurements regarding the longitudinal bunch properties of an electron bunch. Possible applications of a TDS in accelerator beamlines include but are not limited to the measurement of the bunch length [34], the characterization of the longitudinal phase space [35, 36] and even the measurement of the transverse slice emittance [37]. The very first iris-loaded TDS was designed in

the 1960's at the Stanford Linear Accelerator Center (SLAC) [38]. The theorem established by Panofsky and Wenzel [39] was the basis for its design and its intended purpose was the separation of charged particles in particle beams. This structure was then transported to and installed at FLASH, located on the DESY campus, for longitudinal beam diagnostics [40].

A TDS has the ability of measuring bunch lengths ranging from picoseconds all the way down to femtosecond level [41]. These measurements are single-shot measurements. It is therefore possible to investigate shot-to-shot fluctuations with a TDS. One major disadvantage of machine operation with a TDS is the fact that the measurement is destructive, i.e. the beam parameters of the electron bunch behind the TDS are of far lower quality in comparison to the initial beam parameters in front of the TDS. However, this drawback is not of significant relevance for the measurements performed at REGAE.

At REGAE, machine operation is planned for bunch lengths in the order of 10 fs at ultralow sub-pC bunch charges with a normalized emittance down to nanometer level. Such ultrashort bunch lengths are far below the resolution of conventional streaking camera technology. In order to cope with these design parameters and measure the longitudinal bunch parameters, an S-band TDS has been designed and installed at REGAE [9, 42, 43].

The underlying physics of a TDS is outlined in the section below, whereas the actual design of the TDS implemented at REGAE is described in more detail in section 4.1.

2.3.1 Beam Dynamics in a TDS

The underlying working principle of a TDS can be described as follows: a correlation between the longitudinal position of a particle in the bunch and its transverse momentum is introduced by the TDS, which effectively leads to a shearing of the bunch in the transverse plane. Subsequently, the longitudinal distribution can be imaged on a detector stream further downstream. In the following derivations, a TDS which shears the bunch in the vertical direction y is considered.

A relativistic electron with $|\vec{v}| \to c$ and a charge of e propagating along the z-axis through the electromagnetic field of a TDS is affected by the Lorentz force

$$\vec{F}_{\mathrm{L}} = e\left(\vec{\mathcal{E}} + \vec{v} \times \vec{B}\right), \tag{2.47}$$

where $\vec{\mathcal{E}}$ is the electric field, $\vec{B}$ is the magnetic field and $\vec{v}$ denotes the velocity of the particle. A thorough description and analysis of the deflecting field in rf deflecting structures is provided in [44]. Additionally, expressions for the field components in cylindrical coordinates can be found in [45]. After a transformation to the Cartesian coordinate system, the Lorentz force acting in a TDS can be written as

$$\begin{pmatrix} F_x \\ F_y \\ F_z \end{pmatrix} = e\mathcal{E}_0 \begin{pmatrix} 0 \\ \sin(\varphi) \\ ky\cos(\varphi) \end{pmatrix}, \tag{2.48}$$

where k denotes the wave number of the TDS and $\mathcal{E}_0$ is equal to the amplitude of a wave $\mathcal{E}_0 \cdot \exp(i(kz - \omega t))$. For simplicity, it is assumed that the bunch center traverses the TDS along a straight line and interactions with the counterpropagating part of the wave are neglected. More specific and complete considerations with respect to the unique design of the TDS at REGAE are expanded upon in section 4.1, where an outline of the deflecting fields and arising nonlinear effects is also given.

Due to the fact that $F_x = 0$ and F_y is independent of the x- and z-position of the electron, the induced deflection is free of aberration and occurs only in the vertical direction. Moreover, the longitudinal component of F_L exhibits linear dependency on the y-position of the electron and vanishes for particles without vertical offset ($F_z(y = 0) = 0$). The phase φ may also be expressed by $\varphi = k\zeta + \varphi_0$ with the rf phase φ_0 given relative to the center of mass of the bunch [46]. At this point it should be noted that only the phase space coordinates relevant for the TDS will be considered, i.e. the general phase space vector as defined in equation 2.1 is modified to

$$\vec{u} = \begin{pmatrix} y & y' & \zeta & p_z \end{pmatrix}^\mathrm{T}. \tag{2.49}$$

Since the Lorentz force vanishes in the horizontal direction x, the motion of the electron in the horizontal direction remains unaltered. The z-component of the momentum is assumed to be equal to $p_z \approx |\vec{p}| \approx$ const. and the ζ-coordinate itself is given relative to the center of the bunch. The divergence y' and the vertical coordinate y are again given in relation to the axis of the design trajectory z.

Concerning the expression for the phase $\varphi = k\zeta + \varphi_0$, some fundamental considerations with respect to bunch length measurements at REGAE seem sensible. The cavities at REGAE are operated at a frequency of $\nu = 2.998\,\mathrm{GHz}$. The wave number can be calculated from the frequency via

$$k = \frac{2\pi\nu}{c}. \tag{2.50}$$

For the case of machine operation without the buncher cavity, i.e. without any form of bunch compression scheme, the electron bunch length is expected to be on the level of 150 µm, which corresponds to approximately 500 fs. Plugging all values into the $k\zeta$-term yields $k\zeta \approx 9 \cdot 10^{-3}$. Consequently, a Taylor expansion around $k\zeta = 0$ can be performed for the respective terms in the Lorentz force, which leads to

$$\begin{aligned} \begin{pmatrix} F_{\mathrm{L},y} \\ F_{\mathrm{L},z} \end{pmatrix} &= e\mathcal{E}_0 \begin{pmatrix} \sin(k\zeta + \varphi_0) \\ ky\cos(k\zeta + \varphi_0) \end{pmatrix} \\ &\approx \begin{pmatrix} k\zeta\cos(\varphi_0) + \sin(\varphi_0) \\ ky(\cos(\varphi_0) - k\zeta\sin(\varphi_0)) \end{pmatrix}. \end{aligned} \tag{2.51}$$

Subsequently, an electron entering a TDS of length L_TDS with an initial phase space vector $\vec{u}_0 = (y_0, y', \zeta, p_z)^\mathrm{T}$ is considered. As previously mentioned, the TDS

exerts a transverse kick on the electron. This leads to an alteration $\Delta y'$ of the angle at a position z within the TDS, which can be calculated as follows:

$$\begin{aligned} y'(z) &= y'_0 + \int_0^{y'(z)} \mathrm{d}y'(z) = y'_0 + \int_0^{p_y(z)} \frac{1}{|\vec{p}|} \mathrm{d}p_y \\ &= y'_0 + \frac{1}{|\vec{p}|c} \int_0^z F_{\mathrm{L},y} \mathrm{d}z. \end{aligned} \tag{2.52}$$

Plugging in the approximated expression for $F_{\mathrm{L},y}$ from equation 2.51 into equation 2.52 yields

$$y'(z) = y'_0 + \Delta y' = y'_0 + \frac{e\mathcal{E}_0 z(k\zeta\cos(\varphi_0) + \sin(\varphi_0))}{|\vec{p}|c}. \tag{2.53}$$

When operating a TDS in diagnostics mode, it is beneficial for the induced deflection angle $\Delta y'$ to be linearly dependent on the longitudinal position z, which requires $\varphi_0 = 0$. This means that the TDS is operated at zero-crossing[2], where no deflecting field is present for the center of the bunch [44]. As a result, equation 2.53 is simplified to

$$y'(z) = y'_0 + \frac{e\mathcal{E}_0 k\zeta z}{|\vec{p}|c}. \tag{2.54}$$

Due to the fact that the position $y(z)$ is related to $y'(z)$ via $y'(z) = \mathrm{d}y/\mathrm{d}z$, it is possible to calculate $y(z)$ as follows:

$$y(z) = y_0 + \int_0^{y(z)} \mathrm{d}y(z) = y_0 + \int_0^z y'(z)\mathrm{d}z = y_0 + y'_0 z + \frac{e\mathcal{E}_0 k\zeta z^2}{2|\vec{p}|c}. \tag{2.55}$$

The cumulative vertical displacement and angle at the end of the cavity can ultimately be written as

$$\begin{aligned} y(z = L_{\mathrm{TDS}}) &= y_0 + y'_0 L_{\mathrm{TDS}} + \frac{e\mathcal{E}_0 k\zeta L_{\mathrm{TDS}}^2}{2|\vec{p}|c} = y_0 + y'_0 L_{\mathrm{TDS}} + \frac{eV_0 k\zeta L_{\mathrm{TDS}}}{2|\vec{p}|c} \\ &= y_0 + y'_0 L_{\mathrm{TDS}} + \frac{KL_{\mathrm{TDS}}\zeta}{2} \end{aligned} \tag{2.56a}$$

$$y'(z = L_{\mathrm{TDS}}) = y'_0 + K\zeta \tag{2.56b}$$

where the $V_0 = \mathcal{E}_0 L_{\mathrm{TDS}}$ is the peak effective voltage and the substitution $K = \frac{eV_0 k}{|\vec{p}|c}$ has been introduced. The parameter K indicates the deflection angle induced by the TDS per unit length [44]. With the help of equation 2.56a, the vertical component of the momentum change can also be calculated:

$$\begin{aligned} \Delta p_y &= \int_0^{p_y(y(z=L))} \mathrm{d}p_y = \frac{1}{c} \int_0^{y(z=L)} F_{\mathrm{L},y} \mathrm{d}y \\ &= \frac{e\mathcal{E}_0 k}{c} \left(\zeta y_0 + L_{\mathrm{TDS}}\zeta y'_0 + \frac{KL_{\mathrm{TDS}}\zeta^2}{2} \right). \end{aligned} \tag{2.57}$$

2 It is also possible to operate a TDS at the other zero-crossing defined by $\varphi_0 = \pi$.

As a result of the longitudinal component of the Lorentz force for particles not located at the vertical center of the bunch ($y \neq 0$), an electron may experience a change in the longitudinal component of its momentum. This is a direct consequence of the Panofsky-Wenzel theorem [39], according to which streaking in the transverse plane is only possible if the transverse gradient of the longitudinal field component does not vanish. A transverse component of the Lorentz force requires the existence of a longitudinal electric and magnetic field [45]:

$$\vec{F}_\perp \propto (\vec{e}_z \times \vec{\nabla} B_z)_\perp \propto \vec{\nabla}_\perp \mathcal{E}_z. \tag{2.58}$$

Consequently, $F_{\mathrm{L},z} \neq 0$ and the shift in longitudinal momentum Δp_z experienced by an electron upon passage through the TDS is equal to

$$\begin{aligned}\Delta p_z &= \frac{1}{c}\int_0^{L_{\mathrm{TDS}}} F_{\mathrm{L},z}(z)\mathrm{d}z = \frac{e\mathcal{E}_0 k}{c}\int_0^{L_{\mathrm{TDS}}} y(z)\mathrm{d}z \\ &= \frac{e\mathcal{E}_0 k}{c}\left(y_0 L_{\mathrm{TDS}} + \frac{y_0' L_{\mathrm{TDS}}^2}{2} + \frac{K\zeta L_{\mathrm{TDS}}^2}{6}\right).\end{aligned} \tag{2.59}$$

Considering the fact that $F_{\mathrm{L},x} = 0$, it is evident that the horizontal momentum component p_x is not affected by the TDS. A comparison between equations 2.57 and 2.59 leads to the conclusion that each term inside the bracket in the expression for Δp_z is much larger than the according term in Δp_x. This results from the fact that $\zeta \approx 150\,\mu\mathrm{m}$ is the dominant length scale in Δp_x; the strong ζ-dependence is replaced by L_{TDS} in Δp_z. The TDS installed at REGAE has a length of $L_{\mathrm{TDS}} = 270\,\mathrm{mm}$, which means that $L_{\mathrm{TDS}} \gg \zeta$ holds true. Therefore, the total momentum change can be expressed by $\Delta|\vec{p}| \approx \Delta p_z$. The total relative momentum deviation, as defined in the beginning of section 2.1, at the exit of the TDS is equal to

$$\begin{aligned}\delta p &= (\delta p)_0 + \Delta(\delta p) = (\delta p)_0 + \frac{\Delta p}{|\vec{p}|} \approx (\delta p)_0 + \frac{\Delta p_z}{|\vec{p}|} \\ &= (\delta p)_0 + K y_0 + \frac{K L_{\mathrm{TDS}} y_0'}{2} + \frac{K^2 L_{\mathrm{TDS}}\zeta}{6}.\end{aligned} \tag{2.60}$$

With the help of equations 2.56a, 2.56b and 2.60, the transfer matrix for the TDS in first order can be formulated as [47]

$$\mathcal{M}_{\mathrm{TDS}} = \begin{pmatrix} 1 & L & \frac{KL_{\mathrm{TDS}}}{2} & 0 \\ 0 & 1 & K & 0 \\ 0 & 0 & 1 & 0 \\ K & \frac{KL_{\mathrm{TDS}}}{2} & \frac{K^2 L_{\mathrm{TDS}}}{6} & 1 \end{pmatrix}. \tag{2.61}$$

The entries regarding x and x' have been omitted. Moreover, the above depiction of the transfer matrix takes the length of the structure into account. Similarly to the transfer matrix for focusing magnets as discussed in section 2.1, the limit $L_{\mathrm{TDS}} \to 0$ can be applied. This yields a simplified thin lens form of the TDS transfer matrix:

$$\mathcal{M}_{\mathrm{TDS}} \approx \begin{pmatrix} 1 & 0 & 0 & 0 \\ 0 & 1 & K & 0 \\ 0 & 0 & 1 & 0 \\ K & 0 & 0 & 1 \end{pmatrix}. \tag{2.62}$$

The TDS acts as a free drift space with regards to the horizontal coordinates.

2.3.2 Bunch Length Reconstruction

As described in the previous section, an electron receives a transverse kick dependent on its longitudinal position upon passage through a TDS. The ζ-coordinate is thus mapped to the transverse plane. By measuring the transverse beam size of the electron bunch downstream of the TDS, the bunch length inside the TDS can be reconstructed.

In the following section, the phase space vector of an electron at the entrance of the TDS and located at z_0 will be denoted by

$$\vec{u}_0 = \begin{pmatrix} x_0 & x_0' & y_0 & y_0' & \zeta & (\delta p)_0 \end{pmatrix}^{\mathrm{T}}. \tag{2.63}$$

The TDS itself will be approximated in thin lens form as represented by the matrix given in equation 2.62. The phase space vector at the position of a detector located at z_d can be calculated via

$$\vec{u}_\mathrm{d} = \mathcal{M}_{\mathrm{TDS}\to z_\mathrm{d}} \cdot \mathcal{M}_{\mathrm{TDS}} \cdot \vec{u}_0, \tag{2.64}$$

where $\mathcal{M}_{\mathrm{TDS}\to z_\mathrm{d}}$ denotes the transfer matrix of the beamline section downstream of the TDS. Multiplication of the TDS transfer matrix the the initial phase space vector yields

$$\vec{u}_\mathrm{d} = \mathcal{M}_{\mathrm{TDS}\to z_\mathrm{d}} \cdot \begin{pmatrix} x_0 \\ x_0' \\ y_0 \\ y_0' + K\zeta \\ \zeta \\ Ky_0 + (\delta p)_0 \end{pmatrix}. \tag{2.65}$$

On a detector screen, where the transverse distribution of the bunch is imaged, the transverse position coordinates are decisive. Since the horizontal coordinates x and x' are not affected by the TDS, the vertical position y is of particular interest. Under the assumption that the individual planes are decoupled and that the electron bunch undergoes no further change of energy after passage through the TDS, the vertical position y_d on the detector is given by

$$\begin{aligned} y_\mathrm{d} &= \mathcal{M}_{\mathrm{TDS}\to z_\mathrm{d},33} \cdot y_0 + \mathcal{M}_{\mathrm{TDS}\to z_\mathrm{d},34} \cdot y_0' + \mathcal{M}_{\mathrm{TDS}\to z_\mathrm{d},34} \cdot K\zeta \\ &= y_{\mathrm{d,off}} + \mathcal{M}_{\mathrm{TDS}\to z_\mathrm{d},34} \cdot K\zeta. \end{aligned} \tag{2.66}$$

In the above equation, $y_{\mathrm{d,off}}$ denotes the vertical position on the detector without the influence of the TDS, i.e. when the TDS is not activated. The additional term $\mathcal{M}_{\mathrm{TDS}\to z_\mathrm{d},34} \cdot K\zeta$ appears as a result of the deflection induced by the TDS.

At this point, it is helpful to express the matrix element in terms of the optical functions and phase advance [48] as introduced in section 2.1.2, which yields

$$\begin{aligned} y_\mathrm{d} &= y_{\mathrm{d,off}} + \sqrt{\beta_y(z_\mathrm{d})\beta_y(z_0)}\,\sin(\Delta\psi_y) K\zeta \\ &= y_{\mathrm{d,off}} + S\zeta, \end{aligned} \tag{2.67}$$

where $\beta_y(z_0)$ denotes the beta-function at the position of the TDS, $\beta_y(z_\mathrm{d})$ corresponds to the beta-function at the position of the detector and $\Delta\psi_y$ is the vertical phase advance between z_0 and z_d. The parameter S which has been introduced in equation 2.67 is also known as the shear parameter [46]

$$S = \sqrt{\beta_y(z_0)\beta(z_\mathrm{d})}\sin(\Delta\psi_y)K = \frac{ekV_0\sqrt{\beta_y(z_0)\beta_y(z_\mathrm{d})}\sin(\Delta\psi_y)}{c|\vec{p}|}. \tag{2.68}$$

The shear parameter essentially characterizes the deflection strength of the TDS. From equation 2.67 it follows that the measured beam size on the detector $y_\mathrm{RMS}(z_\mathrm{d})$ is in fact a combination consisting of the bunch length in the center of the TDS $\zeta_\mathrm{RMS}(z_0)$ and the unperturbed beam size at the detector $y_\mathrm{RMS,off}(z_\mathrm{d})$, which can be measured when the TDS itself is switched off [48]. Under the assumption that the electrons in the bunch possess no correlation between the vertical coordinates (y_0, y_0') and the longitudinal position ζ upon entering the TDS, the bunch length can be calculated via

$$\zeta_\mathrm{RMS} = \sqrt{\frac{y_\mathrm{RMS}^2 - y_\mathrm{RMS,off}^2}{S^2}}. \tag{2.69}$$

The bunch length is sometimes also given in units of time, which will be denoted as $\xi_\mathrm{RMS} = \zeta_\mathrm{RMS}/c$ in this thesis.

The longitudinal resolution of the measurement [44, 46] performed with the TDS is given by

$$R_z = \frac{y_\mathrm{RMS,off}}{S} = \frac{y_\mathrm{RMS,off}}{\sqrt{\beta_y(z_0)\beta_y(z_\mathrm{d})}\sin(\Delta\psi_y)K}. \tag{2.70}$$

Essentially, the resolution constitutes the (longitudinal) slice length threshold above which it is possible to resolve the internal structure. However, this does not render the measurement of bunch lengths below the longitudinal resolution impossible. In principle, the knowledge of the internal structure is not required to measure the RMS bunch length, which is reconstructed from RMS beam sizes. Therefore, bunch length measurement is essentially limited by the screen resolution of the detector system. Nevertheless, this limit also depends on the shear parameter S; in any case, a maximum shear parameter is usually desirable.

Considering the longitudinal resolution, i.e. the shear parameter, it is beneficial to adjust the machine parameters in such a way that the vertical beta-function $\beta_y(z_0)$ at the center of the TDS is comparatively large. In addition to this, a vertical phase advance between z_0 and z_d of $\Delta\psi_y = \frac{\pi}{2} + n\pi$ with $n \in \mathbb{N}$ is desirable in order to optimize the resolution.

In order to reconstruct the bunch length with the help of equation 2.69, the vertical distribution of the bunch needs to be measured downstream of the TDS and the shear parameter needs to be known. While the first requirement is easily fulfilled by use of an appropriate detector, the calculation of the shear parameter requires precise knowledge of the transfer matrix from the TDS to the detector. However, it is also possible to directly reconstruct the shear parameter experimentally through measurements. As can be seen in equation 2.69, the

vertical position of the particle at the detector depends linearly on the longitudinal position. Applying the statistical mean operator to equation 2.67 yields

$$\langle y_\mathrm{d} \rangle = \langle y_\mathrm{d,off} \rangle + S \langle \zeta \rangle. \tag{2.71}$$

A shift in the bunch position $\Delta\langle y_\mathrm{d} \rangle$ resulting from a shift $\Delta\langle \zeta \rangle$ is therefore also linearly dependent. The longitudinal center position of the bunch can be written as $\Delta\langle \zeta \rangle \approx \beta c \Delta t$, which means that the bunch is shifted from the rf zero phase by a delay in time Δt. The time delay can be rewritten as

$$\Delta t = \frac{\Delta\varphi}{2\pi\nu}, \tag{2.72}$$

where $\Delta\varphi$ is a small shift in the rf phase around the zero-crossing $(\varphi_0 = 0)$ and ν is the rf frequency of the TDS. Since $\langle y_\mathrm{d,off} \rangle$ remains unaffected by a shift $\Delta\varphi$,

$$\Delta\langle y_\mathrm{d} \rangle = \frac{S\beta c \Delta\varphi}{2\pi\nu} \tag{2.73}$$

holds true. Consequently, performing a measurement of the mean beam position $\langle y_\mathrm{d} \rangle$ while varying the rf phase φ in a small range around the zero-crossing phase φ_0 allows the the reconstruction of the shear parameter S. More specifically, S can be derived from a linear fit $\langle y_\mathrm{d} \rangle = a\varphi + b$ as

$$S = \frac{2\pi\nu a}{\beta c} = \frac{360^\circ \nu a}{\beta c}, \tag{2.74}$$

where a denotes the slope of the linear fit.

3 THE REGAE BEAMLINE

REGAE is a linear accelerator beamline of approximately 10 m in length. The machine was constructed by DESY; the target chamber was provided by the Max Planck Institut für Struktur und Dynamik der Materie (MPSD). Originally, the objective of REGAE was to perform UED experiments. For this purpose, REGAE was specifically designed to cope with the respective experimental requirements and thus deliver an electron beam of low energy ($\approx 5\,\mathrm{MeV}$) and ultrashort ($\sim 10\,\mathrm{fs}$) electron bunches with very low transverse emittance for time-resolved UED.

In the year 2018, the REGAE beamline underwent an extensive upgrade [16] as part of a collaboration between DESY and the University of Hamburg. The beamline has been adapted to enable experiments regarding the external injection of electron bunches into a laser-plasma wakefield [49]. The well-known electron beam produced by REGAE may be used as a probing tool of the laser-driven plasma wakefield [50].

In the course of the beamline upgrade, the REGAE front-end containing the accelerating structures has remained mostly unchanged. This segment of the beamline is outlined in section 3.1. The rest of the beamline has been completely rebuilt and is described in section 3.2.2.

3.1 REGAE FRONT-END

The front-end of the REGAE beamline contains both of the accelerating rf structures, namely the gun cavity and buncher cavity. An overview of this section can be seen in figure 3.1.

All of the cavities at REGAE are operated in the S-band at a frequency of 2.998 GHz. The gun cavity is similar to the electron gun implemented at the FLASH accelerator, albeit scaled to a different size. Both gun and and buncher cavity are normal conducting copper cavities. The electron gun is comprised of 1.6 cells and is in fact a photoinjector cavity. This means that the electron beam is generated with the help of the photoelectric effect: a laser pulse shines on the cathode material and produces an electron bunch [51]. The electron bunch adopts the shape of the incoming laser pulse. At this point it should be noted that the cathode marks the origin of the accelerator beamline, i.e. it is positioned at $z = 0$. The charge of the electron bunch depends heavily on the cathode material. Typically, the REGAE beamline is operated with either a Molybdenum or Cesium Telluride cathode. Experience has shown that the charge obtained with the Cesium Telluride cathode is potentially much larger compared to the Molybdenum cathode.

A Titanium sapphire (Ti:Sa) laser system generates an infrared (IR) laser pulse of 800 nm wavelength. This laser system is located in the laser laboratory in the basement of the building. Using a system of mirrors, the laser beam is transported

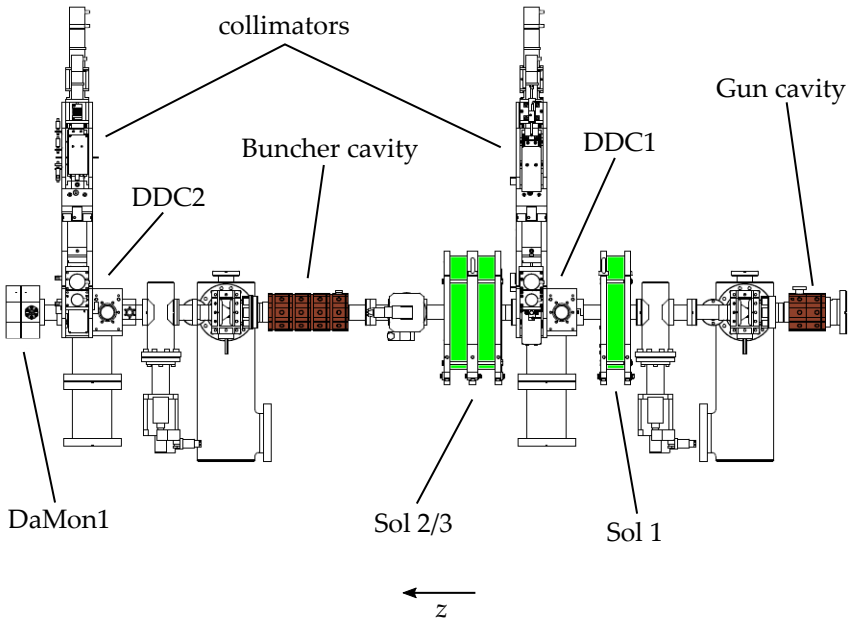

Figure 3.1: Overview of the REGAE front-end from the cathode to DaMon1. The cavities, solenoids and collimators are labeled accordingly, as are the diagnostic elements DaMon1 and the double diagnostic crosses DDC1 and DDC2. Figure adapted from [16]; courtesy of Dr. Benno Zeitler.

upstairs into the tunnel containing the actual accelerator beamline. The laser pulse is then frequency tripled by a third harmonic generation setup installed on a laser table in the vicinity of the gun cavity. Subsequently, the cathode itself is irradiated by a wavelength of 266 nm. The distance between the final lens and the cathode is approximately 50 cm.

Moreover, a motorized attenuator is located on the laser table and can be controlled remotely from the control room. By varying the level on laser beam attenuation, the resulting electron bunch charge can be adjusted to meet the requirements specified by the experimenter. A remote controlled fast shutter is also located in the path of the laser beam. The shutter is used to acquire background images of the respective detector system.

In addition to these existing elements, a beam stabilization setup has been installed for the IR and UV[1] section of the laser. Essentially, this setup is made up of two cameras and two motorized mirrors. The cameras are used to image the near- and farfield of the laser beam. Once a beam position is defined on both cameras and the effect of the motorized mirrors on the beam position is documented in terms of a transfer matrix, the motorized mirrors can be automated to adjust themselves in such a way that the beam remains in the same position on both cameras. The implementation of the stabilization setup was greatly supported by Dr. Christian Werle from the Institut für Experimentalphysik.

Within the gun cavity, the electrons produced by the cathode laser are accelerated by a longitudinal field gradient. The maximum applicable field gradient is 100 MV/m; the corresponding kinetic energy of the beam is equal to $\langle E \rangle = 5\,\mathrm{MeV}$. The second cavity, namely the buncher cavity, is located at $z = 1.36\,\mathrm{m}$ (center

1 The 266 nm wavelength falls within the ultraviolet (UV) spectrum.

position). It consists of four cells and was installed with the objective in mind of compressing the bunch length down to the order of 10 fs via the ballistic bunching mechanism outlined in section 2.2.1. Extensive studies regarding the beam arrival jitter and overall stability of the rf system can be found in [52, 53]. The desired stable operation of the cavities translates to variations of 0.01 % in amplitude and 0.01 deg in phase [52].

An important aspect to note is that buncher and gun cavity were powered by the same klystron prior to the beamline upgrade. This posed great difficulties when attempting to adjust the cavity parameters independently. In the course of the upgrade, an additional klystron system was installed for the buncher cavity, thus enabling an uncoupled operation of both cavities.

Considering the fact that the beam energy is relatively low, the use of compact solenoid magnets is sufficient in terms of beam optics. The magnetic field and the corresponding physics of the solenoid magnets at REGAE have been previously described and analyzed in [54]. While "Sol 1" in figure 3.1 is a single solenoid, "Sol 2/3" is a double solenoid consisting of two single solenoids of opposite polarity separated by a distance of 75 mm. Usually, the rotation angle θ_L induced by a solenoid, also referred to as the Larmor angle, and the focal length f are used to characterize a solenoid. In the case of a double solenoid, no rotation is present, i.e. $\theta_L = 0$ due to the fact that the Larmor angle introduced by the first solenoid is compensated by the second solenoid. The focal length can be calculated via [55, 56]

$$f = \left(\frac{e^2}{4\langle p_z \rangle^2} \int_{-\infty}^{\infty} B_z^2(z) \mathrm{d}z \right)^{-1}, \tag{3.1}$$

where $B_z(z)$ is the longitudinal component of the magnetic field of the solenoid. Using the thin lens approximation, the transfer matrix of a solenoid can be formulated based on equations 2.10 and 2.9. More precisely, a double solenoid is approximated by two thin lens matrices (one for each solenoid of the double solenoid) connected by a free drift matrix.

"Sol 1" is located in close proximity to the electron gun at $z = 0.55$ m. Due to the fact that the beam initially shows a strong transverse divergence, the main purpose of the solenoid is to collect and focus the full charge of the beam. Together with "Sol 2/3", positioned at $z = 0.93$ m, it is usually possible to find machine settings which, to a certain extent, deliver a collimated electron beam through the remainder of the beamline.

The front-end of REGAE is also equipped with two collimators. These are essentially two movable blocks of tantalum with a number of different sized holes. The collimators are especially useful for getting rid of dark current outside of the beam region. It is also possible to block the outer beam fractions, which can reduce the transverse emittance [57].

In terms of beam diagnostics, two double diagnostic crosses [58], namely DDC1 and DDC2, are implemented in the front-end section of the beamline. DDC1 is located behind the first solenoid and DDC2 is behind the buncher cavity. A Cerium-doped LYSO[2] crystal is installed as a scintillator at both diagnostic crosses as a means of measuring the transverse electron distribution of the bunch. This

2 Lutetium Yttrium Orthosilicate.

specific scintillator material was selected because of its high yield, which is equal to about 30,000 photons per MeV deposited by an incoming electron [58], and because of its short decay time of approximately 50 ns [59, 60]. A high light yield is extremely beneficial due to the fact that the electron collision stopping power [61], which is responsible for scintillation light in respective materials, is close to its minimum in the energy range of the REGAE beam [58]. The imaging optics and camera setup of DDC1 and DDC2 is described in [62]. At both diagnostic crosses the scintillator is mounted on a linear manipulator and can be moved in and out of the beamline.

Moreover, a dark current monitor labeled as "DaMon1" in figure 3.1 is installed [63]. The second dark current monitor "DaMon2" is located further downstream. DaMon1 offers a non-destructive way of measuring the total charge of the electron bunch. Originally, the resonator was developed for charge and dark current measurements at the European XFEL [64]. The electron beam induced electromagnetic fields at certain modes upon passage through the resonator. Integrated antennas detect the TM_{01} mode, of which the amplitude of the voltage is proportional to the charge of the bunch [63]. The high sensitivity of the DaMon cavities enables the measurement of electron bunch charges below 10 fC [65].

A number of small dipole magnets are also included in the front-end segment of the beamline and can be used to deflect and effectively steer the electron beam [66]. These steerers are arranged in pairs mounted orthogonal to each other, which enables both vertical and horizontal deflection of the beam. A total of eight steerers are placed throughout the beamline.

3.2 REGAE BEAMLINE UPGRADE

Behind DaMon1, the entire REGAE beamline has been rebuilt. The transport and incoupling of a high power laser into the REGAE beamline marks the main feature of the upgraded beamline. Before going into detail on the new beamline segment where electrons and laser co-propagate and travel through the same pipe, a brief description of the laser itself and its respective transport to the actual REGAE beamline will be given.

3.2.1 Laser Transport Beamline

The aforementioned laser is none other than the ANGUS laser system. The ANGUS laser laboratory is located inside a building in the vicinity of the REGAE beamline. It is a Ti:Sa based high-power laser system with a central wavelength of 800 nm which operates at a repetition rate of 5 Hz and provides pulse energies of about 5 J. This is achieved by use of the chirped pulse amplification technique [67]. The laser pulses are compressed to a FWHM[3] pulse duration of approximately 25 fs. This means that the ANGUS laser system can generate pulses with up to 200 TW. After the last compression of the pulse, the radial intensity profile is described

3 Full width at half maximum.

by a super-Gaussian distribution of eighth order. At this point, the $1/e^2$ beam diameter is equal to 76 mm.

Following the compressor, the laser beam is guided to REGAE through the Laser Transport Beamline (LTBL), which was originally developed by the LUX team [68]. While the majority of the laser system inside the ANGUS laboratory is operated in air, the compressor and the entire LTBL are part of the vacuum system. Moreover, the chambers were carefully designed with the objective of minimizing unwanted effects of external vibrations [69]. After passage through the switch yard, which allows for sending the laser beam either to the LUX or REGAE experiments, the laser is transported to the REGAE tunnel over a total distance of approximately 30 m. Along this distance, seven motorized turning mirrors, each installed in a respective turning mirror chamber, are in place. Each chamber is equipped with a diagnostics setup to monitor the nearfield position of the laser. This is accomplished by recording the leakage signal through the mirror with a camera positioned outside of the chamber behind a window flange.

Behind the seventh and final turning mirror, the chamber containing the final focusing parabola is located. Its design is based on the version installed at the LUX beamline. The effective focal length of the parabola itself is $f = 4.2\,\mathrm{m}$ with the possibility of adjusting the position of the focus by $\pm 20\,\mathrm{mm}$. The parabola is also motorized and equipped with a respective diagnostics setup.

The last mirror before the target chamber is located in the Incoupling Chamber REGAE (ICR) and referred to as the incoupling mirror. This marks the point from which laser and electron beam propagate through the same pipe. In order for the electrons to pass through the incoupling mirror when it is driven into the beamline, the mirror has a small hole of 5 mm diameter. Naturally, the hole removes a small fraction of the laser beam and has an effect on the distribution. Therefore, a second mirror with identical parameters but without a hole has been installed and may also be driven into the beamline to measure and study differences.

An overview of the incoupling section is shown in figure 3.2. The path of the ANGUS laser is colored red. Only the final section of the LTBL is shown, namely the final turning mirror chamber, labeled "CR8". The chamber housing the final focusing parabola is named "MBA". The mirror inside the ICR denoted as "holey mirror" due to the aforementioned hole for the electrons to pass through. For reasons of simplicity, the REGAE front-end (in front of the ICR) and the remaining beamline sections behind the ICR are not shown.

3.2.2 Upgraded REGAE Beamline

As mentioned in a previous section, the entire section behind DaMon1 was affected by the beamline upgrade. An overview of the upgraded beamline can be seen in figure 3.3; a description of the respective beamline components is given in the following paragraphs. The first element, namely the ICR, was described above. The holey mirror inside the ICR is located at $z = 2.70\,\mathrm{m}$. The ICR marks the beginning of the co-propagation segment. Moreover, the ICR contains various pumping ports which are vital for the differential pumping as described in [16].

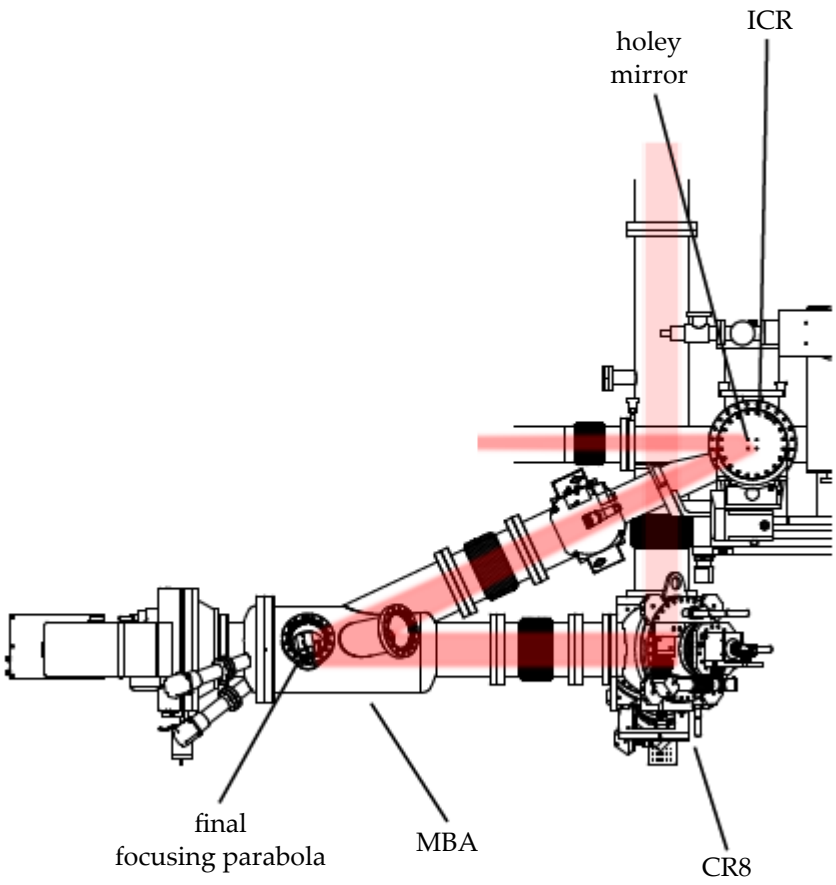

Figure 3.2: Side view of the ANGUS laser path in the incoupling section of the beamline. The final turning mirror chamber, focusing parabola and incoupling mirror are labeled accordingly. The rest of the beamline downstream of the ICR is not shown. Figure adapted from [16]; courtesy of Dr. Benno Zeitler.

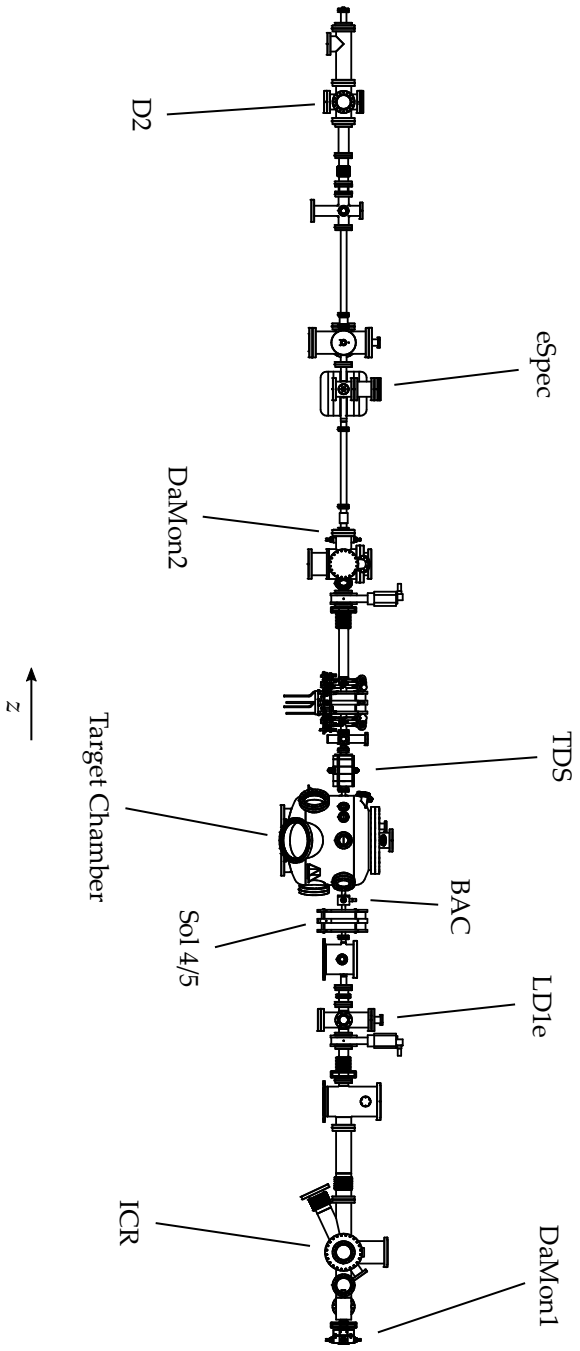

Figure 3.3: Overview of the upgraded segment of the REGAE beamline, starting at DaMon1. The REGAE front-end up to DaMon1 has been described in the previous section. The main components of the beamline are labeled accordingly. A more thorough depiction of the diagnostics section behind the target chamber is given further below. Please see the main text for a description of the individual beamline elements.

Behind the ICR at $z = 4.29\,\mathrm{m}$ lies the first diagnostic setup for both laser and electron beam. This diagnostic cross is referred to as LD1e. At LD1e, a total of three elements can be driven into the beam path with a linear manipulator. Two of these elements are scintillator screens; a fiber optic scintillator (FOS) [70] from Hamamatsu Photonics and a LYSO scintillator, which is also installed at DDC1 and DDC2.

Moving on, a further double solenoid "Sol 4/5" can be found slightly behind LD1e. While this solenoid may also be used for general adjustments of beam optics, its main intended purpose was to focus the electron beam down to a RMS spot size of approximately 10 µm. Such small beam sizes are required for the laser-plasma experiments [16].

The final element before the target chamber is the beam arrival cavity (BAC). Its main purpose is the determination of the arrival time of the electron bunch.

The new target chamber of REGAE was designed by Dr. Benno Zeitler in a way that both electron diffraction and laser-plasma experiments could be performed [16]. Its center is located at $z = 5.51\,\mathrm{m}$. The chamber itself is of cylindrical shape and has a diameter of 60 cm. Inside the target chamber there are three pillars which can be moved up and down, thus driving elements in and out of the beam path. A piezo-based linear stage and two piezo-based hexapod positioning systems are mounted on the pillars. The travel range of the hexapods in the horizontal plane is $\pm 25\,\mathrm{mm}$ and $\pm 75\,\mathrm{mm}$, and $\pm 1\,\mathrm{mm}$ in the vertical direction. A highly beneficial characteristic of the hexapod positioning devices is the fact that they offer a movement precision of only 1 nm. The hexapods are designed to carry a maximum weight of 1.7 kg.

On two of these positioning devices, namely on the linear stage and on one of the hexapods, permanent magnetic solenoids are mounted [71]. Both of the permanent solenoids are surrounded by a copper-coated iron shielding to reduce the effects unwanted stray fields may have on the electron beam. The design of the permanent magnetic solenoids and an outline of their properties is described in [72].

The hexapod mounted on the central movable pillar contains the plasma targets and various diagnostic holders. Each diagnostic holder is equipped with different diagnostic elements. FOS screens are mounted at four separate holder locations. Three of the holders are mounted in such a way that the surface of the screens is perpendicular to the beam axis in order to determine the electron beam axis. Precise knowledge of the beam axis would be required for external injection experiments. The scintillation light is recorded by a camera system located slightly behind the target chamber. In order to measure the position of the laser beam, sapphire plates have been installed in the same holders containing the FOS screens. The scintillator setups and the corresponding imaging procedure has previously been analyzed in [73].

In terms of diagnostics, an additional method of measuring the beam size has been developed [73]. The method is based on the process of determining the beam profile of a laser beam with a knife edge. This concept can also be applied to electron beams. More specifically, a scattering foil with a sharp edge is driven in to the path of the electron beam, effectively blocking a fraction of the beam. Unlike the photons of a laser pulse, the electrons are not completely stopped

but rather scattered by the material. However, the scattering rate of the electron beam into any given solid angle depends on the number of electrons that hit the scattering foil. Consequently, the electron beam size can be reconstructed by driving the scattering foil into the beam in small steps and measuring the transmitted fraction of the electron beam with a detector setup located further downstream.

Another key feature of the target chamber is the large linear manipulator mounted on top of its lid. This setup is implemented for UED experiments and contains a load-lock system to bring the respective targets into place. Two cameras are also mounted on the lid to observe the various components installed inside the target chamber.

The diagnostics section of the REGAE beamline begins immediately behind the target chamber. A schematic overview of this section is shown in figure 3.4. The first element of this section is the TDS. Its center is located at $z = 6\,\mathrm{m}$. A thorough discussion of the unique design of the REGAE TDS is given in section 4.1. The TDS exerts a time-dependent transverse force, i.e. dependent on the longitudinal position of the electron within the bunch, which leads to a change in transverse momentum. Since the resulting transverse kick is linked to the longitudinal position, the longitudinal phase space is effectively mapped onto the transverse plane. By imaging the transverse coordinates of the electron bunch on a detector screen, information on the longitudinal properties of the bunch, such as the bunch length, can be recovered with the TDS. The beam dynamics inside a TDS have been described in section 2.3.1. The total length of the cavity is comparatively short and amounts to only 270 mm, consisting of three regular cells and two end cells. It has been tuned to a frequency of 2.998 MHz just like the gun and buncher cavity. A maximum deflecting voltage of 190 kV can be achieved with the current setup.

A further diagnostic cross is located behind the TDS at $z = 6.17\,\mathrm{m}$. This diagnostic cross is referred to as "QSQ". The imaging system for the beamline diagnostics inside the target chamber is housed within the QSQ setup. Moreover, a FOS and a LYSO scintillator screen are installed at this location. A sapphire plate for determining the position of the laser beam is also included. The generated light is reflected towards a camera by a mirror attached behind the holder.

Two quadrupole magnets are positioned behind QSQ. The quadrupoles were installed with the intention of imaging the electrons from the laser-plasma experiments. A distance of 260 mm lies between the quadrupoles. Within this space, the final double solenoid, denoted as "Sol 6/7", is located. It is identical to the aforementioned solenoids Sol 4/5 and Sol 2/3. Sol 6/7 plays an indispensable role for emittance measurements [57] and diagnostics with the TDS.

The next element in the REGAE beamline is the main laser diagnostic LD2. Similarly to the ICR, the LD2 chamber contains a holey mirror and a regular mirror without a hole. The laser beam is sent towards a diagnostics table. It should be noted that the diagnostic setup itself is still under construction. A second dark current monitor, referred to as DaMon2, is installed behind the LD2 chamber. DaMon2 may be utilized to measure and verify the charge of the electrons accelerated in the course of the external injection experiments. In

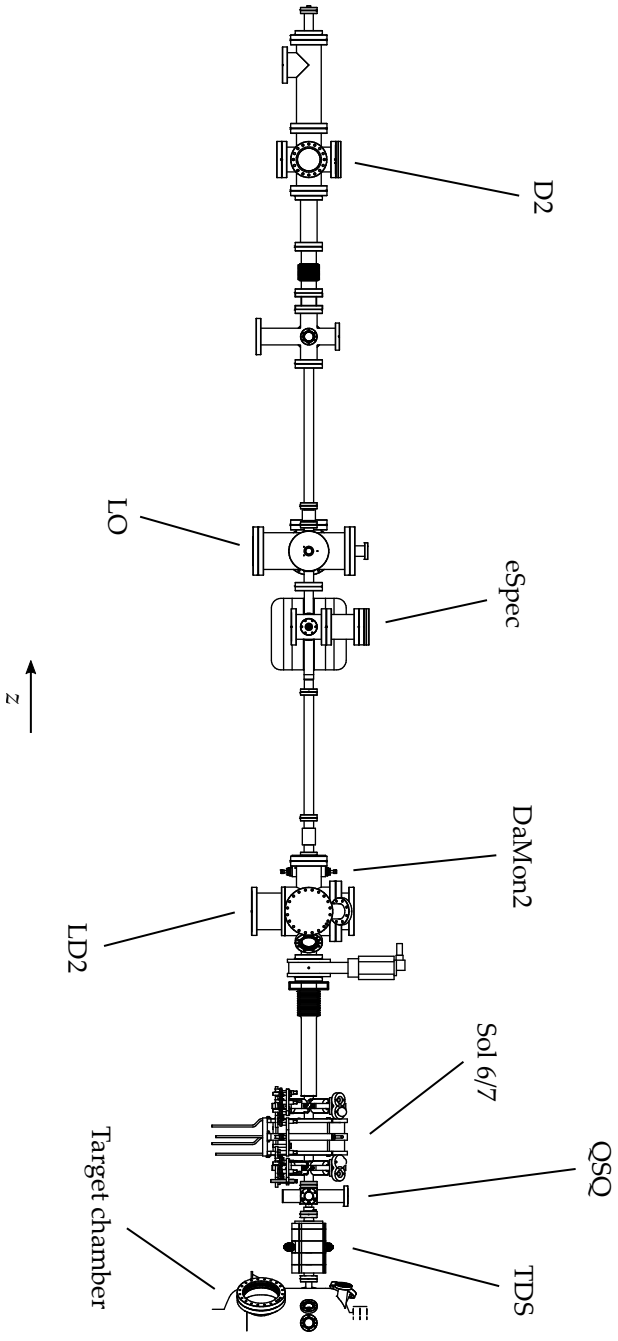

Figure 3.4: Overview of the diagnostics section of the REGAE beamline starting at the exit of the target chamber. The main diagnostic devices are labeled accordingly. Please see the main text for a description of each specific element.

practice, the DaMon2 cavity has proven to be extremely useful in context of guiding the electron beam through the beamline.

Naturally, a method to measure the energy of the particle beam is crucial for any accelerator. A dispersive element is installed at REGAE for precisely this purpose. The spectrometer magnet at REGAE is based on a corrector magnet originally implemented at the Hadron Electron Ring Facility (HERA), located also on the DESY campus. The uniform and vertical magnetic field of the magnetic dipole deflects the electrons by an angle of 90 deg in the horizontal plane towards a detector screen.

The dispersion relations can be derived using the relations obtained from the beam optics formalism as described in section 2.1. For off-momentum particles, the equation of motion as given in equation 2.6 is modified to

$$\frac{\mathrm{d}^2 x_\mathrm{p}(z)}{\mathrm{d}z^2} + K_x(z) x_\mathrm{p}(z) = \frac{\delta p}{\rho(z)}, \tag{3.2}$$

where the parameter $\rho(z)$ denotes the bending radius of the dipole magnet. To be more precise, the complete solution of the equation of motion is a sum of the (unmodified) homogeneous equation 2.6, which describes on-momentum particles, and the inhomogeneous equation above, which describes off-momentum particles. While a general solution can be calculated with perturbation theory using Green's functions, it is possible to find a simplified solution for the case of a constant bending radius $\rho(z) = \text{const.}$ of the dipole [74]. The equation of motion then transforms to

$$\frac{\mathrm{d}^2 x_\mathrm{p}(z)}{\mathrm{d}z^2} + \frac{x_\mathrm{p}(z)}{\rho^2} = \frac{\delta p}{\rho}. \tag{3.3}$$

A basic particulate solution is simply given by $x_\mathrm{p}(z) = \rho \cdot \delta p$ and the complete solution can be written as

$$x(s) = x_0 \cos\left(\frac{s}{\rho}\right) + x_0' \rho \sin\left(\frac{s}{\rho}\right) + \rho \cdot \delta p \cdot \left(1 - \cos\left(\frac{s}{\rho}\right)\right) \tag{3.4a}$$

$$x'(s) = -\frac{x_0}{\rho} \sin\left(\frac{s}{\rho}\right) + x_0' \cos\left(\frac{s}{\rho}\right) + \delta p \sin\left(\frac{s}{\rho}\right). \tag{3.4b}$$

Considering the fact that the deflection angle of the spectrometer dipole at REGAE is equal to 90 deg, the horizontal transfer matrix is given by the expression

$$\mathcal{M}_\mathrm{dipole} = \begin{pmatrix} 0 & \rho & \rho \\ -\frac{1}{\rho} & 0 & 1 \\ 0 & 0 & 1 \end{pmatrix}. \tag{3.5}$$

It follows that the deviations within the dipole magnet are equal to $\Delta x_\mathrm{dipole} = \rho \cdot \delta p$ and $\Delta x'_\mathrm{dipole} = \delta p$. Due to the presence of a short drift distance L between the exit of the dipole magnet and the actual detector screen, the offset between off-momentum particles is additionally increased by $\Delta x_\mathrm{drift} = L \Delta x'_\mathrm{dipole}$. As a result, the cumulative offset on the detector screen Δx_det is given by

$$\Delta x_\mathrm{det} = \Delta x_\mathrm{dipole} + \Delta x_\mathrm{drift} = (\rho + L) \cdot \delta p = D_x \delta p, \tag{3.6}$$

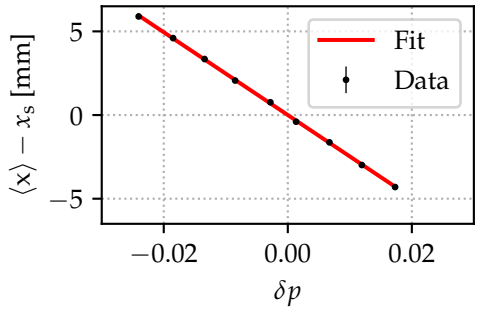

Figure 3.5: Measured calibration curve for the dipole spectrometer installed at the REGAE beamline. The position of the beam centroid $\langle x \rangle$ with respect to the screen center x_s is plotted as a function of the relative momentum deviation δp. A linear fit (red) has been applied to the data (black).

where D_x denotes the dispersion.

A measurement of the dispersion has been carried out. In the center of the screen, the correlation between the momentum p_z and the dipole current I is given by

$$\langle p_z \rangle [\mathrm{MeV}] = 4.3 \frac{\mathrm{MeV}}{\mathrm{A}} \cdot I[\mathrm{A}] + 0.054\,\mathrm{MeV}. \tag{3.7}$$

The relation above has been previously determined based on ASTRA simulations using field maps measured at various dipole currents. The dispersion relation can be obtained by measuring the beam centroid on the detector screen as a function of the beam momentum. Equivalently, a scan of the dipole current can be performed, as each current can be associated with a respective momentum value according to equation 3.7. Such a calibration curve for the dipole spectrometer at REGAE is given in figure 3.5, where the mean beam position $\langle x \rangle$ with respect to the center x_s of the detector screen ($\Delta x_{\mathrm{det}} = \langle x \rangle - x_s$) is shown as a function of the relative momentum deviation $\delta p = (p_z - \langle p_z \rangle)/\langle p_z \rangle$. Thus, the dispersion can be derived from a linear fit to the data and is equal to $|D_x| = (247.45 \pm 0.95)\,\mathrm{mm}$. The data are well described by a linear function. The evident negative slope results from a horizontal flip of the recorded camera images.

The resolution of the dipole spectrometer can be roughly estimated using D_x. Using $x_{\mathrm{RMS}} \approx 40\,\mu\mathrm{m}$ as an estimate for the horizontal beam size, taken from ASTRA simulations using standard operating parameters of the beamline, the ratio of beam size to screen distance results in $x_{\mathrm{RMS}}/D_x \approx 1.61 \cdot 10^{-4}$ as an estimate for the resolution of the spectrometer.

The screen installed in the spectrometer is a FOS and is imaged by an intensified CCD camera. The scintillator screen has the dimensions $50 \times 50\,\mathrm{mm}^2$, although the active area is reduced to $47 \times 47\,\mathrm{mm}^2$. Behind the scintillator, a silicon wafer with an aluminum coating is installed. The mirror reflects the scintillation light by 90 deg and onto a camera. The installed camera is an Andor EMCCD[4] iXon-885 camera [75]. The camera chip has a size of $8 \times 8\,\mathrm{mm}^2$ with pixels of $8 \times 8\,\mu\mathrm{m}^2$ in size. A overview of the basic properties of this camera is presented in table 3.1.

4 Electron multiplying charge-coupled device.

Property	Andor iXon 885	Andor iXon 888
Chip size [mm]	8×8	13×13
Pixel size [µm]	8×8	13×13
Active pixels	1002×1004	1024×1024
Frame rate $[\frac{\text{frames}}{\text{s}}]$	31.4	8.9
Pixel well depth $[e^-]$	≈ 30000	≈ 80000

Table 3.1: Summary of some of the basic properties of the Andor iXon 885 and Andor iXon 888 camera models. Data taken from [76].

Due to the fact that a small fraction of the ANGUS laser passes through the hole in LD2, an additional and final mirror is installed inside the laser out (LO) chamber. It is located behind the spectrometer dipole. The mirror deflects the laser beam out of the REGAE beamline. The main purpose of this setup is to prevent any and all damage the ANGUS laser might inflict on the beamline segment behind LO. Especially potential damage to the sensitive detector system should by prevented this way.

The detector system D2 at REGAE was designed by Hossein Delsim-Hashemi. Located at $z = 10.58\,\text{m}$, it marks the end of the beamline. A FOS of the same format as installed at the spectrometer is used at D2, i.e. the active area is equal to $47 \times 47\,\text{mm}^2$. The orientation of the FOS is perpendicular to the beam axis and the scintillation light, as it is the case at the other diagnostic setups, is deflected by 90 deg towards the camera. At this specific setup, an Andor iXon 888 camera model is installed. A comparison of the basic properties between both Andor iXon 885 and Andor iXon 888 camera models can be found in table 3.1. Cooling is applied to reach an operation temperature of $-70\,°\text{C}$, at which a quantum efficiency of approximately 0.925 is achieved. Here the term "quantum efficiency" denotes the ratio between the number of charge carriers collected by the device and the number of incident photons. Quantum efficiency can hence be used to indicate the detector's sensitivity to light. It should be noted that the quantum efficiency strongly depends on the wavelength of the incident photons. For the Andor iXon 888 camera, the quantum efficiency reaches it maximum at a wavelength of 540 nm, which is in accordance with the scintillation light generated by the scintillation material of the FOS [77].

As a precautionary measure, a lead shielding is placed in front of the camera to block any scattered high-energy photons that might originate from the beginning of the beamline. Moreover, the detector setup has been optimized to achieve an exceptionally high charge sensitivity while retaining a reasonable spatial resolution. Previous tests performed with this detector setup have confirmed the ability to detect single electrons [78]. Details regarding the efficiency of the detector system can be found in [79].

Photons generated by the FOS placed in the propagation path of the electron beam, i.e. scintillation light, is deflected by a mirror onto the CCD chip where it excites an electron. The quantum efficiency of the chip material, as described in the section above, is the governing limitation of this process. Each row of pixels is then read out pixel by pixel and the signal is digitalized in an analog-digital

converter to 14-bit or 16-bit as specified by the user. It should be noted that if the EM gain is activated, the amplification of the signal is carried out before its digitalization. This has the advantage of avoiding an increase of readout noise by the applied EM gain, which would occur if the signal amplification took place in the analog-digital converter.

In order to reduce noise from thermal excitation on the CCD chip, a form of cooling is necessary. Therefore, the chip is mounted on a thermoelectric cooler. This enables the chip to be cooled down via the thermoelectric effect [80]. The cooler has a cold end and a hot end, from where the heat is dissipated either via air cooling in form of a fan or water cooling, with which temperatures down to $-95\,°C$ can be reached. At REGAE, air cooling to $-70\,°C$ is sufficient. The CCD chip is mounted inside a vacuum housing. The incoming photons enter the housing through a window equipped with an anti-reflection coating to reduce losses in intensity.

It has previously been shown that due to the high sensitivity of the Andor camera, the main sources of noise are shot noise of the signal and background [79]. The consequent image processing technique is described in section 4.2.2 and is partially based on previous work presented in [79].

4 BUNCH LENGTH MEASUREMENTS WITH THE REGAE TDS

The longitudinal parameters of a particle bunch, for example the bunch length, are a crucial piece of information with respect to operating a particle accelerator and related experiments. Transverse deflecting structures constitute a possible diagnostic device in order to investigate the longitudinal phase space of charged particle beams. By shearing the particle bunch, a TDS effectively maps the longitudinal coordinate to a transverse coordinate, which can then easily be measured with the help of a scintillator screen. The versatility of a TDS is complemented by the ability to perform single-shot bunch length measurements at a high longitudinal resolution. For these reasons, deflecting structures are a commonly used device for longitudinal phase space diagnostics.

In order to cope with the high quality electron beam of the REGAE accelerator, a unique TDS has been specifically designed for the beamline [9]. The fundamental considerations which ultimately lead to the cavity design are discussed in the following section and based on [44]. The TDS was installed at the REGAE beamline in 2018.

The general operation of the TDS and the subsequent measurement procedure in outlined in detail in section 4.2, along with the typical machine setup process. This includes the calibration of the structure in order to determine the shear parameter, which is required for the bunch length reconstruction. Experimental results of bunch length measurements for an uncompressed electron bunch and for the ballistic bunching mechanism are presented in section 4.3.3 and 4.3.4, respectively.

4.1 DESIGN OF THE REGAE TDS

The transverse rf deflecting cavity at REGAE has been installed with the primary objective of performing diagnostic measurements of the longitudinal parameters of the electron bunch. It is the first TDS to have been developed and optimized for bunch rotation [9]. The cavity is characterized by a minimized level of aberrations in the field distribution along with an improvement in rf efficiency [43]. The following contains basic considerations regarding the unique design of the REGAE TDS and is based on [44].

Generally speaking, there are a number of parameters which were of particular interest in context of design considerations (and limitations) of the REGAE TDS. First and foremost, it must be mentioned that the REGAE accelerator is capable of producing a particle beam with very small emittance values. From an experimental standpoint, it is of interest to preserve the beam quality. In other words, the emittance growth induced by the TDS itself should be reduced as much as reasonably possible. Furthermore, attention must be drawn to the fact that the REGAE beamline is typically operated at cavity settings which provide mean beam

energies in the range of 3 to 5 MeV, i.e. $|\vec{v}| < c$. The longitudinal motion of the electrons within the bunch must also be considered upon passage through the TDS.

Last but not least, the power source of the cavity is a decisive factor, as this dictates the strength of the shear parameter S and thus directly impacts the resolution of the structure. A distinct feature of the TDS at the REGAE beamline is the fact that it is driven only by an amplifier and not by a separate modulator. On the one hand, this typically implies a smaller rf power and therefore a smaller shear parameter during operation of the TDS. On the other hand, substituting a potentially expensive modulator setup and associated waveguide system with a comparatively cheap amplifier greatly reduces financial expenditures. The amplifier used for the TDS can provide an output power of $P_0 = 5\,\mathrm{kW}$, which produces an effective deflecting voltage of $V_0 = 190\,\mathrm{kV}$ in the structure. Furthermore, the cavity has a shunt impedance of $Z_{\mathrm{TDS}} = 7.58\,\mathrm{M\Omega}$ and a calculated quality factor of $Q_{\mathrm{TDS}} = 12550$ [9].

Following the explanation presented in section 2.3.1, for the sake of longitudinal diagnostics a TDS is typically operated at a phase where the central particle of the bunch does not experience any deflection. While this is reflected in the derivations presented in the aforementioned section, it must be noted that this is a purely idealized case. In reality, the central particle will generally exit the TDS with a transverse offset and/or angle and it is not possible to counteract this by operating the cavity at a respective phase [44, 81]. Several reasons can be identified for this behavior.

In a periodic standing wave TDS, where the transverse fields in first order can be expressed by the fundamental spatial harmonics

$$\begin{aligned} \mathcal{E}_y(z,t) &= \mathcal{E}_0 \sin(kz)\cos(\omega t + \varphi) \\ B_x(z,t) &= -B_0 \cos(kz)\sin(\omega t + \varphi) \end{aligned} \tag{4.1}$$

with the wave number k, angular frequency ω and amplitudes B_0 and $\mathcal{E}_0$, the electrons of the bunch interact with the counterpropagating wave, which leads to an offset

$$\Delta y = \frac{e(\mathcal{E}_0 + c\beta_z B_0)\cos(2kz_0)}{4ckp_z} L_{\mathrm{TDS}} \tag{4.2}$$

for an electron propagating with matched energy through the TDS [44]. In the above equation, L_{TDS} denotes the length of the deflecting structure, p_z and β_z are the longitudinal momentum and normalized velocity and the integration constant z_0 is chosen to satisfy $p_y = 0$ and corresponds to the entrance of the cavity. The offset as written in equation 4.2 is not present in traveling wave structures.

Higher spatial harmonics pose an additional contribution to transverse kicks at the entrance and exit of the TDS and therefore lead to transverse oscillations of particles in the bunch [42, 82]. The transverse oscillations of a particle, induced by the counterpropagating wave and higher spatial harmonics, lead to a reduction of the longitudinal component of the particle's velocity. This in turn causes phase slippage between the particle and the rf wave. The resulting phase difference leads to an additional offset, which can be written as

$$\Delta y = \frac{eV_0 L_{\mathrm{TDS}}^2}{12 p_z c}\frac{\partial \varphi}{\partial z} = \frac{eV_0 k_0(\beta_m - \beta_z)}{12 p_z c} L_{\mathrm{TDS}}^2, \tag{4.3}$$

where $\frac{\partial \varphi}{\partial z} = k_0(\beta_m - \beta_0)$ describes the differential phase deviation for a structure matched to β_m and k_0 denotes the wave number in vacuum [44]. Naturally, this contribution vanishes if the TDS is matched to the velocity of the electrons.

Due to the fact that the REGAE beamline provides beam energies in the order of a few MeV, the longitudinal motion of the particles must also be considered. For a particle traveling through the TDS with a transverse offset Δy with respect to the reference particle propagating along the axis of the structure, the resulting longitudinal shift can be calculated similar to equation 2.39:

$$\Delta\zeta(z) = \int_{z_0}^{z} \frac{\Delta\beta(\Delta y, z')}{\beta} \mathrm{d}z'. \tag{4.4}$$

In the above equation, $\Delta\beta(\Delta y, z)$ denotes the velocity difference between the two particles. In first order, this expression can be formulated as

$$\Delta\zeta(z) = \int_{z_0}^{z} \frac{1}{\beta}\frac{\partial\beta}{\partial\gamma}\Delta\gamma(\Delta y, z')\mathrm{d}z' = \int_{z_0}^{z} \frac{\Delta E(\Delta y, z')}{cp\beta\gamma^2}\mathrm{d}z', \tag{4.5}$$

where $\Delta E(\Delta y, z)$ describes the energy difference. According to [44], the integral can be computed to yield

$$\Delta\zeta(z) = -\frac{ekV_0\Delta y z^2}{2cp\beta\gamma^2 L_{\mathrm{TDS}}} \tag{4.6}$$

for $z \in [0, L_{\mathrm{TDS}}]$ if the TDS is operated at the zero-crossing phase. For simplicity, the entrance of the TDS has been chosen as $z_0 = 0$. Thus, after passage through the TDS, the bunch length has increased according to

$$\zeta_{\mathrm{RMS}} = \sqrt{\zeta_{0,\mathrm{RMS}}^2 + \left(\frac{eV_0 k L_{\mathrm{TDS}} y_{\mathrm{RMS}}}{cp_z\beta\gamma^2}\right)^2}, \tag{4.7}$$

where $\zeta_{0,\mathrm{RMS}}^2$ denotes the unperturbed bunch length and the second term in the square root portrays the bunch lengthening effect ascribable to the longitudinal particle motion within the TDS. The shift itself along the longitudinal axis depends on the transverse offset Δy relative to an on axis particle. As a result of the bunch lengthening effect, the transverse momentum in streaking direction receives a further contribution dependent on the transverse position of the particle [44]. This means that the electron bunch experiences transverse defocusing.

Another key aspect is the fact that a longitudinal field gradient arises from the transverse fields in a TDS (see equation 4.1) as a result of Maxwell's equation $\vec{\nabla} \times \vec{\mathcal{E}}(\vec{r}, t) = -\partial_t \vec{B}(\vec{r}, t)$. While this field gradient can be set to zero on the central axis, the particles traveling through the structure with an offset in streaking direction induce an uncorrelated energy spread $E_{\mathrm{RMS,u}}$ according to

$$E_{\mathrm{RMS,u}} = ekV_0 y_{\mathrm{RMS}} \tag{4.8}$$

if the structure is operated at the zero-crossing phase [8]. Since the uncorrelated energy spread exhibits the same dependencies as the inverse longitudinal resolution $1/R_z$ as derived in section 2.3.2, there is no free parameter left optimization in term of the cavity design [44]. In addition to this, a linear correlated energy

spread is also induced if the transverse particle motion during passage through the TDS is considered. For a structure operated at zero-crossing, a correlated energy spread $E_{\mathrm{RMS,c}}$ written as

$$E_{\mathrm{RMS,c}} = \frac{e^2 k^2 V_0^2 \zeta_{\mathrm{RMS}} L_{\mathrm{TDS}}}{6 c p_z} \tag{4.9}$$

is built up in the TDS [8].

A shorter deflecting structure is advantageous to minimize the unwanted effects listed above, since all (except for the induced uncorrelated energy spread) scale with the length of the TDS. However, one critical drawback of shorter structures is the established fact that the efficiency regarding the necessary rf power to produce the deflecting field is reduced in comparison to structures of larger length [82]. This problem becomes particularly pronounced for deflecting structures operated in traveling wave mode, where the rf wave is subject to attenuation as a result of power dissipation in the boundary walls of the structure. For an S-band cavity such as the TDS installed at REGAE, operation in standing wave mode is considered to be more effective.

Taking this into consideration, the TDS at REGAE was designed to satisfy the following conditions [9]:

1. the length of the structure should be kept small, while providing
2. a linear deflecting field with
3. high rf efficiency.

At this point, some further remarks regarding the description of the deflecting fields are in order. Ultimately, an electromagnetic field in vacuum is characterized by Maxwell's equations

$$\begin{aligned}
\vec{\nabla}\vec{\mathcal{E}}(\vec{r},t) &= 0 \\
\vec{\nabla}\vec{B}(\vec{r},t) &= 0 \\
\vec{\nabla}\times\vec{\mathcal{E}}(\vec{r},t) &= -\frac{\partial \vec{B}(\vec{r},t)}{\partial t} \\
\vec{\nabla}\times\vec{B}(\vec{r},t) &= \epsilon_0\mu_0\frac{\partial \vec{\mathcal{E}}(\vec{r},t)}{\partial t}.
\end{aligned} \tag{4.10}$$

Two independent variables are needed to give a complete description of the field distribution. It is common practice to select the longitudinal components of the electric and magnetic field for this purpose. Based on the assumption that the time-dependence is proportional to $\exp(i\omega t)$, the relations

$$\begin{aligned}
\frac{\partial^2 \mathcal{E}_r}{\partial z^2} + k^2 \mathcal{E}_r &= \frac{\partial^2 \mathcal{E}_z}{\partial r \partial z} - \frac{i\omega n}{r} B_z \\
\frac{\partial^2 \mathcal{E}_\theta}{\partial z^2} + k^2 \mathcal{E}_\theta &= -\frac{n}{r}\frac{\partial \mathcal{E}_z}{\partial z} + i\omega \frac{\partial B_z}{\partial r} \\
\frac{\partial^2 B_r}{\partial z^2} + k^2 B_r &= -\frac{ikn}{cr}\mathcal{E}_z + \frac{\partial^2 B_z}{\partial r \partial z} \\
\frac{\partial^2 B_\theta}{\partial z^2} + k^2 B_\theta &= -\frac{ik}{c}\frac{\partial \mathcal{E}_z}{\partial r} + \frac{n}{r}\frac{\partial B_z}{\partial z}
\end{aligned} \tag{4.11}$$

can be deduced from Maxwell's equations written in cylindrical coordinates (r, θ, z) with $\{\mathcal{E}_z, \mathcal{E}_r, B_\theta\} \propto \cos(n\theta)$ and $\{B_z, B_r, \mathcal{E}_\theta\} \propto \sin(n\theta)$ [45]. This field description in terms of transverse electric and magnetic waves (TE and TM) is commonly encountered in the literature [25, 83]. A general discussion on the representation of fields in vacuum with cylindrical symmetry can be found in [84].

It has previously been established that the exclusive use of the TE-TM basis is not feasible for the description of transverse deflecting structures [44, 82]. To overcome this problem, a new hybrid basis with hybrid electric and hybrid magnetic (HE and HM) waves was introduced [84, 85]. Compared to the TE-TM basis, one major difference is that the longitudinal field components $\mathcal{E}_z$ and B_z now depend on each other. In the HE-HM basis, the fields in a TDS can be described by a superposition of HE and HM waves of the form

$$\begin{aligned} \vec{\mathcal{E}}(\vec{r}, t) &= a\vec{\mathcal{E}}_{\mathrm{HE}}(\vec{r}, t) + b\vec{\mathcal{E}}_{\mathrm{HM}}(\vec{r}, t) \\ \vec{B}(\vec{r}, t) &= a\vec{B}_{\mathrm{HE}}(\vec{r}, t) + b\vec{B}_{\mathrm{HM}}(\vec{r}, t), \end{aligned} \tag{4.12}$$

where the coefficients of the superposition are essentially defined by the geometry of the TDS.

For relativistic particles with $\beta_z \to 1$, the deflecting force from the main spatial harmonic in a TDS is constant. This simplification was the basis for the derivations in section 2.3.1. Additional nonlinear components arise for the general solution of the deflecting fields, which have been discussed in [44]. The primary origin of nonlinearities in the transverse components are higher spatial harmonics. For a TDS which deflects particles along the vertical y-axis, the transverse components of the force for the nth spatial harmonic in the vicinity of the z-axis are given by

$$\begin{aligned} F_{x,n} &\approx \frac{ek_n(a_n + b_n)\tilde{e}_{z,n}}{2} \left(k_n^4(x^3y + xy^3) + \dots\right) \\ F_{y,n} &\approx \frac{ek_n(a_n + b_n)\tilde{e}_{z,n}}{2} \left(1 + \frac{k_n^2(x^2 + y^2)}{4} + \dots\right), \end{aligned} \tag{4.13}$$

where $\tilde{e}_{z,n}$ denotes the longitudinal field component and a_n and b_n correspond to the coefficients as defined in equation 4.12. The wave vector k is connected to k_n via the relations

$$k_n^2 = |k_{z,n}^2 - k^2| \quad \text{and} \quad k_{z,n} = \frac{k(\psi_0 + 2\pi n)}{\beta_z \psi_0} \tag{4.14}$$

with ψ_0 as the phase advance at which the TDS is operated.

From equation 4.13 it follows that the contributions from higher harmonics vanish only for $a_n \simeq -b_n$. In a "conventional" disk-loaded waveguide structure, such as the LOLA TDS [40], higher harmonics can be effectively reduced by increasing the aperture of the iris [43], which balances the HE and HM components in equation 4.12. Unfortunately, the radius of the iris aperture is effectively the only degree of freedom that can be optimized in a disk-loaded waveguide structure, and while the increase does lead to $a \simeq -b$, it also causes a loss in rf efficiency.

In order to preserve a high efficiency while attempting to balance the field components, the control of the rf parameters of the TDS needs to be decoupled

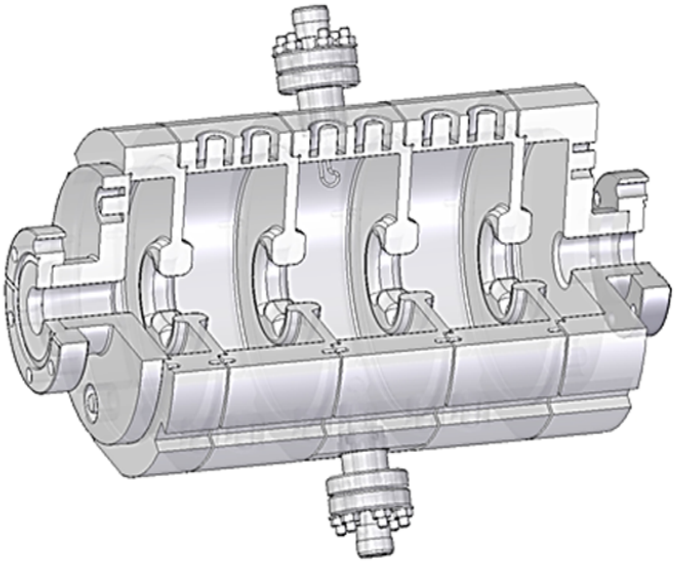

Figure 4.1: Technical drawing of the deflecting structure with minimal level of aberrations. The interior of the cavity can be seen.

from the control of the field distribution inside the TDS [86]. This requires the development of structures with a more complex layout.

Ultimately, the design of the decoupled REGAE TDS is a result of these considerations regarding efficiency and linearity of the electromagnetic fields, i.e. a minimal level of aberrations [9]. A technical drawing of the TDS is shown in figure 4.1. In contrast to a disk-loaded waveguide structure with a round iris in the center, the shape of the aperture in the REGAE TDS is more complex. The circular outline of the iris is "disturbed" by a protruding section of material. In a decoupled structure, the deflecting field depends on the combination of the unperturbed aperture radius and on the effective window radius between the protruding sections.

The unique cell design of the REGAE TDS is depicted in figure 4.2, where a single cell of the deflecting structure can be seen. More specifically, one of the three regular cells is shown. The beam axis matches the cylinder axis through the center of the aperture. In order to meet the three conditions listed above, extensive numerical simulations and modifications of the properties of the aperture have been performed previously [87].

Naturally, the sophisticated cell design poses more difficulties to the machining of the structure as compared to a LOLA-type TDS. This comes as the price for the improved rf efficiency. In order to evaluate and select an appropriate machining technology, a number of test cells were manufactured. The production took place at the Center for the Advancement of Natural Discoveries using Light Emission (CANDLE) in Armenia [88]. Further details regarding the results obtained with the test cells, further design properties of the structure and of the cavity rf probes can be found in the technical report [87].

Following the satisfactory results provided by the test cells, the actual copper cells of the TDS were manufactured [87]. One such cell can be seen in figure 4.2. The cavity was brazed and tuned to a frequency of 2.998 MHz. A picture of

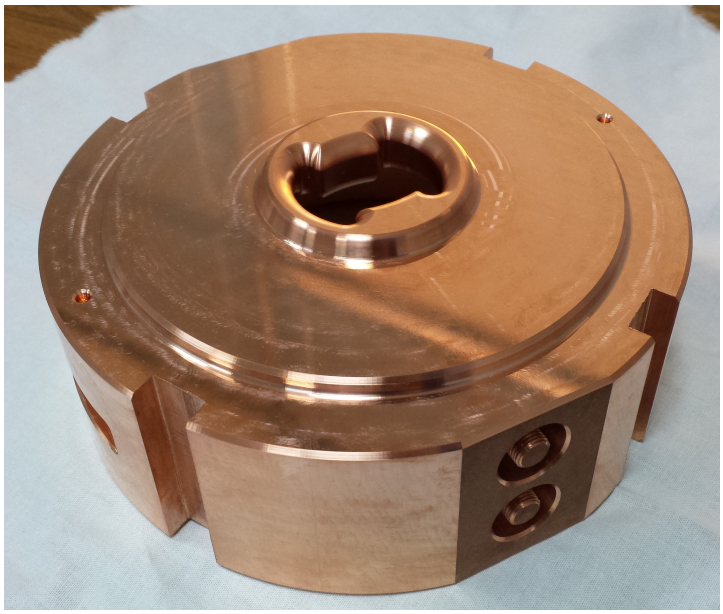

Figure 4.2: Picture of a cell of the REGAE TDS. The particular shape of the aperture can be seen.

TDS property	Value
ν_{TDS} [GHz]	2.998
L_{TDS} [mm]	270
P_0 [kW]	5
V_o [kV]	190
Q_{TDS} (calculated)	12550
Z_{TDS} [MΩ]	7.58

Table 4.1: Overview of cavity design parameters of the REGAE TDS; table adapted from [9].

the TDS after brazing can be seen in figure 4.3. The larger flange located on the central axis of the TDS connects the structure to the beam pipe. The rf probe is inserted via the small flange as seen at the top of the image.

Moreover, table 4.1 lists the main parameters of the deflecting structure. The TDS consists of three regular cells and two end cells at the entrance and exit of the cavity. Installation of the deflecting structure into the REGAE beamline took place in course of the extensive beamline upgrade as described in section 3.2.2 with support from the DESY vacuum group [89]. A picture showing the installed TDS can be seen in figure 4.4.

For the purpose of further classifying the REGAE TDS and putting its unique design into perspective, it is helpful to compare the structure operated at REGAE to different transverse deflecting cavities installed at other research facilities. As previously mentioned, iris-loaded transverse deflecting rf cavities were first constructed at SLAC in the 1960s. This particular type of cavity is commonly referred to as LOLA-type structure, owing chiefly to the names of its inventors

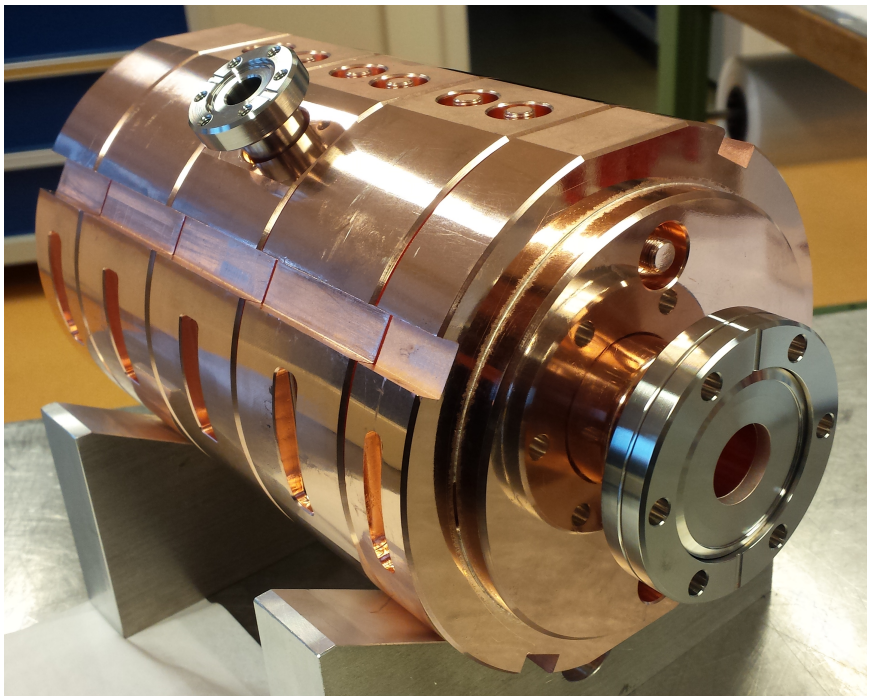

Figure 4.3: Image of the brazed deflecting cavity before installation into the REGAE beamline.

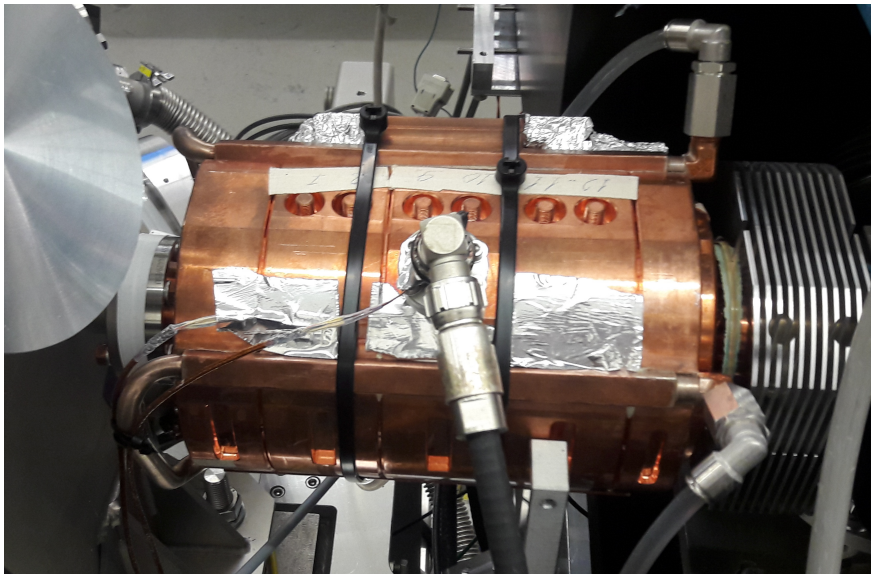

Figure 4.4: Side view of the transverse deflecting structure after installation into the REGAE beamline as part of the beamline upgrade. The electrons propagate from left to right. The entrance flange of the TDS is connected to the target chamber, part of which can be seen on the left side of the image. The exit flange of the TDS is connected to the QSQ diagnostic cross. A steerer magnet is clamped over the exit flange and can be seen on the right side of the image.

G. A. Loew, R. R. Larsen and O. A. Altenmueller [38]. A prime example for a LOLA-type structure is the TDS currently installed in the FLASH linear accelerator as part of collaboration between DESY and SLAC [40, 90]. This TDS is a normal conducting rf structure consisting of copper and was originally built at SLAC in 1968 and transferred to the FLASH beamline in 2003 [91]. It has a total length of $L_{\mathrm{TDS}} = 3.64\,\mathrm{m}$, which is larger by more than a factor of ~ 10 compared to the REGAE TDS with $L_{\mathrm{TDS}} = 0.27\,\mathrm{m}$. The structure is comprised of a number of cylindrical copper cells, each measuring 3.5 cm in length.

This TDS is a disk-loaded structure with an iris radius of 2.24 cm and a disk thickness of 0.58 cm. Essentially, the design of the structure was dictated by the objective to achieve a phase velocity of the fundamental spatial harmonic equal to c [92]. Similar to the REGAE TDS, the LOLA TDS is operated in the S-band frequency range, but at a value of $\nu = 2.856\,\mathrm{GHz}$, which is lower than the frequency used at REGAE ($\nu = 2.998\,\mathrm{GHz}$). It should be noted that the design frequency could not be matched to a multiple of the FLASH master oscillator, since the LOLA-TDS was originally constructed for a different accelerator. Because of this, the operating temperature of the cavity was adapted in order to slightly shift the resonance frequency and thus enable synchronization [93].

As suggested earlier in this section, a distinct feature of the REGAE TDS is the absence of a costly dedicated rf system. The rf pulses for the LOLA-TDS at FLASH are generated in a separate modulator. After amplification by a klystron, the rf pulse is subsequently transported through a waveguide system spanning a total length of approximately 75 m. The waveguide system is operated at the same temperature as the TDS. The maximum input power is equal to 25 MW, which produces a deflecting voltage of $\approx 29\,\mathrm{MV}$ [8]. The rf input power at the REGAE TDS is only 5 kW[1]. Moreover, the typical mean beam energy at the position of the LOLA-TDS at FLASH is equal to $\langle E \rangle = 500\,\mathrm{MeV}$, which is again higher than a factor of ~ 10 compared to the typical mean beam energies measured at the REGAE beamline. Despite the fact that there are nonlinear terms in the deflecting force arising due to $\beta < 1$, these additions are proportional to $1/(\beta^2\gamma^2)$ and are thus suppressed for higher energies [82]. However, the nonlinearities resulting from higher spatial harmonics are in principle still present. These unwanted perturbations are eliminated by the concrete design of the LOLA-TDS. More specifically, the iris radius has been adapted to satisfy $a \simeq -b$ (see equation 4.12). The consequent reduction of the rf efficiency is remedied by the high input power available for the operation of the TDS. An overview of the main LOLA TDS parameters is given in table 4.2.

A novel type of transverse deflecting rf structure allows the user to arbitrarily select the streaking direction. Cavities of this type are referred to as PolariX TDS and are operated in the X-band frequency range ($\nu \approx 12\,\mathrm{GHz}$). Originally, the PolariX was designed for the Compact Linear Collider (CLIC) at CERN [94]. Further developments of the structure were carried out in a collaboration between DESY, CLIC and the Paul Scherrer Institut (PSI) located in Switzerland [95]. Such cavities are (planned to be) installed at various accelerator beamlines, such as FLASH2

1 The amplifier has recently been replaced by a model providing up to 10 kW.

TDS property	Value
ν_{TDS} [GHz]	2.856
L_{TDS} [m]	3.64
P_0 [MW]	25
V_o [MV]	29

Table 4.2: Overview of cavity parameters of the LOLA TDS installed at the FLASH beamline [93].

and FLASHFORWARD [96, 97], SWISSFEL [98] and at the Accelerator Research Experiment at SINBAD[2] [99, 100].

With the PolariX TDS, it is possible to arbitrarily adjust the polarization of the deflecting field. Thus, the direction in which the streaking of the TDS takes place can be altered at will. This unique feature enables experimental access to a number of bunch properties, such as the reconstruction of the three-dimensional charge distribution [101, 102] and slice emittance measurements carried out in both transverse planes (using the same deflecting structure) [103]. A characterization of the complete six-dimensional phase space can be achieved. It should be noted that these feats cannot be accomplished with a conventional LOLA-type TDS.

The FLASH facility contains a total of three PolariX structures. While the FLASH2 beamline features two structures, each measuring 0.96 m in length, the FLASHFORWARD beamline is equipped with only one PolariX TDS. In principle, the PolariX TDS also belongs to the category of disk-loaded structures; the iris radius is equal to 4 mm with a disk thickness of 2.6 mm. It should be noted that the deflecting structures at both beamlines share the same rf power source, which means that simultaneous operation of the PolariX structures at both beamlines is currently not possible. The rf pulse generated by a dedicated modulator and amplified by a klystron reaches an output power of 6 MW. At FLASH2, klystron and PolariX structures are connected by a waveguide of 5 m length. The expected deflecting voltage amounts to $\approx$ 34 MV. The maximum deflecting voltage at FLASHFORWARD is again slightly reduced due to waveguide losses and roughly $\approx$ 10 MV. As is the case with the conventional LOLA-type TDS, the reduced rf efficiency can be ignored due to the high input power, which again comes with the cost of a dedicated modulator, klystron and waveguide system.

4.2 MEASUREMENT PROCEDURE AND DATA ANALYSIS

This section includes a detailed description of the experimental procedure and the subsequent analysis of the bunch length measurements performed with the TDS at REGAE. The reliable execution of high-precision measurements places requirements on the beam properties of the accelerator. Therefore, some general considerations regarding the desired beam parameters and the operation of the machine to meet these demands will be discussed before addressing the core results of the bunch length measurements with the TDS.

2 Short and Innovative Bunches at DESY.

Upon passage through the TDS, the electron bunch receives an additional contribution to the transverse component of its momentum. At this specific beamline, the orientation of the TDS is such that the shearing is carried out in the vertical direction, which means that the TDS exerts a vertical kick on the particles in the bunch. Essentially, this vertical kick is translated into a vertical displacement of the electrons during the drift segment behind the structure, and the generated vertical offset depends on the longitudinal position of the particle within the bunch. To measure this, the electron beam needs to be imaged on a screen by use of an appropriate electron beam optics.

For experimental purposes, it is advantageous to manipulate the beam parameters in such a way that the effect the TDS has on the bunch is maximized. Hence the initial divergence of the bunch as it enters the structure should be kept minimal; beam size itself should be large [44]. With appropriate beam optics, the additional transverse momentum kick imparted by the TDS is converted to a certain finite (vertical) extent on a detector screen.

In summary, the ratio of the "stretched" vertical beam size, i.e. when the TDS is switched on, to the unperturbed beam size when the TDS is switched off should be at its maximum. One possible way of implementing this criterion is by use of a solenoid to focus the beam and thus tune the phase advance between the TDS and the detector to be equal to 90 degrees. As derived in section 2.3.2, this optimizes the achievable bunch length resolution of the measurement setup with the deflecting structure. In this case, the resolution can be written as [44]

$$R_z = \frac{\epsilon_y}{y_{0,\mathrm{RMS}} K}, \tag{4.15}$$

where ϵ_y denotes the vertical geometrical beam emittance, $y_{0,\mathrm{RMS}}$ denotes the vertical beam size in the TDS and the parameter K corresponds to the angle induced by the TDS per unit length as defined in section 2.3.1. Therefore, it is desirable to find machine settings which provide a beam with low transverse emittance and a relatively large beam size of approximately 0.5 mm [44].

4.2.1 Machine Setup Procedure

Some basic considerations regarding favorable machine settings and the procedure for setting up the machine for measurements will briefly be discussed.

The first step is the alignment of the UV laser on the cathode. For this purpose, the general approach is to apply a relatively low field gradient of 30 MV/m in the gun cavity. The reason for this is the fact that, as experience has shown, the beam can be imaged well on the nearest scintillator screen at this particular setting, as well as the absence of dark current at such low gradients. Moreover, all magnets are switched off to reduce any perturbations caused by the magnetic fields. The resulting electron beam can be imaged at the first diagnostic cross DDC1 (see section 3.1 for a description of the REGAE front-end). By turning the last motorized mirror of the UV laser section, the position of the laser beam on the cathode can be adjusted, which translates to a shift of the electron beam at DDC1. If the laser beam is aligned on the cathode, changing the phase or gradient of the gun cavity yields no significant change in electron beam position on the scintillator screen.

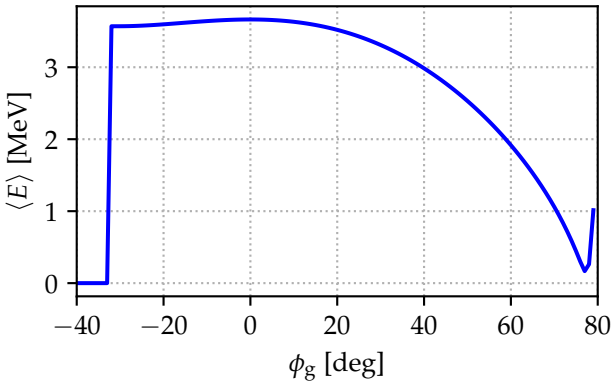

Figure 4.5: Kinetic energy gain $\langle E \rangle$ in the gun cavity in dependency of the gun phase ϕ_g for a peak gradient of $\mathcal{E}_g = 80\,\mathrm{MV/m}$ simulated with ASTRA. The net energy gain is maximized at $\phi_g = 0\,\mathrm{deg}$. The strong phase slippage in the gun cavity is responsible for the curious shape of the curve.

Next, a configuration of magnet settings must be determined to guide the beam through the accelerator beamline. The field gradient in the gun cavity was set to $\mathcal{E}_g = 80\,\mathrm{MV/m}$ to allow stable operation conditions. It should be noted that a calibration of the gun gradient has been carried out by performing an energy-phase-scan at the spectrometer prior to the experiments. Given the assumption that the rf system remains unchanged, the calibration is valid at all times and was therefore not repeated for each measurement. Similarly, a phase scan of the gun where the charge measured with a DaMon device was performed. Details on the calibration and the rf system can be found in [79].

Figure 4.5 shows an ASTRA simulation of the kinetic energy $\langle E \rangle$ of the electron beam gained in the gun cavity as a function of the gun phase ϕ_g for the standard operating gradient of $\mathcal{E}_g = 80\,\mathrm{MV/m}$. Due to the fact that the kinetic energy of the electrons upon release from the cathode material is nearly zero, the bunch experiences phase slippage with respect to the rf field. These phase slippage effects account for the particular profile of the curve. The phase value $\phi_g = 0$ denotes the phase where the energy gain reaches its maximum. During operation, the phase of maximum energy gain was determined using the dipole spectrometer. As long as the decisive laser and rf parameters do not change, this phase value remains constant.

Upon exiting the gun, the electron beam displays a large divergence. It is therefore necessary to operate the first solenoid almost at maximum field strength in order to "capture" the electrons and ensure propagation free of clipping on any of the elements located in the beamline[3]. In practice, a current of typically 8 A was sent through the magnet, which corresponds to a peak field of 170 mT. Solenoid 2/3 is required to reduce the divergence even further and can be used to set the size of the electron beam inside the TDS. The beam size can be measured with the FOS at the QSQ diagnostic cross. While the image on the scintillator technically reflects the bunch properties at QSQ and not directly inside the TDS, it must

3 A low field strength resulted in a larger beam size, which in turn often lead to clipping of the electron beam on the in-vacuum mirror of the cathode laser.

be mentioned that the TDS and QSQ are separated by a distance of only 73 mm (measured from the TDS exit flange to the QSQ scintillator screen). Hence the change in beam size between these two elements is negligible and therefore the beam size in the TDS is assumed to be equal to the beam size measured at QSQ in good approximation. The various dipole steerer magnets are used to guide the electron beam along the desired beam axis. For bunch length measurements, the electron beam should be aligned in such a way that it traverses the TDS along its central axis. A vertical shift from this axis in the TDS, for instance, leads to an alteration of the beam energy. Utilization of steerer pairs in front of the TDS enables the alignment of the electron beam so that no energy gain or loss is visible when the TDS is switched on, which means that the beam propagates through the deflecting structure without vertical offset from the axis.

In the beamline segment behind the deflecting cavity, deployment of the steerer magnets is helpful to center the beam on the detector screens. Furthermore, solenoid 6/7 is used to optimize the phase advance between TDS and detector. As explained above, the desired phase advance is equal to 90 deg.

Once the beam axis through the REGAE front-end has been defined and an according magnet configuration has been established, collimators can be driven into the beamline to reduce dark current. As described in section 3.1, the REGAE beamline is equipped with two collimators at DDC1 and DDC2. While the bunch length measurement itself can be carried out without reducing the dark current, the subsequent processing and evaluation of the images recorded with the detector is simplified greatly when the dark current has been eliminated or at least minimized as much as possible.

Lastly, some parameters can be fine-tuned to satisfy the requirements of the respective measurement. This may include, for example, the adjustment of the laser power with the attenuator setup in the UV segment of the cathode laser to obtain a desired charge and potentially reduce space charge effects, since it is much easier to set up the machine with higher charge and subsequent stronger signal on the scintillator screens at the diagnostic crosses, and the alignment of the electron beam through solenoid 6/7 to prevent the electron beam from vanishing off the edge of the scintillator screen due to a transverse kick received if not propagating along the magnetic axis of the solenoid.

An exemplary evolution of the transverse beam size along the beamline under the influence of the solenoids located in the REGAE front-end is shown in figure 4.6. Both horizontal and vertical beam sizes have been extracted from an ASTRA simulation of an electron bunch of $Q = 100\,\mathrm{fC}$ charge. The gun cavity and the two solenoids Sol 1 and Sol 2/3 are the only active elements in the simulation and have been marked gray and green, respectively. The deflecting structure has also been marked gray. The purpose of this simulation was to identify solenoid settings which provide an electron beam with desirable properties at the position of the TDS, i.e. a transverse beam size of approximately 0.5 mm and low transverse divergence during propagation through the deflecting structure [44]. As previously mentioned, the first solenoid is set to 8 A, which produces a maximum field of 170 mT. The abovementioned simulation has shown that solenoid 2/3 should yield a peak field of 48 mT to achieve a beam transport as plotted in figure 4.6.

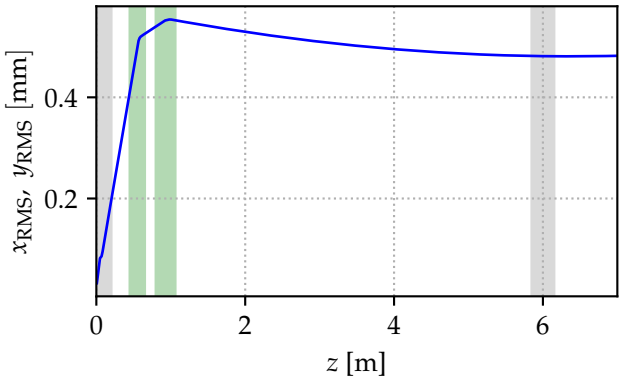

Figure 4.6: ASTRA simulation showing a preferable evolution of the transverse beam size (of a transverse symmetric electron bunch, i.e. $x_{RMS} = y_{RMS}$, containing a total charge of $Q = 100\,\text{fC}$) as a function of the longitudinal position z along the design trajectory. The gun cavity is marked gray and is located at the beginning of the beamline. The two solenoids Sol 1 and Sol 2/3 are marked green. While not activated in this simulation, the TDS located at $z = 6\,\text{m}$ is also marked gray.

These values obtained from the ASTRA simulation were used as starting points for the procedure of setting up the machine for various measurements. After adjusting the solenoids to their respective values and tuning the steerer magnets to roughly center the electron beam on the detector screens, the beam size was evaluated at different positions along the beamline, namely at LD1e, inside the target chamber using a FOS screen on the central hexapod, at QSQ and at the D2 detector system. It should be mentioned that an intricate analysis of the obtained detector images was not performed. Instead, the beam size was determined during machine operation with help of the REGAE camera tool[4] by taking a number of background images[5], subtracting these from the beam images and applying a simple relative intensity cut. This intensity cut merely sets all pixel values below a given percentage of the maximum pixel value to zero. A magnet configuration to achieve a desired beam transport was found by tuning the peak fields of the magnets in an iterative procedure. Solenoid 1 was indeed set to 170 mT, whereas the peak field of solenoid 2/3 was adapted to 51 mT. This value deviates only slightly from the simulated value. The final solenoid in the beamline was used to optimize the phase advance between TDS and detector by focusing the beam to a small spot.

Naturally, these magnet settings strongly depend on the rf parameters of the cavities. Measurements performed in context of the linearization strategy require a different configuration than a "standard" bunch length measurement where the gun cavity is operated at maximum energy gain. Nevertheless, the machine setup procedure remains more or less the same and the aforementioned solenoid values have proven to be extremely useful as a starting point, especially for setting up the front section of the beamline.

4 The REGAE camera tool is a Matlab-based tool created by Max Hachmann.
5 Typically, an average background array was calculated as the mean of ten recorded background images.

4.2.2 Image Processing

Essentially, measurements of beam properties can be equated with extracting relevant information from raw data of a detector device. In the case of the detectors installed at REGAE, where the data is in form of images recorded with a respective camera (as described towards the end of section 3.2.2), statements regarding the length of the electron bunch can be made by analyzing the streaked (and unstreaked) detector images. An appropriate image processing routine is therefore a crucial element in terms of determining the beam signal within an image. In order to develop such a routine, the properties of noise and background present on an image need to be described and understood.

As previously mentioned in section 3.2.2, the images are recorded with Andor EMCCD cameras installed at the dipole spectrometer and at the D2 detector setup. While there is intrinsic electric noise in every camera, the EMCCD cameras at REGAE feature several technical aspects which lead to an effective reduction of noise (see again section 3.2.2 and [79] for details). Moreover, shot to shot fluctuations in the images are clearly visible. These fluctuations are of statistical nature and manifest themselves in form of variations in the number of electrons registered by a certain pixel of the camera chip. This type of noise is referred to as shot noise.

In addition to this, a detector image contains not only a beam signal from electrons released due to the UV laser, but also displays a background structure as a result of unintentionally accelerated electrons from the cavity. As a result of the residual roughness of the surface on the inner walls of the cavity, the high rf field gradient gives rise to the emission of electrons. A portion of these electrons propagates through the accelerator beamline together with the electrons produced by the laser spot on the cathode and are commonly referred to as dark current.

Typically, the dark current overlaps with the beam signal at the detector. As long as the assumption that the center of mass of the dark current remains constant during experiments holds true, it is possible to eliminate the dark current on the detector images by simply subtracting background images, i.e. camera images where the photocathode laser has been blocked by a shutter, from the images containing the beam signal. However, the dark current itself is also dominated by shot noise. The subtraction of the background causes additional noise on the images. By taking several images to increase statistics, the noise can be reduced. The image processing routine must

1. remove the dark current background and
2. determine and isolate the beam signal from the remaining noise

in a reliable way.

The production of electrons via the UV laser on the cathode and via high field gradients at the inner walls of the cavity can be seen as independent random events. These processes follow a Poisson distribution

$$f_{\mathrm{P}}(k,\lambda) = \frac{\lambda^k}{k!}\exp(-\lambda), \tag{4.16}$$

where $k \in \mathbb{N}$ can be identified with the number of electrons registered by a pixel of a detector and λ denotes the expected value and the variance of the distribution.

The events on each pixel can be associated with a Poisson distribution. Excluding the small region containing the beam signal, subtracting a background array from a complete image is equivalent to the subtraction of two images based on a Poisson distribution. For each single pixel, the result of the subtraction follows the Skellam distribution

$$f_S(k, \lambda_1, \lambda_2) = \left(\frac{\lambda_1}{\lambda_2}\right)^{\frac{k}{2}} I_k(2\sqrt{\lambda_1\lambda_2}) \exp(-(\lambda_1 + \lambda_2)), \tag{4.17}$$

where λ_1, λ_2 are the expected values of the respective Poisson distributions and I_k denotes the modified Bessel function of the first kind [104]. In the case of the Skellam distribution, the expected value is equal to $\lambda_1 - \lambda_2$, whereas the variance is given by $\lambda_1 + \lambda_2$. Since the pixel values for a given pixel on both images originate from the same source, the assumption $\lambda_1 = \lambda_2 = \lambda$ should hold true. This implies that the resulting distribution is centered around zero, which will be verified shortly.

However, the incorporation of the Skellam distribution in a to the greatest possible extent automated image processing algorithm is suboptimal. The calculation of the parameters by means of a fit routine is significantly slower than for a normal distribution, which can be utilized substitutional for the Skellam distribution if the expected values are large enough: for $\lambda > 30$ the underlying Poisson distribution can be approximated by a normal distribution. For even higher values of λ, the degree of resemblance between the two distributions continuously increases. More specifically, the Poisson distribution displays strong asymmetry for small values of λ. It becomes more symmetric with increasing λ and can ultimately be approximated by a normal distribution f_N written as

$$f_P(k, \lambda) \approx f_N(k, \lambda) = \frac{1}{\sqrt{4\pi\lambda}} \exp\left(-\frac{(k-\lambda)^2}{4\lambda}\right), \tag{4.18}$$

where mean and variance are given by $\mu = 0$ and $\sigma^2 = 2\lambda$, respectively [105]. The assumption of high λ is typically fulfilled for the high pixel depths of the 14- and 16-bit images recorded with the Andor cameras. Ultimately, the subtraction of the background array yields a normally distributed noise array centered around $\mu \approx 0$ where a small image region contains the beam signal which accounts for exceptionally high pixel values.

It should be pointed out that this is only a valid approximation as long as the individual pixel values λ_k of all k pixels do not differ significantly from each other with exception of the beam signal, i.e. apart from the beam there should be no other structures visible on the image after background subtraction has been performed. As a result from shot noise of the dark current and a positional jitter of the dark current at REGAE, a residual structure is typically present in the background subtracted images. It has previously been empirically determined that a superposition of two normal distributions is well suited for the description of the background subtracted image [79].

The respective pixel intensity histogram of an image, after background subtraction has been carried out, is shown in figure 4.7. Both images have been recorded at the D2 detector setup. The data points are marked in black and a double Gaussian fit function is plotted in red. It can clearly be seen that the distribution

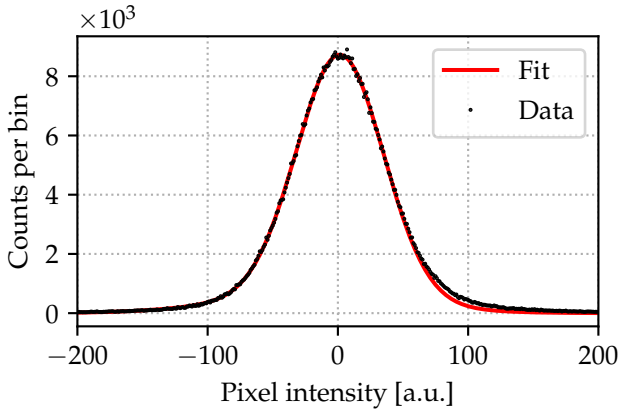

Figure 4.7: Pixel intensity histogram of a background subtracted image recorded at D2. The data points are shown marked black. A least squares fit using the superposition of two Gaussian functions has been applied to the noise distribution and the resulting function is shown in red. The distribution is centered around zero.

is indeed centered around zero, which confirms that the assumption $\lambda_1 = \lambda_2$ for (nearly) all pixels in two images "1" and "2" (full image and background) is justified. Upon further inspection it becomes apparent that the data differ slightly from the the fit function at higher pixel values. This difference is caused by the beam signal, which accounts for the asymmetry of the data. The noise distribution itself is assumed to be symmetric around zero. Only data points below the pixel intensity value of $\mu + \frac{\text{FWHM}}{2.35}$ were considered for the fit. The FWHM of the distribution was calculated as an estimate for the variance of the Gaussian function and then also used as the initial parameter for the fit.

Shot noise has been identified as the dominant noise source in the image data at REGAE. In order to reduce statistical uncertainties of beam signal and background, several images with and without beam, i.e. signal and background, are recorded. This allows for the calculation of the average of the images, which can then be used for further analysis. Naturally, this approach is only valid if the operating conditions of the accelerator remain sufficiently stable.

Despite the fact that this is generally the case at REGAE, a spatial jitter of the beam and also of the dark current can clearly be seen on all detector images. The reasons for this can be manifold. For instance, fluctuations in the electric currents circulating through the respective magnets can lead to differences in the generated magnetic field and therefore result in varying deflection of the beam. Another possible contribution regarding the beam signal is the positional jitter of the laser beam. While the installed stabilization setup does counter some unwanted effects such as temperature drifts, small jitters still remain. Instabilities in the rf system may also be responsible for the jitter of both beam and dark current. At the time of the measurements presented in this thesis, the desired variations of 0.01 % in amplitude and 0.01 deg in phase (as specified in section 3.1, see [52] for more details) could not be observed. The stability of the gun rf system is visualized in figure 4.8, where the deviation of the readback values from the setpoints of 80 MV/m amplitude and maximum energy gain phase are

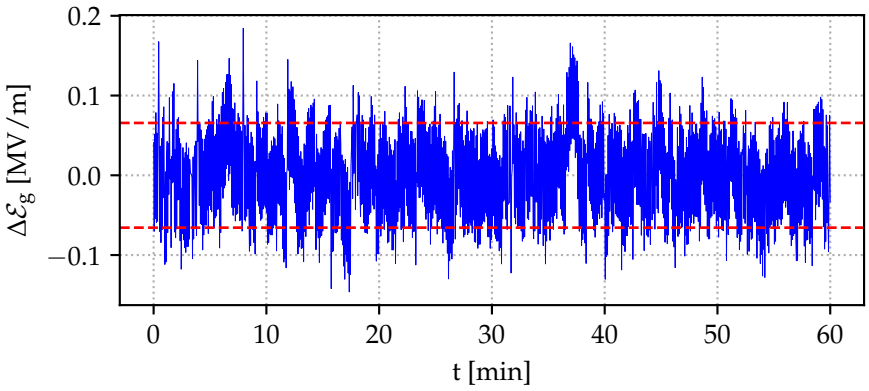

(a) Variation $\Delta\mathcal{E}_g$ of the gun gradient readback value around the setpoint of 80 MV/m accumulated over a time frame of one hour.

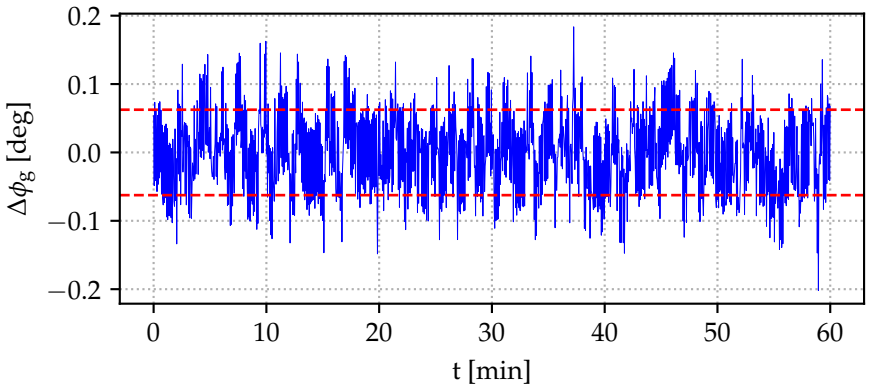

(b) Variation $\Delta\phi_g$ of the gun phase readback value around the initial setpoint accumulated over a time frame of one hour.

Figure 4.8: Stability of the gun gradient (4.8a) and phase (4.8b). The rf readback values were accumulated over the course of one hour. The dashed red lines indicate the respective RMS value.

shown over the course of one hour. The standard deviation of gun gradient and rf phase is equal to 0.07 MV/m (which corresponds to 0.08 % at a gradient setpoint of $\mathcal{E}_g = 80$ MV/m) and 0.06 deg, respectively. The buncher cavity was subject to larger fluctuations of 0.5 % in amplitude and 0.12 deg in phase. Investigations regarding the stability of the rf and laser systems at REGAE and subsequent improvements are a continuously ongoing process.

The positional jitter of the beam signal poses a problem if the RMS beam sizes are calculated from the averaged images where summation of the images has been applied. The variations on the two-dimensional image effectively lead to a "smearing out" of the beam, which falsely increases the calculated RMS values. This effect can be reduced, if not completely eliminated, by centering the image arrays to each other. A variety of methods exist to detect the effective offset between images. For various images analyzed and presented in the course of this thesis, the image alignment was performed via cross-correlation. Naturally, centering the images is not necessary when evaluating single-shot measurements.

Generally speaking, cross-correlation gives information on the similarity of two signal arrays plotted against the relative displacement between both arrays [106]. The functional dependency arises from "sliding" the second array over the first array, which is why cross-correlation is also referred to as sliding dot product. As long as the main difference between two arrays can be described purely by displacement, cross-correlation is well suited to detect the existing offset. This requires that there is

1. no rotation between the images and
2. no significant variation in brightness.

Since the beam intensity is affected by shot noise, the second constraint is only fulfilled to a certain extent. For large variations in intensity, a type of normalization can be applied to the images prior to calculating the cross-correlation. However, this was not necessary for the images obtained at REGAE.

For reasons of computational efficiency, the convolution of two images was calculated rather than the cross-correlation. The two quantities are closely related: cross-correlation is equivalent to convolution where the second image array has been mirrored. The underlying principle of the utilization of cross-correlation to detect the translation between two beam signal arrays can be illustrated with the following example (see figure 4.9): consider two artificial beam signals generated by a two-dimensional Gaussian distribution with a transverse beam size of $\sigma_x = \sigma_y = 3$ pixels, which is roughly in the order of magnitude of real beam sizes recorded at the REGAE detectors (for a focused beam; see the top left subplot in figure 4.9). The mean position of the second beam signal has been shifted by 10 pixels from the first beam signal in the horizontal direction. Taking the mean of both images (summation and division by number of images) yields a horizontal beam size of $x_{\mathrm{RMS}} = 5.83$ pixels, which clearly overestimates the actual beam size. To determine the offset between both images, the self-correlation, i.e. the cross-correlation of the first image with itself, is calculated (see figure 4.9; bottom right). In this case, the two-dimensional pixel coordinates where the cross-correlation reaches its maximum correspond to the center of the image, which is to be expected for two identical images. However, the maximum coordinates of the cross-correlation of the first image with the second image are slightly shifted with respect to the image center (see figure 4.9; top right). The difference between the maxima is equal to the offset between the two beam signals. Indeed, shifting the second image by the respective value yields the correct beam size $\sigma_x = 3.00$ pixels (see figure 4.9; bottom left).

Beam Intensity Cut

After formulation of an adequate theoretical description of noise and possible centering of the signal arrays, the isolation of the beam signal from the surrounding noise on the image still needs to be carried out. In previous measurements performed at REGAE, a distinct halo surrounding the beam has been observed at D2 at all times. Details on the halo are presented in [79], from which the general considerations are summarized below.

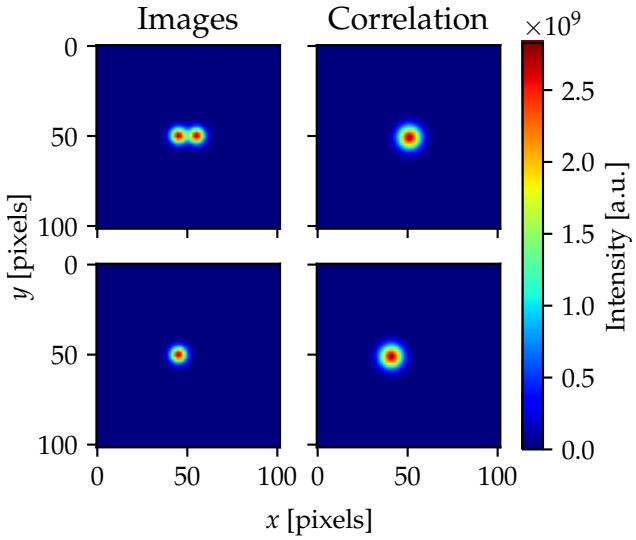

Figure 4.9: Illustration of array centering using cross-correlation. On the left side, uncentered (top) and centered (bottom) image arrays based on the artificial two-dimensional Gaussian distributions are shown; the top subplot shows the simple addition of two uncentered Gaussians. The right side shows the self-correlation (top) of the reference Gaussian and the cross-correlation (bottom) of both Gaussians. The clearly visible shift in the between the correlations is equal to the shift between the two input image arrays.

For the unstreaked and focused electron beam, signal and halo on the detector can be described by the superposition of two Gaussian functions. The fundamental idea behind the beam intensity cut procedure is to only take the first Gaussian function (with larger amplitude and smaller width), i.e. the beam signal, into account. The images in or at least near the focus of the beam are selected due to the high signal to noise ratio and good performance of the fit. Once the fit to the horizontal and vertical beam profile has been performed, the beam intensity I_{beam} can be calculated as the integral of the associated Gaussian function

$$I_{\text{beam}} = \int_{-\infty}^{\infty} A_1 \exp\left(-\frac{(x-\mu_1)^2}{2\sigma_1^2}\right) \mathrm{d}x, \tag{4.19}$$

where A_1 is the amplitude and μ_1 and σ_1^2 are the mean and variance of the distribution, respectively. The calculated intensity can then be implemented as a form of quantile I_{cut} in the respective pixel intensity histogram. All pixels with intensities smaller than I_{cut} are not considered to be part of the beam. This procedure originates from the work presented in [79].

The effect of the beam intensity cut method is presented in figure 4.10. A typical detector image of a focused beam recorded with the D2 detector setup was recreated as a superposition of two Gaussian functions for the beam signal and halo, respectively. The beam Gaussian was created with a standard deviation of $\sigma_x = \sigma_y = 10\,\text{pixels}$, whereas the halo Gaussian had a transverse beam size of $\sigma_x = \sigma_y = 50\,\text{pixels}$. Moreover, the amplitude of the beam Gaussian was set to be 100 times larger than the halo amplitude. This approximately corresponds to the halo (and beam) properties observed on real detector images at the D2

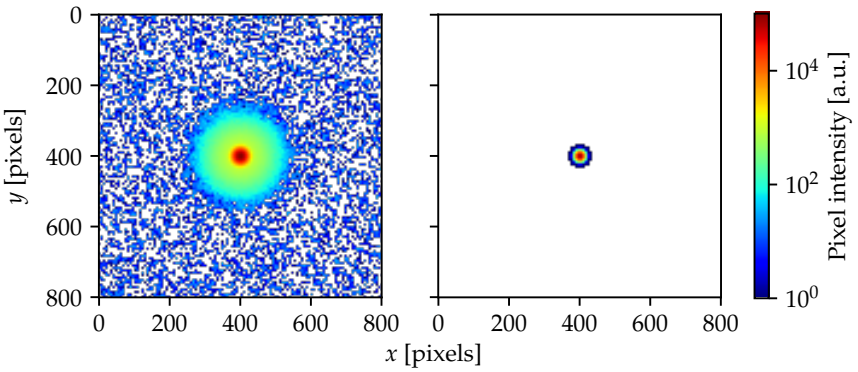

(a) Artificially generated detector image before (left) and after (right) application of the beam intensity cut routine.

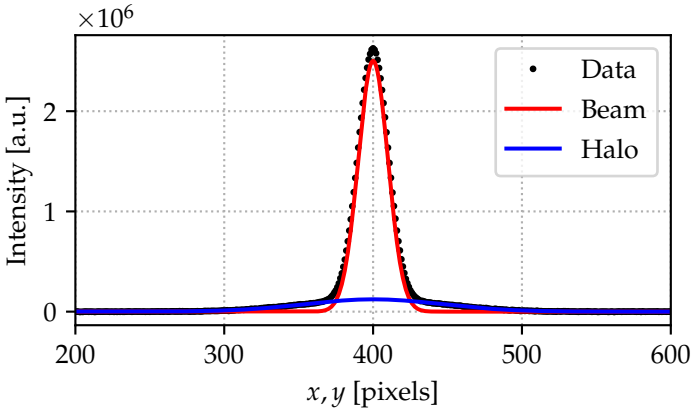

(b) Exemplary replication of the transverse profile of a Gaussian beam surrounded by a halo at D2.

Figure 4.10: Illustration of the beam intensity cut routine. Figure 4.10a shows synthetic detector images before (left) and after (right) image processing. The initial beam size was set to 10 pixels. The beam intensity cut reconstructs the RMS beam size with a percent-level precision. The discrepancy depends on the strength of the halo. Figure 4.10b shows the transverse profile of the unprocessed image. The Gaussian functions for the beam (red) and halo (blue) are labeled accordingly. The beam Gaussian was used to calculate the intensity cut value.

detector setup[6]. A noise array based on a normal distribution was also added to the image. The unprocessed image can be seen in figure 4.10a on the left. Without the implementation of any type of intensity cut procedure, the transverse beam size is equal to $x_{\mathrm{RMS}} = y_{\mathrm{RMS}} = 25.47$ pixels.

The transverse profile of the image is shown in figure 4.10b, where the two Gaussian fit functions for the beam, colored in red, and the halo, colored in blue, can also be seen. Next, the intensity of the beam was calculated by integrating the beam Gaussian function. In practice this was usually done for both vertical and horizontal coordinate, and the mean of the the two intensity values was used for further analysis. The beam intensity was then used to define an intensity cut value in the pixel intensity histogram. The intensity values of all pixels with fewer entries than the threshold were set to zero. This marks the last step in the image processing routine. The processed image is shown on the right side of figure 4.10. Based on a total of 1000 artificial beam samples of the type described above, input beam size and processed beam size deviate by $(4.54 \pm 0.10)\,\%$. While the reconstruction of the RMS value with the beam intensity cut is slightly erroneous, the deviations are reasonably small and the RMS values are certainly much closer to the initial beam size than the values calculated from the unprocessed image, which still contains the beam halo. The deviation written above is included in all calculated RMS beam sizes presented in the sections below where the beam intensity cut has been applied.

Naturally, the variance of the beam Gaussian may also be interpreted as beam size in the specific case where the beam profile can correctly be modeled by a Gaussian function. However, this circumstance is not always given for both axes of a detector image. For instance, an image containing a beam signal streaked along the vertical axis by the TDS may exhibit a Gaussian shape in the horizontal profile, but the vertical profile, i.e. the profile in streaking direction, will generally not be describable by a Gaussian function.

Additionally, it should be noted that the difference between initial and reconstructed beam size is affected by the amplitude of the halo. Observations during machine operations have lead to the assessment that the beam halo at the dipole spectrometer appears to be considerably weaker compared to the D2 detector setup. For smaller halo amplitudes (≈ 500 times smaller with respect to the beam amplitude), the reconstructed beam size rapidly converges towards the initial beam size, i.e. the deviations quickly tend towards values below 1 %.

Region Growing Algorithm

A drawback of the beam intensity cut developed in [79], as summarized in the section above, is the fact that the profile must be described by a function. However, this function is not necessarily known; and the simple case of an underlying Gaussian distribution is not always given. If the bunch distribution is not known and cannot be easily described by a (simple) analytical function, a different method of image analysis is required.

6 The beam halo at the dipole spectrometer setup appears to be considerably smaller; further investigations are required.

Essentially, the isolation of the beam signal from the rest of the image, containing dark current and camera noise, can be expressed as a form of image segmentation. Generally speaking, image segmentation can be defined as the process of splitting an image into subsets of pixels grouped together [107]. These subsets are commonly referred to as image objects. One of many existing image segmentation methods is region growing.

A form of region growing has previously been utilized in [108] and discussed in [54]. This region growing algorithm intrinsically confines the region of interest to an elliptic area in the image. As such, the algorithm provides good results only when the underlying beam distribution exhibits an elliptical shape on the detector image.

Due to the fact that the condition of elliptical shape does not apply to some of the streaked images recorded with the detectors at REGAE, a more generalized method of region growing was implemented [109]. A similar algorithm has been previously used in [92].

Any seeded region growing algorithm requires an initial pixel as a starting point from which the object is identified; this pixel is commonly referred to as seed pixel [109]. In the case of the electron beam images recorded with the REGAE detectors, it is justified to assume that the pixel with maximum intensity belongs to the beam. Therefore, this pixel can be selected as a reliable seed pixel. In the next step, the eight neighboring pixels are determined. It should be noted that it is also possible to disregard the diagonal neighbors, i.e. to only consider the four nearest neighbors surrounding the seed pixel. For each neighbor the algorithm determines whether or not the current pixel should be added to the region of interest. This decision is based on a predefined threshold. If the restrictive condition is fulfilled, the pixel is added to the region and also added to a list of pixels to be processed, for which the procedure of determining the neighboring pixels is repeated. To optimize the efficiency, respective pixels are only processed once (at maximum).

The intensity threshold itself is based on the noise distribution of the background subtracted image. From the corresponding pixel intensity histogram (see figure 4.7 for an example), both mean μ and variance σ^2 are calculated. As deduced in an earlier part of this section, the noise distribution resembles a peaked Gaussian function and is approximately centered around zero. The threshold[7] was chosen to be $\mu + 5\sigma$. In the end, all pixel intensities outside of the region of interest are set to zero.

In cases where the streaked beam displays a large bunch length or energy spread and is observed at the dipole spectrometer, it covers a comparatively large portion of the camera image. This causes a rather long computation time for the region growing algorithm. To mitigate this effect to a reasonable extent, it is possible to apply binning to the images before applying the region growing algorithm. In image processing, binning is defined as the combination of a defined pixel subset into one single pixel. If the pixel subset is chosen to be of quadratic shape consisting of $N \times N$ pixels, a total of N^2 pixels are summarized in one "large" pixel. Thus the number of pixels in the image can be greatly reduced, which in turn speeds up the analysis procedure. However, large values of N

7 In [92], the threshold was set to 3σ.

can potentially result in a significant loss of information. Considering the two aforementioned effects, a pixel length was typically chosen to be in the interval $N \in [1,4]$ when implemented in the image analysis.

4.3 EXPERIMENTAL RESULTS

After successful adjustment of the machine settings following the procedure described in section 4.2.1, bunch length measurements with the TDS can be carried out. With the image data obtained with the REGAE TDS, which streaks the beam in the vertical direction, the bunch length can be reconstructed according to equation 2.69. This requires knowledge of the vertical beam size at the detector with and without the activated TDS. Moreover, the shear parameter S as defined in section 2.3.1 needs to be determined in order to calculate the bunch length from the measured beam sizes.

4.3.1 Transverse Emittance Measurement

At REGAE, the transverse beam emittance can be reconstructed by means of a solenoid scan [57]. Figure 4.11 shows the evolution of the transverse beam size x_{RMS} and y_{RMS} measured at the D2 detector as a function of the solenoid current, i.e. the focusing strength of solenoid 6/7. The beam intensity cut has been applied. The emittance can be reconstructed from the coefficients of a fit to the data. The fit is based on the envelope equation

$$y_{\mathrm{RMS}} = \begin{pmatrix} \mathcal{M}_{11}^2 \\ 2\mathcal{M}_{11}\mathcal{M}_{12} \\ \mathcal{M}_{12}^2 \end{pmatrix}^{\mathrm{T}} \cdot \begin{pmatrix} c_1 \\ c_2 \\ c_3 \end{pmatrix}, \tag{4.20}$$

where $\mathcal{M}$ is the transfer matrix from the solenoid to the D2 detector setup and the vector components c_n are given by

$$\begin{aligned} c_1 &= y_{0,\mathrm{RMS}}^2 \\ c_2 &= y_{0,\mathrm{RMS}} \cdot y'_{0,\mathrm{RMS}} \\ c_3 &= \frac{\epsilon_y^2}{y_{0,\mathrm{RMS}}^2} + (y'_{0,\mathrm{RMS}})^2 \end{aligned} \tag{4.21}$$

where $y_{0,\mathrm{RMS}}$ and $y'_{0,\mathrm{RMS}}$ denote the RMS beam size and envelope slope at the entrance of the solenoid [54]. Details on the fit procedure have been previously studied and analyzed at REGAE and are elaborated on in [54, 57, 79].

From the data presented in figure 4.11, the normalized horizontal and vertical emittance was calculated to be $\epsilon_{\mathrm{n},x} = (94 \pm 11)\,\mathrm{nm}$ and $\epsilon_{\mathrm{n},y} = (97 \pm 6)\,\mathrm{nm}$. The transverse beam size at the position of the solenoid can also be deduced from the fit parameters and is equal to $x_{0,\mathrm{RMS}} = (0.550 \pm 0.005)\,\mathrm{mm}$ and $y_{0,\mathrm{RMS}} = (0.463 \pm 0.002)\,\mathrm{mm}$, respectively. The fit routine and emittance calculation were carried out by Max Hachmann.

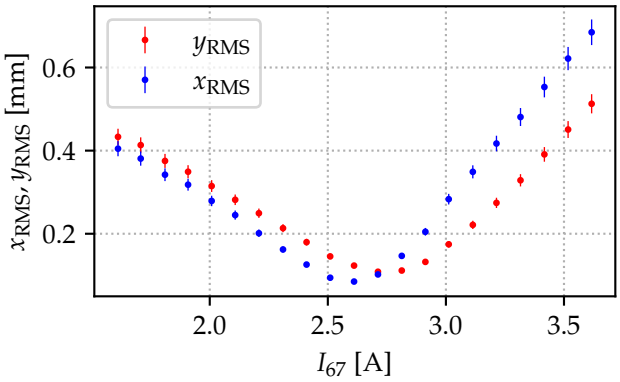

Figure 4.11: Vertical (red) and horizontal (blue) RMS beam size (x_{RMS} and y_{RMS}) as a function of the solenoid current I_{67}. The transverse emittance can be reconstructed from the functional dependency between focusing strength of the solenoid and beam size measured at D2.

4.3.2 TDS Calibration

Due to the fact that precise knowledge of the optical functions inside the TDS required to calculate the shear parameter using equation 2.68 is generally not at hand, a different approach is commonly used. The shear parameter is determined experimentally by performing a phase scan of the TDS, for which the procedure is outlined below.

After finding a suitable magnet lattice for the TDS measurements, the dipole magnet was activated to visualize the beam on the spectrometer. Next, the TDS was switched on. The TDS was aligned in such a way that no net energy gain was inflicted by the structure. In practice this was verified by recording the pixel position on the energy axis of the spectrometer camera image without the TDS, then activating the TDS and adjusting the vertical position with one of the steerer magnets installed in front of the TDS until the original pixel position was re-established. The energy of the beam was measured while the beam was on the spectrometer screen. Furthermore, DaMon1 and DaMon2 served as measurement devices for the bunch charge. In order to negate energy related jitter and any other potential perturbations arising from the magnetic field of the dipole spectrometer, the beam was then directed towards the D2 detector setup by deactivating the dipole.

In general, the TDS was operated in a mode where the rf phase was adjusted to a value for which the center of the electron bunch experiences no deflection from the structure and therefore propagates through the TDS along a straight line. This principle is visualized with ASTRA simulations shown in figure 4.12, where a calculated field map of the TDS was implemented[8]. The vertical mean beam offset with respect to the reference orbit is shown as a function of the TDS rf phase. The full range phase scan with $\varphi \in [0, 2\pi]$ can be seen in figure 4.12a. A close-up view of the range around the zero-crossing phase is shown in figure 4.12b. The linearity visible in this plot is of crucial importance for the calibration scan to determine the shear parameter. It should be noted that in principle two

8 The field map was provided by courtesy of K. Flöttmann and V. Paramonov.

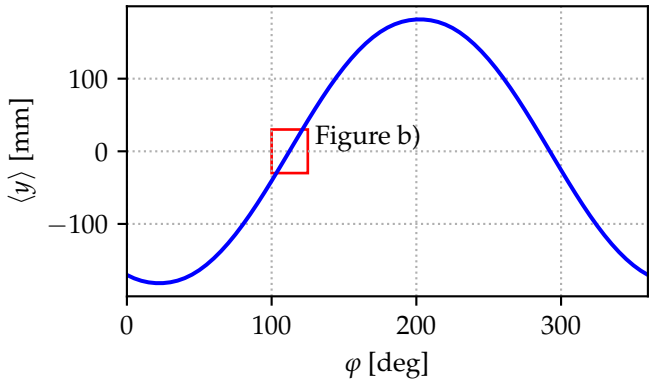

(a) Phase scan of the TDS simulated with ASTRA. The mean beam position $\langle y \rangle$ behind the structure is shown as a function of the TDS phase φ. There are two phase setpoints where the beam receives no transverse offset upon passage through the structure.

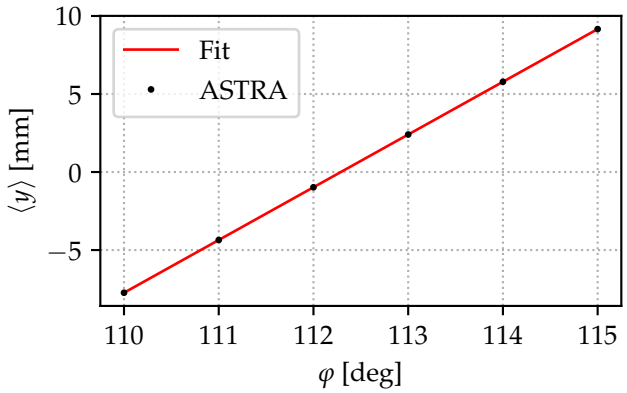

(b) Linear regime of the TDS phase scan simulated with ASTRA. The linearity is clearly visible.

Figure 4.12: Mean vertical beam offset $\langle y \rangle$ as a function of the rf phase φ of the TDS simulated with ASTRA. Figure 4.12a shows the full range phase scan, while figure 4.12b shows only the linear regime around the zero-crossing, which is of special importance in context of the calibration procedure of the TDS.

zero-crossing phases exist, which can clearly be seen in the full range phase scan. Operation at either of these phases yields identical results regarding the measured bunch length; the only difference is the sign of the shear parameter obtained experimentally through the calibration scan. The reconstructed bunch length is independent of the sign of the shear parameter.

From the calibration scan performed in ASTRA, the theoretical shear parameter can be determined from the linear fit to the data. This yields a shear parameter of $S_{\text{sim}} = 12.22$ for a deflecting voltage of 190 kV and an optimized phase advance of $\Delta\psi_y = \frac{\pi}{2}$. In a real cavity, the shear parameter will most likely be reduced slightly due to misalignment, power losses, field imperfections and various other deficits such as suboptimal phase advance adjustment. Nevertheless, a shear parameter of about 10 should be feasible.

At this point, it should be noted that the streaking direction does not necessarily correspond to an axis defined by the pixelated camera image.

Generally speaking, the transition from the camera coordinate system to the coordinate system defined by the TDS is given by a basis transformation. The pixel coordinates of the camera image form a restricted vector space $V_{\mathcal{B}}$, where $\mathcal{B}$ indicates the canonical basis of the camera image corresponding to the horizontal and vertical axes of the image. The restriction is given by the fact that the pixel vector space does not span over $\mathbb{R}$, but rather over $\mathbb{Z}$. The TDS coordinate system is characterized by a different basis $\mathcal{B}'$. The transformation matrix $\mathcal{M}_{\mathcal{B}\to\mathcal{B}'}$ can be computed if the basis vectors of $\mathcal{B}'$ are known. For a set of basis vectors $\mathcal{B}' = (\vec{b}'_1, \ldots, \vec{b}'_n)$ of an n-dimensional vector space V, the basis vectors $\mathcal{B} = (\vec{b}_1, \ldots, \vec{b}_n)$ can be expressed as a linear combination

$$\vec{b}_m = \sum_{k=1}^{n} c_{km} \vec{b}'_k \tag{4.22}$$

with $m \in [1, n]$. The coefficients c_{km} are summarized in the transformation matrix $\mathcal{M}_{\mathcal{B}\to\mathcal{B}'}$. Since the vector space is in fact equal to the coordinate space, albeit with the imposed restriction, the basis vectors can be written as column vectors. These vectors can be combined in respective matrices $\mathcal{M}_{\mathcal{B}}$ and $\mathcal{M}_{\mathcal{B}'}$. In this case, the transformation matrix is simply given by

$$\mathcal{M}_{\mathcal{B}\to\mathcal{B}'} = \mathcal{M}_{\mathcal{B}'}^{-1} \cdot \mathcal{M}_{\mathcal{B}}. \tag{4.23}$$

The expression simplifies if $\mathcal{B}$ is the canonical basis, in which case $\mathcal{M}_{\mathcal{B}\to\mathcal{B}'} = \mathcal{M}_{\mathcal{B}'}^{-1}$ holds true.

In order to determine the shear parameter and the tilt between the streaking direction and the vertical axis of the camera image, a TDS phase scan was performed in the linear regime characterized in figure 4.12b. Ideally, the beam centroid only moves along the vertical axis of the camera. In reality, a small degree of horizontal movement was also observed.

This is depicted in figure 4.13, which shows the evolution of the beam centroid for a variety of TDS phase settings in the linear regime around the zero-crossing phase. A total of 20 beam and background images were recorded with the D2 detector at each setpoint of the TDS rf phase. Subtraction of the averaged background was carried out for each beam image to eliminate the image structures resulting from dark current. However, the array centering procedure was not executed. The reason for this is the fact that one of the images must be selected as a reference array to which all other images are centered. The positional jitter visible on the D2 camera image arising from the TDS can potentially lead to a "bad" choice of reference image, which would then affect the calculated beam centroid position and thus impact the parameters of the fit function, leading to a falsification of both $\mathcal{M}_{\mathcal{B}\to\mathcal{B}'}$ and the shear parameter. To overcome this problem, the beam position was determined for each beam signal image individually. The beam positions are plotted with respect to the beam centroid of the unstreaked beam corresponding to $\langle y \rangle = \langle x \rangle = 0$.

For each rf phase setpoint, the mean beam position and variance were calculated from the individual beam position values obtained from each beam signal image. A linear fit has been applied to the data and is plotted as a red line in figure

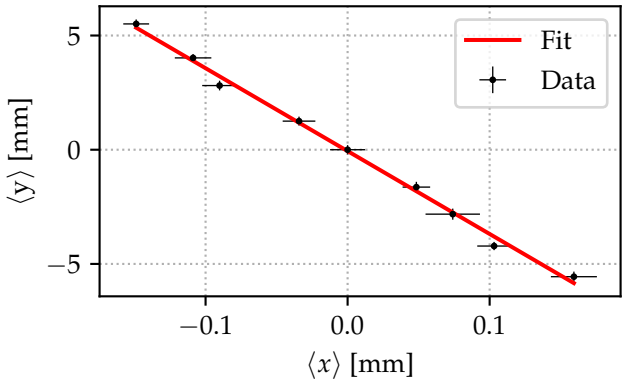

Figure 4.13: Measured position of the beam centroid on the D2 detector screen for a variety of TDS phase values. Each data point (black) represents a different phase setting, for which the mean beam position ($\langle x \rangle, \langle y \rangle$) is plotted.

4.13. The measurement results imply that the streaking axis is slightly tilted with respect to the vertical camera axis, since the beam centroid also performs a small degree of movement along the horizontal camera axis. Based on the slope of the linear fit to the measurement data, the angle between the streaking axis and the axis of the camera image can be calculated. The resulting angle is on the order of 10 mrad. From this dataset, the transformation $\mathcal{M}_{\mathcal{B}\to\mathcal{B}'}$ can be obtained. The image arrays can be transformed using a spline interpolation[9], after which the statistical moments of the distribution on the image can be calculated along the vertical axis of the resulting image array. It should be noted, however, that the effect of the transformation is usually significantly smaller than shot-to-shot uncertainties of the measurement data. Nevertheless, a respective correction has been applied to each image recorded with the TDS at the D2 detector.

In order to reconstruct the bunch length from the obtained image data, a calibration of the TDS needs to performed. Essentially, the calibration of the TDS involves the determination of the shear parameter S. As explained in section 2.3.2, the shear parameter is experimentally accessible by making use of the fact that the mean beam position in streaking direction depends on the rf phase at which the deflecting structure is operated. This is a direct consequence of the fact that a TDS is designed in such a way that the (vertical) position of a particle downstream of the structure is connected to its longitudinal position upon passage through the TDS.

The experimental data obtained from performing the calibration scan of the deflecting structure installed at REGAE is summarized in figure 4.14. The plot shows the mean position $\langle y \rangle$ of the electron beam in streaking direction for a variety of setpoints of the TDS rf phase φ. The data points essentially correspond to the dataset presented in figure 4.13 and are marked black in the plot. The electron beam had a mean kinetic energy equal to $\langle E \rangle = 3.667\,\text{MeV}$ and contained a charge of $Q = (105.2 \pm 0.8)\,\text{fC}$ per bunch. A linear fit, marked by the red line,

9 As per the default setting of the respective Scipy python module used for the rotation, a spline interpolation of the third order was generally used [110].

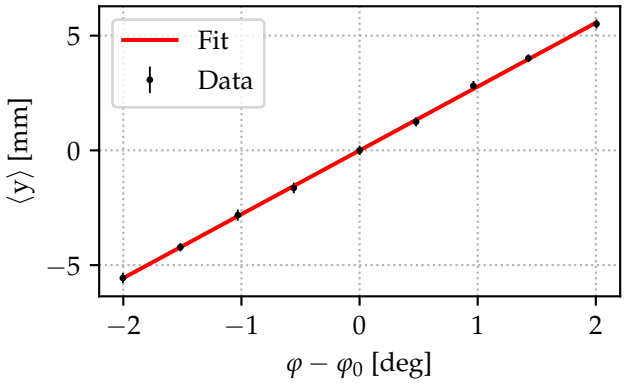

Figure 4.14: Linear fit (red) to the data (black) from the calibration scan. The mean vertical beam position $\langle y \rangle$ at the D2 detector setup is shown as a function of the TDS phase φ with respect to the zero-crossing phase φ_0.

has been applied to the data, from which the shear parameter can be reconstructed. It can clearly be seen that the data are well described by a linear function.

As derived in section 2.3.2, the vertical mean beam position $\langle y_\mathrm{d} \rangle$ measured with the detector and the rf phase φ of the deflecting structure are linked by a linear relation of the form $\langle y_\mathrm{d} \rangle = a\varphi + b$ with $a, b \in \mathbb{R}$. The shear parameter S of the TDS can be calculated from the slope of the linear fit according to equation 2.74. The slope of the fit depicted in figure 4.14 is equal to $a = (76.77 \pm 1.42)\,\frac{\mathrm{pixels}}{\mathrm{deg}}$. Plugging in the calibration of the screen at the D2 detector setup, where $1\,\mathrm{pixel} = 36.40\,\mu\mathrm{m}$, yields $a = (2.79 \pm 0.05)\,\frac{\mathrm{mm}}{\mathrm{deg}}$. The resulting shear parameter of the TDS for this machine setting for $\langle E \rangle = 3.667\,\mathrm{MeV}$ is equal to $S = 10.14 \pm 0.19$.

It should be noted that the procedure of determining the shear parameter from a linear fit only works as long as the mean vertical beam offset measured on the detector and the the rf phase of the TDS exhibit a linear correlation. Essentially, this means that the phase interval in which the calibration scan is performed should be confined to a small range around the zero-crossing phase where the vertical deflection is equal to zero. Experiences gathered during machine operation with the TDS have shown that a calibration scan where the TDS phase is varied in 0.5 deg steps within an interval $[\varphi_0 - \Delta\varphi, \varphi_0 + \Delta\varphi]$ around the zero-crossing phase φ_0 with $\Delta\varphi = 2\,\mathrm{deg}$ is feasible in most cases. The data of the calibration scan shown in figure 4.14 exemplifies this.

4.3.3 Bunch Length Measurement

In the previous section, the procedure for experimentally determining the shear parameter was described and the obtained results were presented. The calibration of the TDS, i.e. the shear parameter, has been measured and is equal to $S = 10.14 \pm 0.19$.

The bunch length can be reconstructed with the help of equation 2.3.2. This is possible because all required input quantities are known: the shear parameter has been calculated from the data obtained during the calibration scan and the beam sizes y_RMS and $y_\mathrm{RMS,off}$ have been measured with the EMCCD camera installed at

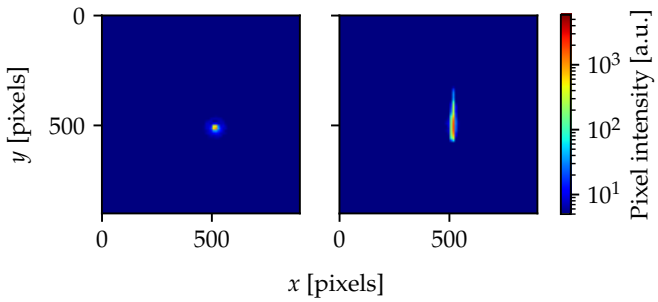

Figure 4.15: Camera images of the unstreaked (left) and streaked (right) electron beam recorded at the D2 detector setup. The shearing effect of the TDS along the vertical direction is clearly visible.

the D2 detector setup. Exemplary images showing the streaked and unstreaked electron beam are shown in figure 4.15. The effect of the TDS, which shears the bunch along the vertical axis, can clearly be distinguished upon comparison to the unstreaked image.

A total of 20 beam and background images were used for the reconstruction of the bunch length. After background subtraction, the unstreaked images were utilized as a basis for the beam intensity cut procedure, since the beam profile in streaking direction of the streaked images did not display a Gaussian shape. From each beam signal image, the beam intensity was calculated from the underlying Gaussian function. The beam intensity for each shot can be seen in figure 4.16. The error bars arise from the fact that each beam intensity value was calculated as the mean based on the fit functions to the beam profile in both horizontal and vertical direction. Taking only the intensity values depicted in figure 4.16 into account, the beam intensity exhibits a relative fluctuation of 1.35 % around the mean. This is on the same order of magnitude as the relative fluctuation of the bunch charge measured with DaMon1, which is equal to 1.13 %. Since these fluctuations are only on the level of 1 %, the beam intensity remains sufficiently constant on a shot-to-shot level. This confirms the applicability of the image processing methods used in this thesis.

The results of the bunch length measurements are summarized in figure 4.17. The reconstructed electron bunch length is shown for a total of 20 shots. The images were recorded with the camera installed at the D2 detector setup. The weighted mean bunch length is equal to $\bar{\xi}_{\mathrm{RMS}} = (454.06 \pm 9.57)$ fs for a bunch charge of approximately 100 fC, i.e. $\bar{\zeta}_{\mathrm{RMS}} = (136.22 \pm 2.87)$ µm, where the respective uncertainties have been used as weights. A summary of the main beam properties recorded in the course of the entire TDS measurement procedure is given in table 4.3.

With knowledge of the shear parameter S and the unstreaked beam size $y_{\mathrm{RMS,off}}$ at the position of the detector, the longitudinal resolution R_z of the TDS can be calculated according to equation 2.70. Plugging in the respective values yields a measured resolution of $R_z/c = (33.45 \pm 0.14)$ fs.

The validity of this result can be confirmed via comparison to an ASTRA simulation of the REGAE beamline. A required input parameter for the ASTRA

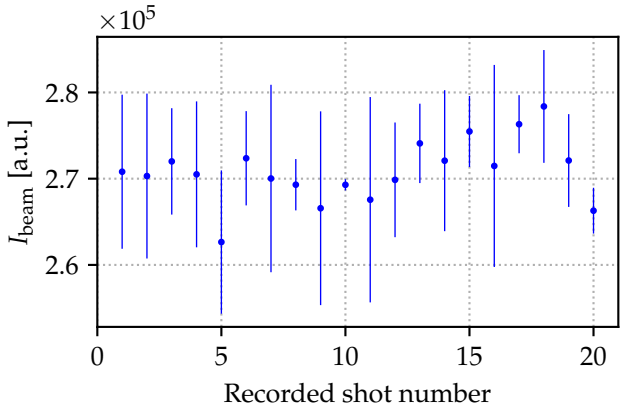

Figure 4.16: Shot-to-shot beam intensity I_{beam} calculated from the Gaussian fit during the beam intensity cut procedure.

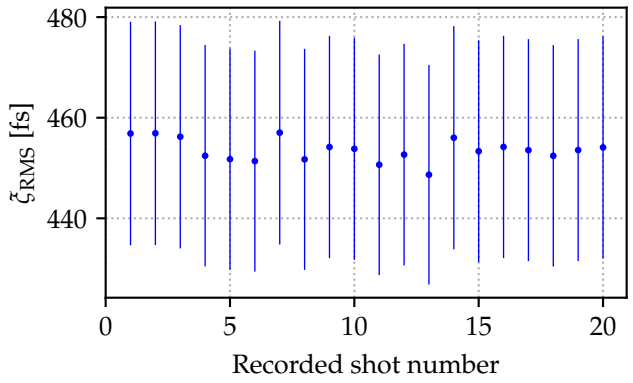

Figure 4.17: Electron bunch length ζ_{RMS} measured with the TDS for 20 shots. The camera images were recorded with the D2 detector and the beam intensity cut procedure has been applied.

Beam property	Measured value
$\langle E \rangle$ [MeV]	3.6668 ± 0.0004
Q [fC]	105.9 ± 1.2
ζ_{RMS} [fs]	454.06 ± 9.57
$\epsilon_{\text{n},x}$ [nm]	94 ± 11
$\epsilon_{\text{n},y}$ [nm]	97 ± 6

Table 4.3: Overview of beam properties measured in the course of the TDS bunch length measurements.

simulation is the electron emission time, i.e. the time interval during which electrons are emitted by the UV laser from the cathode. This corresponds to the pulse duration of the laser pulse. A measurement of the pulse length in the UV segment of the photocathode laser was carried out with the help of the DESY FS-LA group. An autocorrelator (see [111] and the references therein for a thorough description of pulse length measurements via the autocorrelation techniques) was temporarily placed on a board next to the laser table beside the cathode. In addition to this, a mirror was installed to couple out the laser beam and deflect it towards the autocorrelator. The operation of the autocorrelator and the subsequent measurements were performed with courtesy of the DESY FS-LA Laser Operation group.

Three sets of data were taken with the autocorrelator. The measurements are displayed in figure 4.18. It is possible to derive the intensity width, i.e. the pulse duration, from the intensity autocorrelation width. However, this is only feasible if the shape of the laser pulse is known. For further considerations, a Gaussian laser pulse is assumed. In this case, the deconvolution factor between the intensity autocorrelation width σ_{IA} and the intensity width $\sigma_{z,\mathrm{L}}$ of the laser pulse is equal to $\sqrt{2}$, i.e.

$$\sigma_{z,\mathrm{L}} = \frac{\sigma_{\mathrm{IA}}}{\sqrt{2}}. \tag{4.24}$$

Application of a Gaussian fit to the intensity autocorrelation profiles and averaging over the three datasets yields a laser pulse length of $\sigma_{z,\mathrm{L}} = (370.28 \pm 17.90)$ fs.

With the help of ASTRA, the evolution of the bunch length along the beamline can be simulated. The laser pulse length obtained from the autocorrelation measurements is plugged into the initial particle distribution of the simulation. This yields a simulated bunch length of $\xi_{\mathrm{o,RMS}} = (436.06 \pm 8.79)$ fs for $Q = 100$ fC at the position of the TDS if the TDS itself is not included in the simulation. However, space charge and higher order effects arising from the TDS must also be considered for the bunch length reconstruction. As discussed in section 4.1, the internal longitudinal motion of electrons in the bunch must be taken into account at energies in the range of a few MeV, which leads to an induced bunch length and transverse defocusing upon propagation through the TDS. The reconstruction of the bunch length according to equation 2.69 implicitly assumes that a deconvolution of the vertical beam size contribution from the bunch length (with respect to the total streaked beam signal) can be performed by utilizing $y_{\mathrm{RMS,off}}$, which is measured when the TDS is deactivated. From a mathematical point of view, the unstreaked beam signal acts as a point spread function with which the longitudinal profile is convolved in the streaked beam signal. In other words, $y_{\mathrm{RMS,off}}$ is assumed to be equal to the vertical beam size contribution of the streaked signal. Since the TDS causes transverse defocusing, this assumption is strictly speaking not fulfilled [44].

Simulations with ASTRA indicate that the induced bunch length contribution is well below 10 fs, which is in good agreement with the analytical prediction formulated in equation 4.7. This contribution can be neglected in the quadratic addition with the unperturbed bunch length $\xi_{0,\mathrm{RMS}}$ (see again equation 4.7). However, transverse defocusing caused by the TDS may increase the reconstructed bunch length. Plugging in the respective conditions and parameters

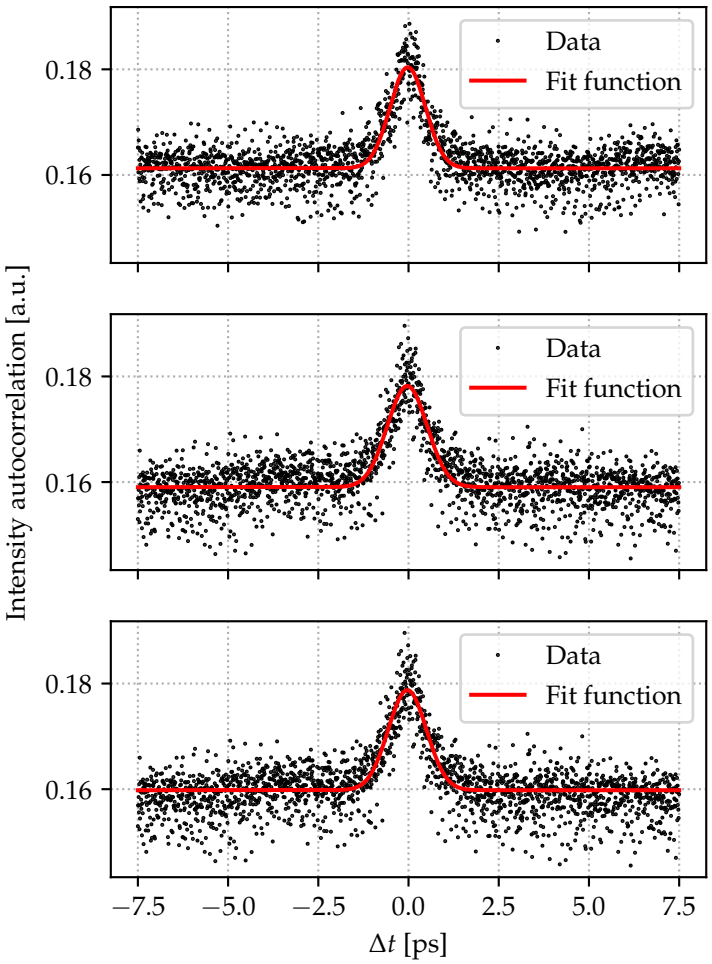

Figure 4.18: Measured pulse length in the UV section of the photocathode laser. The pulse length can be derived from the distribution of the intensity autocorrelation as a function of the delay Δt. The measurements were carried out with the assistance of the DESY FS-LA group.

of the measurement procedure in an ASTRA simulation, effectively performing a synthetic "measurement" in ASTRA, yields a reconstructed bunch length of $\xi_{\mathrm{RMS,sim}} = (437.87 \pm 8.83)\,\mathrm{fs}$. Thus, transverse defocusing leads to a increase of only about 1 fs in the reconstructed bunch length. Both transverse defocusing and induced bunch length are kept small as a result of the comparatively short length of the structure ($L_{\mathrm{TDS}} = 270\,\mathrm{mm}$). By operating the beamline at the design gun gradient $\mathcal{E}_{\mathrm{g}} = 100\,\mathrm{MV/m}$, thereby increasing the beam energy to $\langle E \rangle = 5\,\mathrm{MeV}$, these effects could be suppressed even further due to the $1/\gamma^2$ scaling. In addition, it is noted in [44] that a compensation of the transverse defocusing may be possible with appropriate beam optics. Studies regarding this aspect were not further explored in the scope of this thesis.

Comparison of synthetically "measured" bunch length $\xi_{\mathrm{RMS,sim}} = (437.87 \pm 8.83)\,\mathrm{fs}$ and measured bunch length $\bar{\xi}_{\mathrm{RMS}} = (454.06 \pm 9.57)\,\mathrm{fs}$ leads to the conclusion that, within the scope of measuring accuracy, the experimentally reconstructed bunch length is in outstanding agreement with the simulation results.

4.3.4 Ballistic bunching

As outlined in section 2.2.1 on the fundamentals of the ballistic bunching mechanism, a compression of the electron bunch length can be achieved by operating the buncher cavity at the zero-crossing phase, which is defined here as the phase value $\phi_{\mathrm{b}} = -90\,\mathrm{deg}$ where the bunch does not experience any gain in mean energy. The buncher gradient can be tuned in a way to shift the position of the longitudinal focus into the center of the TDS.

The principle of the ballistic bunching mechanism is illustrated in figure 4.19, based on a simulation with ASTRA where the buncher phase has been set to $\phi_{\mathrm{b}} = -90\,\mathrm{deg}$ and the buncher gradient was adjusted to $\mathcal{E}_{\mathrm{b}} = 8.5\,\mathrm{MV/m}$, which places the longitudinal focus at the position of TDS in the REGAE beamline. The gun gradient was set to $\mathcal{E}_{\mathrm{g}} = 80\,\mathrm{MV/m}$. In addition to this, the typical REGAE front-end magnet configuration regarding solenoid 1 and solenoid 2/3 (see section 4.2.1 for details on the general machine setup procedure) has been included in the simulation. For visualization purposes, space charge effects were not incorporated.

Figure 4.19a shows the evolution of the bunch length throughout the REGAE beamline. The positions of the cavities are marked in gray. After the buncher cavity, the bunch length decreases until the longitudinal focus is reached at $z = 6\,\mathrm{m}$. The position of the focus coincides with the center position of the TDS in the beamline. This enables the measurement of the bunch length in the focus. The TDS itself was not activated in this simulation. Moreover, the longitudinal phase space at selected positions in the beamline is depicted in figure 4.19b. Behind the gun cavity at $z = 1\,\mathrm{m}$, the particle distribution resembles a horizontal line, which implies a relatively small energy spread but also a large bunch length. The buncher cavity imprints a negative energy correlation onto the electron bunch, which can be seen in the particle distribution in the longitudinal phase space at $z = 4\,\mathrm{m}$. At the position of the longitudinal focus at $z = 6\,\mathrm{m}$, the phase space distribution is close to a vertical line. In the beamline section behind the focus, the bunch length increases again.

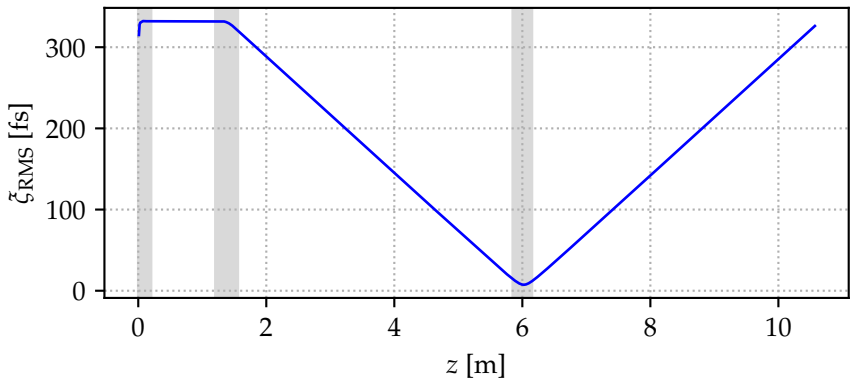

(a) Evolution of the RMS bunch length ζ_{RMS} throughout the beamline. The gray lines mark the positions of the gun cavity in the front, the buncher cavity at approximately $z = 1.3\,\mathrm{m}$ and the TDS at $z = 6\,\mathrm{m}$.

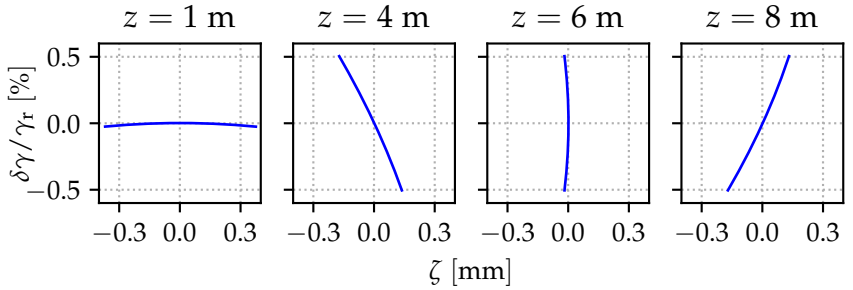

(b) Visualization of the longitudinal phase space at different positions in the beamline. A negative energy correlation is imprinted on the electron bunch in the buncher cavity. The longitudinal focus is reached at $z = 6\,\mathrm{m}$, after which the bunch length increases. The plotted lines represent quadratic functions as best fit to the actual particle distribution.

Figure 4.19: Illustration of the ballistic bunching mechanism showing the evolution of the bunch length ζ_{RMS} and of the longitudinal phase space at selected points in the REGAE beamline.

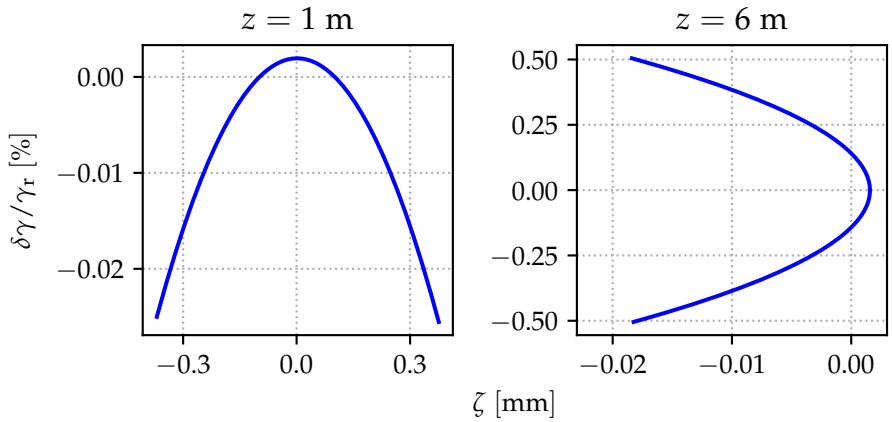

Figure 4.20: Particle distribution in the longitudinal phase space slightly behind the gun at $z = 1$ m (left) and in the longitudinal focus at $z = 6$ m (right) taken from an ASTRA simulation. Both distributions display a parabolic shape. The plotted lines represent quadratic functions as best fit to the actual particle distribution.

As explained in section 2.2.2, the particle distribution in the longitudinal phase is not characterized by a perfectly straight line in the longitudinal focus. Instead, a degree of curvature is visible in the phase space distribution. Closer inspection of the particle distribution in the longitudinal phase space, of which a close-up is shown in figure 4.20 for $z = 1$ m (left) in front of the buncher cavity and for $z = 6$ m in the longitudinal focus (right), reveals a clear nonlinear shape in form of a parabola. As previously discussed, the nonlinear shape of the phase space distribution at the beginning of the beamline, i.e. behind the gun, arises from the intrinsic nonlinear energy correlation due to the curvature of the accelerating field in the gun and from the nonlinear relationship between the velocity and the energy of a relativistic particle. These nonlinearities are transferred to the phase space distribution in the longitudinal focus, where the parabolic shape of the distribution essentially acts as a lower limit to the bunch length in context of the ballistic bunching mechanism.

In this specific case, the bunch length in the longitudinal focus is equal to $\xi_{o,RMS} = 7.38$ fs if the gradient of the buncher cavity is adjusted in such a way that position of the longitudinal focus coincides with the position of the center of the TDS at $z = 6$ m. If space charge effects are included in the simulation, a minimum bunch length of $\xi_{o,RMS} = 14.57$ fs is expected. In this case, the gradient of the buncher cavity needs to be adjusted slightly. Compared to the case where the buncher cavity is switched off, this corresponds to a compression factor of ≈ 30.

Regarding the machine setup procedures, some minor adaptations were necessary to provide suitable beam parameters. The main reason for these adaptations is the focusing/defocusing effect of the buncher cavity. Additionally, the magnet lattice of the REGAE front-end was modified to ensure the correct alignment of the beam trajectory through the buncher cavity. Ideally, the field of the buncher does not lead to a transverse offset of the beam further downstream. At the time

of the measurements, the laser system was only able to deliver a beam charge of $Q = 50\,\mathrm{fC}$.

Once an appropriate magnet setting for the REGAE front-end had been established, the correct buncher phase, i.e. $\phi_b = -90\,\mathrm{deg}$, had to be found. This was done by deflecting the beam onto the scintillator screen of the spectrometer with the dipole magnet, noting down the beam position on the camera image, and then switching on the buncher cavity and tuning the buncher phase until the original beam position was recovered. No net effect with respect to the mean beam energy should be imparted by the buncher.

Strictly speaking, there are two buncher phase settings where the beam experiences no change in energy. In order to identify the correct phase value which leads to a compression of the bunch length, the TDS was switched on and the beam sizes in streaking direction with and without active buncher cavity were compared. The phase value where the streaked beam size under the effect of the buncher cavity is smaller than the streaked beam size of the uncompressed beam, i.e. when the buncher is not active, corresponds to the bunching phase $\phi_b = -90\,\mathrm{deg}$. The second zero crossing is located 180 deg away from the bunching phase and leads to the opposite effect, i.e. corresponds to the debunching phase.

The exact value of the buncher gradient which yields the smallest bunch length in the TDS needs to be determined experimentally. Essentially, the electron bunch length was measured for a variety of buncher gradients around the suspected minimum as determined from ASTRA simulations. Once suitable machine parameters were found, the bunch length was measured at the D2 detector setup. A more thorough description of the measurement procedure can be found in the preceding sections.

In the time between the first measurements of the uncompressed bunch, presented in section 4.3.3, and the measurements in context of the ballistic bunching scheme, some improvements on the photocathode laser system were implemented[10]. This includes the integration of a pinhole imaging setup to produce a transverse uniform distribution in the laser pulse. However, the current state of the laser system does not feature diagnostic elements to determine the pulse duration or the exact spot size on the cathode.

A summary of the bunch lengths measured in the course of the buncher gradient scan is shown in figure 4.21. The data points are marked in black. Up to this date, the shortest measured bunch length by employment of the ballistic bunching mechanism at REGAE is $\xi_{RMS} = (18.26 \pm 1.14)\,\mathrm{fs}$, which corresponds to $\zeta_{RMS} = 5.48\,\mu\mathrm{m}$. This is equal to a compression factor of ≈ 25. For comparison, the theoretical bunch length, taken from ASTRA simulations, is shown in the same figure and marked in red. Here, the shortest achievable bunch length amounts to $\xi_{o,RMS} = 14.57\,\mathrm{fs}$, which is equal to $\zeta_{o,RMS}$ =4.37 µm. The error bars in the ASTRA simulations are a consequence of the uncertainty of the pulse duration of the photocathode laser and based on the measurements presented in the previous section.

Comparison of the bunch lengths reconstructed from the measurement data to those obtained from ASTRA leads to the observation that both follow a very similar

10 The improvements were designed with the help of Dr. Chris Werle.

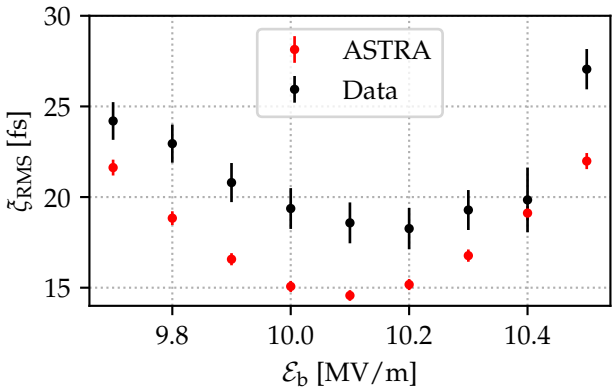

Figure 4.21: Reconstructed bunch length ξ_{RMS} for a variety of buncher gradient setpoints $\mathcal{E}_b$ around the minimum bunch length setting. Both measurement data (black) and bunch lengths expected from ASTRA simulations (red) are shown. Space charge effects were included in the ASTRA simulation. The shortest measured bunch length at REGAE is 18.26 fs.

trend. However, some differences are clearly visible. First and foremost, nearly all measured bunch lengths are slightly higher than the simulation would predict for the respective gradient value. The average difference between measurement and simulation is (3.40 ± 1.24) fs; the deviation in the last gradient setpoint at $\mathcal{E}_b = 10.5\,\mathrm{MV/m}$ is larger than the difference at the other setpoints. Moreover, there appears to be a minor shift along the horizontal axis of the plot, which can be seen when inspecting the gradient at which the respective bunch length minima are located: for the data, the minimum occurred at a buncher gradient of $\mathcal{E}_b = 10.2\,\mathrm{MV/m}$, whereas the ASTRA simulation predicts a bunch length minimum at a gradient of $\mathcal{E}_b = 10.1\,\mathrm{MV/m}$. This can most likely be attributed to calibration errors of the buncher cavity.

The ASTRA values depicted in figure 4.21 are taken from simulations without the TDS. Performing a synthetic measurement with ASTRA, which includes higher order effects from the TDS, yields a minimum reconstructed bunch length of $\xi_{sim,RMS} = 15.91$ fs.

Within the scope of measuring accuracy, it appears that measurement data and ASTRA simulation results are not in full agreement with each other. Having said that, the similarity in terms of the run of the curve of the measurements and simulation, combined with the comparable overall bunch duration scale ($\sim 15 - 20$ fs) of the results, is remarkable. Systematic errors arising from calibration uncertainties of the buncher cavity and higher order effects of the TDS may partially account for the differences between measurement data and simulations. Considering the fact that a number of assumptions had to be made with respect to the simulation parameters, the agreement between measurement and simulation is excellent. A reasonably valid model of the REGAE beamline geometry in ASTRA is crucial and requires sufficiently precise knowledge of many machine properties, which include but are not limited to the correct calibration of cavity gradients and phases as well as calibration of the solenoid magnets, the position of all relevant beamline elements, correct and reproducible energy measurement, reliable charge measurement and last but not least knowledge of the input

Beam property	Measured value
$\langle E \rangle$ [MeV]	3.6634 ± 0.0003
Q [fC]	49.6 ± 1.0
$\xi_{0,\mathrm{RMS}}$ [fs]	18.26 ± 1.14
$\epsilon_{\mathrm{n},x}$ [nm]	65 ± 11
$\epsilon_{\mathrm{n},y}$ [nm]	69 ± 16

Table 4.4: Overview of beam parameters measured in the course of the ballistic bunching measurements.

parameters of the photocathode laser. A final overview of the beam parameters recorded in the course of the ballistic bunching measurements is given in table 4.4. Measurements of the emittance via a solenoid scan yielded a normalized emittance of $\epsilon_{\mathrm{n},x} = (65 \pm 11)\,\mathrm{nm}$ and $\epsilon_{\mathrm{n},y} = (69 \pm 16)\,\mathrm{nm}$, respectively.

All in all, it is likely that the sum of small deviations between the ASTRA model and the actual beamline characteristics in terms of the points listed above are the reason for the difference between the measurement data and the ASTRA simulation. Especially the uncertainty regarding the properties of the photocathode laser pulse is a major factor and requires further investigation in the future. Furthermore, not all beamline elements have been measured and positioned by the DESY measurement group. The exact position and orientation is not always known. Lastly, the dipole steerer magnets used during machine operation were not included in the simulations.

Taking all the abovementioned points into consideration, it is justified to regard the findings as valid measurement results and the ASTRA model as a valid representation of the REGAE accelerator beamline.

4.4 SUMMARY

Prior to the installation of the TDS at REGAE in context of the beamline upgrade, there was no longitudinal diagnostic device included in the beamline. Neither reconstruction of the electron bunch length nor imaging of the longitudinal phase space was possible. In addition to this, operation of the buncher cavity was severely limited, due to the fact that gun and buncher cavity were powered by the same klystron. Due to the presence of significant correlations between the rf settings, independent high precision tuning of the both cavities at the same time was not feasible before the upgrade.

The introduction of deflecting structures dates back to the 1960s. The structure at REGAE was specifically designed to preserve the ultralow transverse beam emittance. It is the first TDS developed to produce linear deflecting fields while maintaining a high rf efficiency. Owing to the unique geometry of the structure, an amplifier suffices as a power source for the TDS due to the high rf efficiency, thus foregoing the high financial cost of another separate rf system. The structure was installed in the course of the extensive REGAE beamline upgrade, during which an additional klystron was installed for decoupled operation of the buncher cavity.

Following initial conditioning after the completion of the beamline upgrade, the REGAE accelerator was operated with reliable performance.

A routine for single-shot bunch length measurement operation of the TDS was successfully established. The associated machine setup procedure was described thoroughly and a standard magnet lattice for a bunch length measurements of the uncompressed bunch has been determined, which is readily accessible during machine operation.

First measurements of the uncompressed bunch length have been performed with the TDS. A calibration scan to experimentally determine the shear parameter of the structure yielded $S = 10.14 \pm 0.19$. For the bunch length measurement, the TDS was operated at zero-crossing. The measured bunch length is equal to $\xi_{\mathrm{RMS}} = (454.06 \pm 9.57)\,\mathrm{fs}$ for a bunch charge of $Q = (105.2 \pm 0.8)\,\mathrm{fC}$ at a beam energy of $\langle E \rangle = (3.6668 \pm 0.0004)\,\mathrm{MeV}$ and is in excellent agreement with ASTRA simulations of the REGAE beamline. The longitudinal resolution of the TDS was measured to be $R_z/c = (33.45 \pm 0.14)\,\mathrm{fs}$. At the time of this measurement, the normalized transverse beam emittance was approximately 100 nm.

Application of the ballistic bunching scheme at the REGAE accelerator beamline enabled the successful production and measurement of an electron beam with a longitudinal extent of $\xi_{\mathrm{o,RMS}} = (18.26 \pm 1.14)\,\mathrm{fs}$. This result marks the shortest measured bunch length using the ballistic bunching mechanism at REGAE up to this date. Improvements of the laser system resulted in a normalized transverse emittance of approximately 65 nm. In view of the general assumptions regarding the beamline geometry of the REGAE model in ASTRA, measurement data and simulations are in excellent agreement.

It has been shown that bunch length measurements carried out with the TDS produce realistic and reliable results. Since the ballistic bunching mechanism does not include a linearization of the longitudinal phase space, the achievable bunch length can in principle be decreased by employing a shorter pulse duration of the photocathode laser [20]. A potential drawback of using extremely short laser pulses (an initial pulse duration of 100 fs was used in [20]) is the fact that the transverse emittance may deteriorate due to increased space charge forces at the cathode. To preserve a high beam quality, it can be advantageous to start with a comparatively long laser pulse duration.

Generally speaking, the attainability of even shorter bunch lengths can be limited by space charge effects and by higher order contributions in the longitudinal phase space distribution. Measurement data geared towards the linearization of the longitudinal phase space is presented in the next section.

5 LONGITUDINAL PHASE SPACE LINEARIZATION

Many electron accelerator facilities perform experiments where very short bunch lengths are required, for example free electron lasers or time-resolved electron diffraction. Other applications, such as time-resolved transmission electron microscopy, greatly benefit from electron bunches characterized by an extremely small energy spread. While the achievable longitudinal extent of the bunch is also affected by repulsion forces arising from space charge, both bunch length compression and energy spread minimization are both limited by nonlinear correlations in the longitudinal phase space. These nonlinearites in the internal structure of the electron bunch evolve as the beam propagates through the beamline and can ultimately restrict the attainable beam parameters. In order to overcome these limitations, the nonlinearities in the longitudinal phase space need to be eliminated.

Large particle accelerator institutions, such as the European XFEL [13] and the FLASH accelerator at DESY [14], make use of a purpose-built cavity to linearize the longitudinal phase space [15, 112]. This cavity is operated at a higher harmonic frequency of the main rf system.

A novel linearization strategy without the utilization of higher harmonic fields has previously been developed [16]. Numerical and analytical studies for the REGAE beamline demonstrating the feasibility of the method have been published in [17]. The method itself is denoted as *stretcher mode*. It is based on a phase setting of the gun cavity which leads to a controlled expansion of the bunch up until the buncher cavity. The effect of a longitudinally "stretched" bunch propagating through a cavity operated at the fundamental frequency of the main rf system is similar to that of an unaltered bunch traveling through a higher harmonic cavity. Thus, the buncher cavity - after the controlled expansion of the bunch - can be used to linearize the longitudinal phase space and effectively compress the electron bunch. Simulations including space charge forces have indicated an achievable bunch length below 1 fs of the linearized bunch [17].

Essentially, the realization of the stretcher mode described above yields an upright line in the longitudinal phase space, i.e. a compressed bunch of extremely small longitudinal extent. However, the stretcher mode can also be employed to achieve a "horizontal" distribution in the longitudinal phase space, which minimizes the energy spread of the bunch. The initial energy spread accumulated in the gun cavity can be compensated with help of the buncher cavity.

The following section briefly summarizes previous derivations presented in [16, 17] and describes the working principle of the stretcher mode.

5.1 STRETCHER MODE

The energy gain of a particle propagating through a cavity can be written in form of a Taylor expansion

$$\Delta\gamma = \tilde{A}_0 + \tilde{A}_1\zeta_c + \tilde{A}_2\zeta_c^2 + \tilde{A}_3\zeta_c^3, \tag{5.1}$$

where the longitudinal particle coordinate in the co-moving frame at the position of the cavity located at $z = z_c$ is denoted by ζ_c and the cavity coefficients $\tilde{A}_n$ with $n \in [1,3]$ of the Taylor expansion are given in equation 2.46. If two cavities are present in a beamline, as is the case at REGAE, there are a total of four cavity parameters which can freely be adjusted independent of each other, namely the gradients and phases of the respective cavities. The underlying principle of longitudinal phase space linearization is to have the nonlinear terms of both cavities in equation 5.1 cancel each other out exactly by finding suitable cavity settings. For the gun and buncher coefficients $\tilde{G}_n$ and $\tilde{B}_n$, this implies that $\tilde{G}_2 = -\tilde{B}_2$ and $\tilde{G}_3 = -\tilde{B}_3$. Combining this with equations 2.46 and 5.1 ultimately translates into

$$\frac{1}{k}\tan(\phi_g) = \frac{1}{k}\tan(\phi_b), \tag{5.2}$$

where ϕ_g and ϕ_b are the rf phase values of the gun and buncher cavity and k is the wave number at which the cavities are operated at. This in turn leads to $L_g\mathcal{E}_g = -L_b\mathcal{E}_b$; the cavity amplitudes are proportional to the product $L_c\mathcal{E}_c$. Consequently, longitudinal linearization would lead to a complete deceleration of the electron bunch, since the second cavity, i.e. the buncher cavity, would negate the energy gained by the beam in the gun cavity.

However, this implication loses its validity if the cavities are operated at different frequencies, which leads to different wave numbers k_g and k_b. This is the fundamental principle of a higher harmonic cavity, which can be operated at tripled frequency so that the sum of the fields acting on the electron beam effectuate a flat longitudinal profile [15, 112]. Such a type of cavity is typically installed as an addition to the main cavities in an accelerator beamline. Considering the fact that a separate rf system needs to be implemented for a higher harmonic structure, this method of phase space linearization can entail high financial costs.

The method derived in [17] does not require a potentially expensive higher harmonic cavity. Rather than employing a separate cavity operated at a higher harmonic frequency, the proposed linearization concept relies on the controlled expansion between the gun cavity and the buncher cavity. The increase in bunch length effectuates a reduction in curvature in the longitudinal phase space. This effectively increases the curvature of the field in the buncher cavity as seen by the elongated electron bunch. The crucial point here is the fact that only gun and buncher cavity are required and both are operated at the same fundamental rf frequency. The resulting overall effect is comparable to that of a higher harmonic structure in the sense that higher order contributions in the longitudinal phase space are effectively eliminated.

The main difference between stretcher mode and a higher harmonic system with respect to the the gun cavity is the fact that the gun cavity is operated at an

off-crest phase in stretcher mode. This means that the gun phase is set to a value which does not yield the maximum energy gain. As a result, the assumptions leading to equation 5.2 do not hold true anymore. In the stretcher mode, there exists a configuration of cavity parameters, i.e. amplitudes and phases of the gun cavity and the buncher cavity operated at the same frequency, which produces a linearized phase space distribution in the longitudinal focus.

At this point it should be mentioned that the linearized concept described above is not intrinsically limited to the production of a vertical line in the longitudinal phase space. In other words, the stretcher mode can also be utilized to minimize the energy spread instead of the longitudinal extent of the electron bunch, thus yielding a "horizontal" phase space distribution. A solution of the problem exists where the configuration of the cavity parameters linearizes the longitudinal phase space distribution in a way that the energy spread from the curvature in the gun cavity is compensated by the buncher cavity.

Both of the linearization options are based on the same procedure, which is summarized in the next section.

5.1.1 Linearization Procedure

In order to calculate the cavity parameters of the linearization method, a mathematical procedure has been developed [17]. The foundations for this have already been described in section 2.2.2. Essentially, it is assumed that the structure of the particle distribution in the longitudinal phase space can be described by a function, i.e. there are no ambiguities in ζ. The effects of the cavities and drift sequences are written in form of a Taylor expansion.

The full details of this mathematical formalism are given in [16], on which the following summary of the linearization procedure is based. The individual steps are illustrated in figure 5.1, where an ASTRA simulation of the bunch length evolution in stretcher mode operation is shown.

1. The electron bunch is produced at the cathode. The initial particle distribution is specified externally. Apart from the requirement of possessing a functional representation, i.e. being describable by a continuous curve, in principle any arbitrary particle distribution can be used. Due to the fact that the strong phase slippage within the gun make an analytical description rather complicated and tedious [113], the energy gain the electron beam experiences in the gun is obtained from an ASTRA simulation. The accuracy of the analytical description presented in [113] is not sufficient for this purpose. At the end of the gun cavity, the longitudinal phase space coordinates are given by

$$\left[\zeta_g, \sum_n G_n \zeta_g^n\right], \tag{5.3}$$

   where ζ_g denotes the longitudinal coordinate and G_n are the Taylor coefficients for energy distribution from the gun cavity.

2. The buncher cavity is separated from the gun cavity by a free drift segment. While the mean beam energy does not change in this section, the bunch

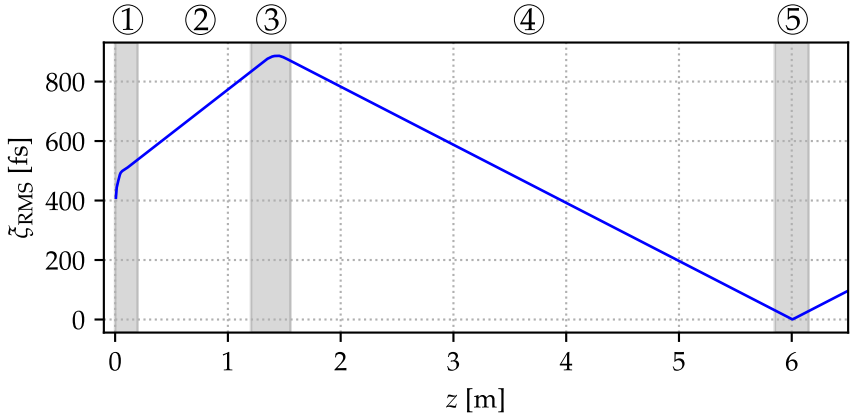

(a) Evolution of the electron bunch length ξ_{RMS} along the REGAE beamline in stretcher mode simulated with ASTRA. The positions of the gun and buncher cavities are marked gray; the TDS position is also marked.

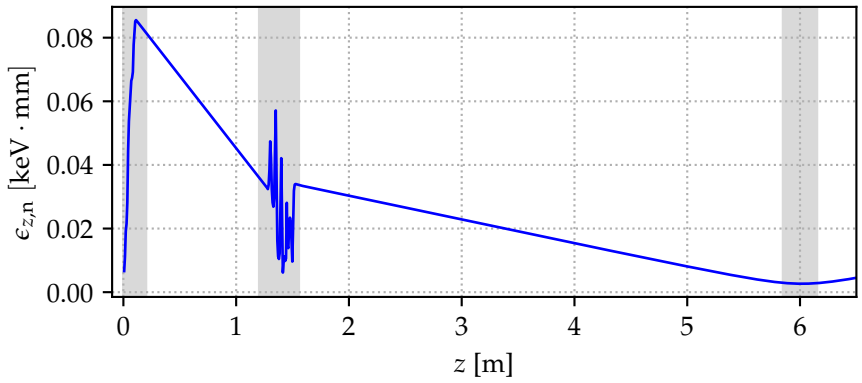

(b) Evolution of the longitudinal emittance $\epsilon_{z,n}$ along the REGAE beamline in stretcher mode simulated with ASTRA. The positions of the gun and buncher cavities are marked gray; the TDS position is also marked. It has been shown that, in order to eliminate second order contributions to the longitudinal phase space in the focus, the position of the minimal bunch length must coincide with a local minimum of the longitudinal emittance.

Figure 5.1: Exemplary representation of the stretcher mode linearization scheme. The evolution of the bunch length ξ_{RMS} (figure 5.1a) and of the longitudinal emittance $\epsilon_{z,n}$ (figure 5.1b) are shown. The corresponding beamline sections have been labeled according to the respective step in the linearization procedure. The gun cavity is operated at an off-crest phase which causes the bunch length to increase in the subsequent drift. The parameters of the buncher cavity are set in such a way that the bunch length decreases and the second order vanishes in the longitudinal focus. Specifically the buncher gradient has been set to a value which places the position of the longitudinal focus at the center of the TDS. Space charge effects were not included. Figure adapted from [17].

length increases due to the present energy spread. The fact that this expansion occurs in a controlled way is one of the key points of the stretcher mode; the gun phase ϕ_g is set to an off-crest value. As already described in section 2.2.2, this leads to the build-up of additional curvature. This effect is represented by equation 2.44, which implicates an alteration of the longitudinal coordinate $\zeta(z)$ in the free drift segment with $z_g \leq z \leq z_b$, where z_g and z_b denote the positions of the gun and buncher cavity in the beamline, respectively. In the drift interval, the phase space coordinates can by expressed as

$$\left[\sum_n \chi_n(z)\zeta_g^n, \sum_n g_n(z)\zeta^n(z)\right], \tag{5.4}$$

where $\chi_n(z)$ contain the coefficients of equation 2.44 and the coefficients $g_n(z)$ replace the previous G_n in order to compensate for the kinetic effects in the drift segment and thus preserve the value of the energy coordinate (see [16] for a thorough mathematical derivation and description).

3. The buncher cavity leads to an energy gain of the particles in the bunch. The buncher itself is regarded in context of the thin lens approximation, which means that the effect on the particle's energy is assumed to be instantaneous. Furthermore, it is assumed that the longitudinal coordinate remains constant. Since the energy gain resulting from the buncher can be written in form of equation 5.1, the coefficients can be added to the existing energy distribution of the incoming electron bunch. This leads to an expression of the form

$$\left[\sum_n \chi_n(z_b)\zeta_g^n, \sum_n B_n\zeta_b^n\right] \tag{5.5}$$

for the longitudinal phase space coordinates, in which the coefficients B_n of the energy polynomial are a sum containing the initial energy distribution and the effects of the buncher cavity.

4. The free drift segment behind the buncher is treated in a manner similar to step 2. Analogously, the phase space coordinates read

$$\left[\sum_n X_n(z)\zeta_b^n, \sum_n b_n(z)\zeta^n(z)\right] \tag{5.6}$$

for values of z in the interval $z_b \leq z \leq z_f$, where z_f denotes the position of the longitudinal focus.

5. In the longitudinal focus, the polynomial functions need to be evaluated at $z = z_f$. At this point, a description of the energy coordinate by means of a mathematical function is no longer possible, since multiple electrons occupy the same longitudinal coordinate at $z = z_f$. Instead of writing the energy coordinate as a function of $\zeta_f = \zeta(z_f)$, the value at the exit of the buncher cavity can simply be used. This yields

$$\left[\sum_n X_n(z_f)\zeta_b^n, \sum_n B_n\zeta_b^n\right] \tag{5.7}$$

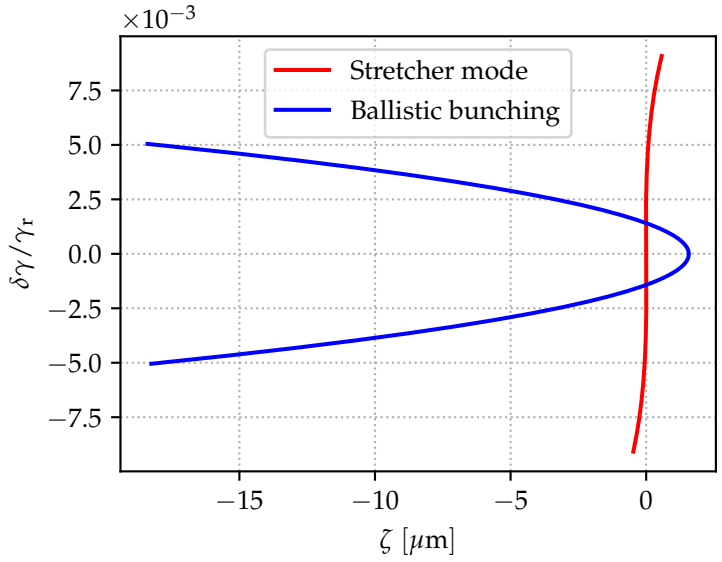

Figure 5.2: Longitudinal phase space distribution at the position of the longitudinal focus simulated with ASTRA. The results from two bunch compression schemes are shown, namely the ballistic bunching mechanism (blue) and stretcher mode (red). While the ballistic bunching mechanism leads to a parabolic phase space distribution, the stretcher mode leads to the manifestation of an S-shaped structure, i.e. the first and second order have successfully been eliminated and the third order is clearly visible. Space charge forces were not included in these simulations.

for the longitudinal phase space coordinates at the position of the longitudinal focus.

With this formalism, the phase space coordinates in the gun cavity are mapped to the position of the longitudinal focus. In order to eliminate higher order terms of the longitudinal distribution and thus minimize the bunch length, the coefficients $X_n(z_f)$ in equation 5.7, which depend on the cavity parameters, must be set to zero. This leads to a set of equations depending on up to which order the nonlinearities should be eliminated. Ultimately, the solution yields a set of cavity parameters which yield a vertical line in the phase space distribution at the position of the longitudinal focus. It should be noted that the rf phase of the cavities appears in trigonometric functions in the system of equations $X_n(z_f) = 0$, while the amplitudes of the cavities contribute in linear terms. The method of solution of these transcendent equations is elaborated in [16].

A correction of the second order can be achieved by solving $X_1 = 0$ and $X_2 = 0$. In this case, a set of solutions exists due to the fact that the gun phase can be chosen arbitrarily, albeit within a restricted interval. A comparison of the longitudinal phase spaces for the ballistic bunching mechanism and the stretcher mode is visualized in figure 5.2. Both phase space distribution were simulated with ASTRA. As already discussed in section 4.3.4, the clearly visible parabolic shape of the distribution limits the bunch length to a minimum of $\xi_{\mathrm{RMS}} = 7.38\,\mathrm{fs}$. With the use of the stretcher mode, it is possible to eliminate second order nonlinearities. This results in an S-shaped structure in the longitudinal phase

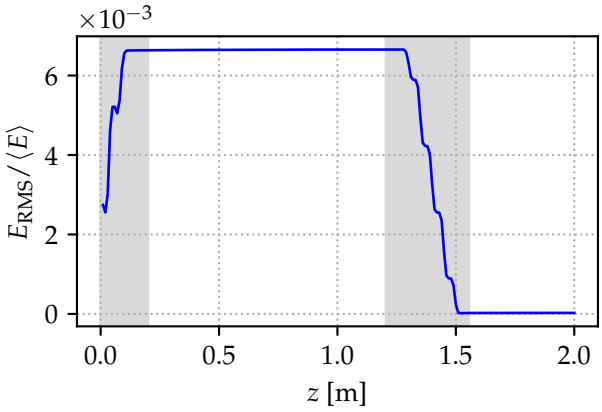

Figure 5.3: ASTRA simulation showing the evolution of the RMS energy spread E_{RMS} of the electron beam in the case of the energy spread compensation scheme of the stretcher mode. The buncher cavity is used to eliminate the energy spread built up in the gun cavity. Both cavity positions are marked in gray. Space charge forces were included in this simulation.

space. The bunch length in the longitudinal focus is equal to $\zeta_{RMS} = 358\,as$, i.e. $\zeta_{RMS} = 107\,nm$ (without space charge). In this case, the gun cavity parameters were set to $\mathcal{E}_g = 80.00\,MV/m$ and $\phi_g = 34.10\,deg$, and the buncher cavity parameters were set to $\mathcal{E}_b = 14.18\,MV/m$ and $\phi_b = -106.15\,deg$, respectively.

It is also possible to to apply the stretcher mode linearization procedure to the energy coordinate, i.e. minimizing the energy spread of the particle beam. The energy spread accumulated by the electron bunch during the emission process in the gun cavity can be compensated by the buncher cavity. This would yield a horizontal line instead of a vertical line distribution in the longitudinal phase space. For this application, it is sufficient to describe the propagation of the beam up until the buncher cavity. This corresponds to step 3 in the linearization procedure described above. Ultimately, the coefficients B_n in equation 5.5 in step 3 must be set to zero to eliminate the nth order of the energy distribution.

An ASTRA simulation with a cavity configuration eliminating first and second order contributions in the energy distribution yields an expected energy spread of about 60 eV at a mean beam energy of 3.12 MeV, which corresponds to a relative energy spread of $E_{RMS}/\langle E\rangle = 1.9 \cdot 10^{-5}$. The initial pulse duration was set to the value obtained in the course of the autocorrelator measurements in section 4.3.3. The gun cavity parameters were set to $\mathcal{E}_g = 80.00\,MV/m$ and $\phi_g = 45.00\,deg$, which resulted in buncher cavity parameters equal to $\mathcal{E}_b = 9.24\,MV/m$ and $\phi_b = -72.80\,deg$, respectively.

For both energy spread compensation and bunch compression schemes of the stretcher mode, cavity settings which eliminate first and second order contributions in the longitudinal phase space have been determined for the REGAE beamline. The following section provides experimental verification as a proof of concept for the stretcher mode as a linearization strategy.

5.2 PROOF OF CONCEPT

It has been shown that the achievable bunch length with the bunch compression scheme of the stretcher mode can be below 1 fs if the cavity parameters are adjusted so that the third order vanishes as well [17]. This is far below the resolution of the transverse deflecting rf structure installed at REGAE. Similarly, a relative energy spread $< 10^{-4}$ obtained via energy spread compensation, i.e. an RMS energy spread of $E_{\mathrm{RMS}} \approx 60\,\mathrm{eV}$ at mean beam energies in the range of $\langle E \rangle = 3\,\mathrm{MeV}$, cannot be resolved with the spectrometer setup installed at the REGAE beamline.

In an attempt to overcome this problem, the initial pulse duration of the photocathode laser was increased. This increases the minimum attainable energy spread after application of the energy spread compensation scheme, and may also increase the bunch length in the longitudinal focus using the compression scheme of the stretcher mode. This was accomplished by mounting glass blocks in the UV segment of the laser propagation path. Due to the lack of diagnostic elements, a measurement of the resulting pulse duration was not possible.

Nevertheless, it is possible to establish a proof of concept by considering the development of the curvature in the longitudinal phase space in a parameter region around the optimal cavity settings. If the linearization procedure is carried out with success, the structure of the phase space distribution should give rise to an S-shaped form, due to the fact that the first and second order vanish.

5.2.1 Energy Spread Compensation

From a practical point of view, the real cavity parameters of the energy spread compensation scheme can be determined by fixing the parameters of the gun cavity and performing a two-dimensional parameter scan of the buncher gradient and phase during machine operation. In the case of second order correction, a solution exists for each gun phase within a restricted domain; not every gun phase value is suitable for linearization. The aforementioned calculated cavity parameters can naturally be used as a starting point, but it is likely that the actual machine settings will differ slightly from the cavity configuration obtained from the theoretical model. Hence, a scan of the parameters can be used to fine-tune the buncher cavity settings. The principle of such a scan is illustrated in figure 5.4, which shows an ASTRA simulation of the energy spread for a multiplicity of buncher cavity settings for $\mathcal{E}_{\mathrm{g}} = 80.00\,\mathrm{MV/m}$ and $\phi_{\mathrm{g}} = 45.00\,\mathrm{deg}$. An initial laser pulse duration of approximately 2.1 ps was assumed as a rough estimate based on ASTRA simulations in combination with the measured bunch length of about 1.4 ps. The red areas mark cavity configurations where the relative energy spread reaches minimal values. Space charge effects were not included in this simulation set.

For the purpose of approaching the actual measurement procedure with realistic expectations and a better understanding of the behavior of the beam in the energy spread compensation scheme, it is constructive to investigate the characteristics of the longitudinal phase space in a buncher cavity parameter region around the minimum energy spread. An analysis of this parameter region

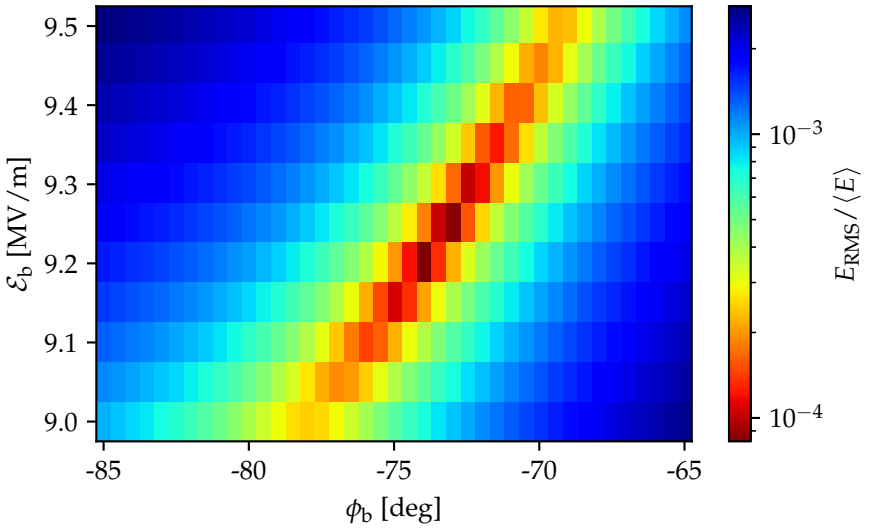

Figure 5.4: Two-dimensional parameter scan of the buncher gradient $\mathcal{E}_b$ and phase ϕ_b performed with ASTRA. The scan was performed around the (suspected) optimal energy spread compensation configuration where the second order vanishes and the relative energy spread $E_{RMS}/\langle E\rangle$ reaches its minimum. The color code marks the value of the relative energy spread for each buncher configuration within the scan interval. Space charge forces were not included in these simulations.

simulated in ASTRA is depicted in figure 5.5. Space charge effects were excluded in order to generate an unperturbed depiction of the internal bunch structure. For each parameter set consisting of a distinguished amplitude and phase value of the buncher cavity, a cubic fit of the form $f(\zeta) = a_3\zeta^3 + a_2\zeta^2 + a_1\zeta + a_0 = \gamma(\zeta)$ has been applied to the particle distribution in the longitudinal phase space. The first and and second order coefficients a_1 and a_2 are plotted together with the relative energy spread $E_{RMS}/\langle E\rangle$ as a function of the buncher phase. The value of the buncher gradient is specified in the title of the respective subplot.

The buncher gradient at which both first and second order fit coefficients are equal to zero for a distinct buncher phase value marks a cavity configuration where the longitudinal phase space is linearized in the sense of the stretcher mode linearization model. First and second order contributions have successfully been eliminated. Upon further inspection of the simulation results shown in figure 5.5 it becomes apparent that the linearization and energy spread minimization occur at different cavity configurations. This is due to the fact that a non vanishing slope, i.e. $a_1 \neq 0$, partially compensates the now dominant third order contributions [16].

From the analysis shown in figure 5.5 it can be deduced that the first and second order contributions in the longitudinal phase space distribution are eliminated for $\mathcal{E}_b = 9.24\,\mathrm{MV/m}$ and $\phi_b = -72.80\,\mathrm{deg}$ as parameters for the buncher cavity. Here, the relative energy spread reads $E_{RMS}/\langle E\rangle = 1.3 \cdot 10^{-4}$. Note that the relative energy spread takes on its minimal value of $E_{RMS}/\langle E\rangle = 0.8 \cdot 10^{-4}$ at a slightly different buncher phase $\phi_b = -73.30\,\mathrm{deg}$ due to the reason specified above. The mean beam energy behind the buncher cavity amounts to $\langle E\rangle = 3.082\,\mathrm{MeV}$.

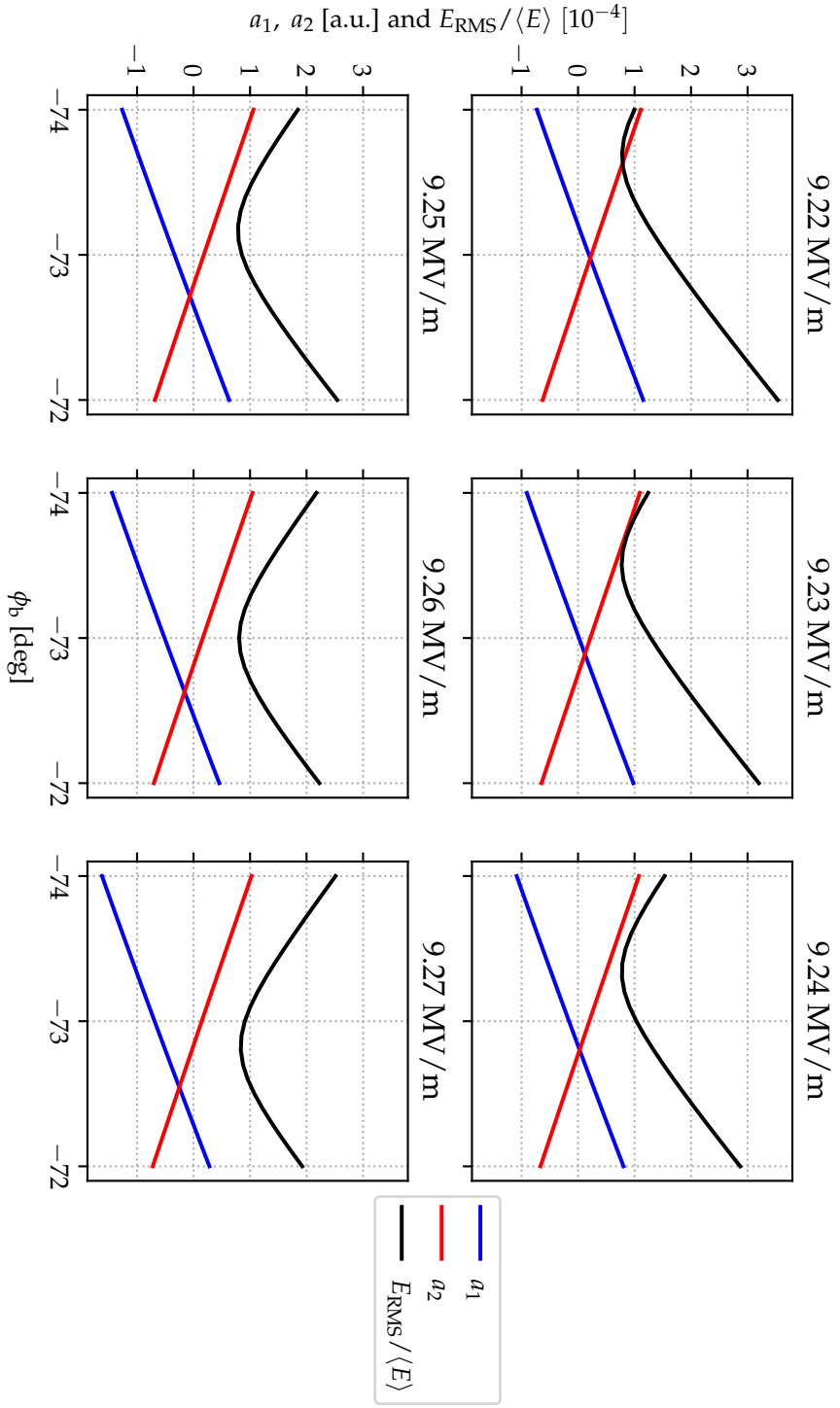

Figure 5.5: Relative energy spread $E_{\mathrm{RMS}}/\langle E\rangle$ (black) as well as first (blue) and second (red) order fit coefficients a_1 and a_2 of a cubic fit to the longitudinal phase space distribution for buncher phase scans simulated with ASTRA for a subset of buncher gradients. The values of the fit coefficients have been scaled to the order of magnitude of the relative energy spread. A cavity setting where both first and second order fit coefficients vanish corresponds to energy spread compensation in the sense of second order correction.

An overview of the evolution of the longitudinal phase space for $\mathcal{E}_b = 9.24\,\mathrm{MeV}$ in dependency of the buncher phase can be seen in figure 5.6. The phase space distribution simulated with ASTRA is shown for a variety of buncher phase values, which have been varied with a step width of 0.50 deg. A cubic fit has been applied to each particle distribution and is plotted as a red line. It can clearly be seen that the phase space distribution is well described by a third order polynomial function.

Some further remarks regarding the evolution of the longitudinal phase space are in order. First and foremost, the decrease in energy spread as the buncher phase approaches the optimal phase value (at $\phi_b = -72.80\,\mathrm{deg} = \phi_{lin}$) is clearly visible since all subplots share the same axis limits. At $\phi_b = \phi_{lin} - 4.00\,\mathrm{deg}$, the distribution has a relatively large extent in $\delta\gamma/\gamma_r$. The vertical extent of the distribution can be connected to the (relative) energy spread of the electron bunch, which is equal to $E_{RMS}/\langle E\rangle = 6.6 \cdot 10^{-4}$ at this point. The energy spread then continuously decreases until the minimum value of $E_{RMS}/\langle E\rangle = 0.8 \cdot 10^{-4}$ is reached, after which it begins to increase again.

Furthermore, the principle of the stretcher mode as a method of phase space linearization can be observed in these simulations. In the parameter region around the optimal cavity configuration at $\phi_b \to \phi_{lin}$ the unperturbed S-shape of the third order becomes visible. As explained above, the first and second order, i.e. the linear and quadratic fit coefficients a_1 and a_2, tend towards zero here, and only higher order terms remain. For phase values further away from the linearized setting, the second order contributes significantly and causes distortions of the "pure" S-shape of the phase space distribution. The expected energy spread for 30 fC obtained from subsequent simulations of the energy spread compensation scheme is around of $E_{RMS,sim}/\langle E\rangle = 1.5 \cdot 10^{-4}$.

The measurements presented in the following focus on an analysis of the degree of curvature in the longitudinal phase space distribution within a parameter region around the optimal cavity configuration.

A similar machine setup procedure as described in section 4.2.1 was carried out. In fact, the magnet lattice obtained from the proceedings explained in that section was used as part of the initial parameters. The electron beam was then visualized on the scintillator screen installed at the dipole spectrometer setup. Starting with the accelerating phase in the gun cavity, i.e. $\phi_g = 0$, the gun phase was successively regulated towards $\phi_g = 45.00\,\mathrm{deg}$ (see section 5.1.1). A reference beam image for $\phi_g = 0$ is shown in figure 5.7, which represents the particle distribution in the longitudinal phase space (ζ, γ) due to the combined effect of TDS and dipole spectrometer. Here, $\delta\gamma$ denotes the energy difference with respect to the mean $\langle\gamma\rangle$.

During the stepwise adjustment of the gun phase, the mean beam energy continuously decreased and because of this, the dipole current also had to be decreased to keep the beam visible on the camera image. At the same time, a strong increase in the energy spread of the beam could be observed. Initially, the measured value of the relative energy spread reads $E_{RMS}/\langle E\rangle = (4.7 \pm 0.1) \cdot 10^{-4}$.

At $\phi_g = 45.00\,\mathrm{deg}$, the energy spread increased to $E_{RMS} = 86\,\mathrm{keV}$ (according to ASTRA simulations), resulting in a relative energy spread of $E_{RMS}/\langle E\rangle \approx 3.1 \cdot 10^{-2}$. Direct measurements of the energy spread were no longer possible, due to the

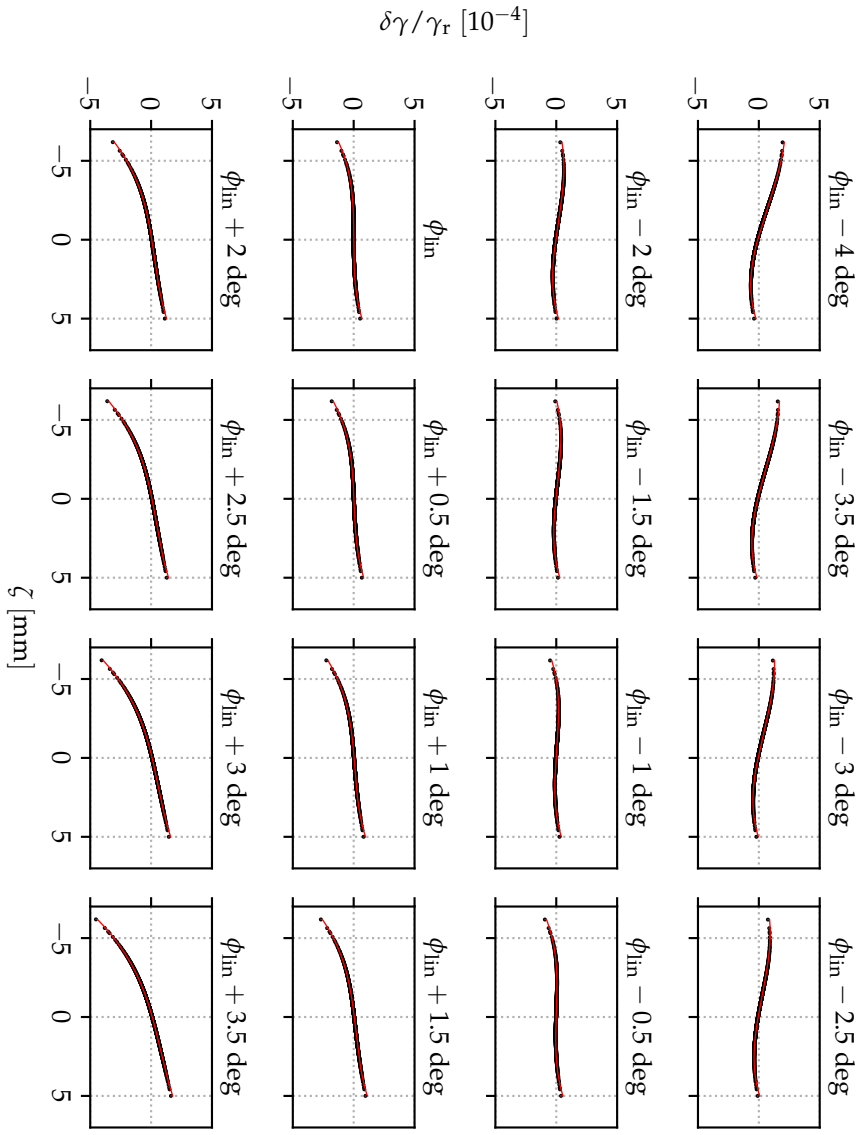

Figure 5.6: ASTRA simulations of the longitudinal phase space for a variety of buncher phase settings at a fixed gradient of $\mathcal{E}_b = 9.24\,\mathrm{MV/m}$. A cubic fit (red) has been applied to each particle distribution (black). The vanishing of the first and second order makes the third order clearly visible.

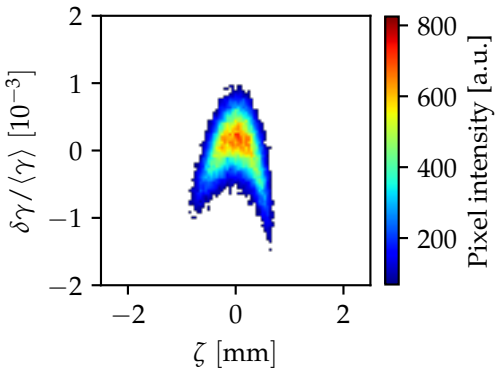

Figure 5.7: Processed camera image of the streaked beam recorded at the dipole spectrometer setup. Due to the combination of TDS and dipole magnet, the longitudinal phase space is imaged. The existing curvature of the phase space distribution is clearly visible.

fact that the beam occupied a larger energy interval than the range defined by the boundaries of the camera image. At this point, the mean beam energy decreased from 3.667 MeV to 2.766 MeV[1]. Concurrently, a noticeable rise in total bunch charge occurred. The attenuator in the UV segment of the photocathode laser was adjusted to counteract this effect in order to keep the bunch charge on the level of $Q = 30\,\mathrm{fC}$ in order to reduce perturbations arising from space charge effects. However, due to the drastic increase in energy spread at a constant bunch charge, the area occupied by the beam signal on the camera image grew significantly while the total beam intensity remained unchanged. Thus, the camera gain of the respective Andor camera was increased to instantiate a higher apparent brightness of the camera image. This facilitated "following" the beam visually on the camera image while manipulating the gun phase.

Once the correct gun phase value was adjusted, some minor alterations regarding the magnet settings in the REGAE front-end were necessary. More specifically, the current through the magnets in front of the buncher cavity were reduced. Especially the focusing strength of solenoid 1 was decreased. These required changes are a result of the lower beam energy at the respective gun phase.

Next, the buncher cavity was activated. The gradient was set to the value $\mathcal{E}_\mathrm{b} = 9.24\,\mathrm{MV/m}$, which was obtained from previous ASTRA simulations. The alignment of the electron beam through the buncher cavity was still reasonably good, which is why no further adjustments of the steerer magnets in front of the buncher seemed necessary. The buncher was also stepwise adjusted towards the nominal value of $\phi_\mathrm{b} = \phi_\mathrm{lin}$. As was the case with the gun phase adjustment, the dipole current had to be changed in accordance with the mean beam energy in order to keep the beam signal on the camera image. In addition to this, the focusing strength of solenoid 6/7 was altered in order to focus the beam onto the scintillator screen of the dipole spectrometer. This served the purpose of increasing the contrast of the image.

At this point, it should be noted that while the rf parameters according to ASTRA provide a good starting point, it is to be expected that the real cavity

1 This value was also obtained from an ASTRA simulation.

settings will differ somewhat from the simulated values. There are multiple reasons for this, for example calibration errors of the cavities and position and alignment inaccuracies of cavities and magnets. Instead of viewing the ASTRA parameters as fixed values, from an experimental point of view it is better to use these settings as guidelines and determine the real cavity configuration by directly investigating the longitudinal phase space.

As the cavity parameters of the buncher approached the optimal settings dictated by the energy spread compensation scheme, $E_{\mathrm{RMS}}/\langle E \rangle$ of the electron beam decreased significantly. Once a suspected optimal cavity configuration was found, collimators were driven into the path of the beam to reduce the dark current visible on the camera image, which posed significant complications in the course of the image processing routines. Special care was taken to avoid cutting away outer regions of the beam. Thus, the entire charge was transported through the collimator. In practice, only the collimators at DDC1 provided a satisfactory effect.

Finally, the TDS was switched on. Combined with the dipole spectrometer, it is possible to image the longitudinal phase space. The TDS was not operated at full power, since the curvature of the phase space distribution was already clearly visible at lower power settings, and too high of a power setting caused the vertical (i.e. longitudinal) extent of the beam to be larger than the boundaries of the camera image. This was due to the extremely large bunch length. The gun cavity is operated at a phase setting of $\phi_{\mathrm{g}} = 45.00\,\mathrm{deg}$, which is an expanding phase (as is required by the stretcher mode concept). Therefore, the bunch length increases up until the buncher cavity, which negates the expansion and after which the bunch length remains constant. Behind the buncher cavity, the longitudinal extent of the bunch is slightly below 4.9 ps.

Similarly to the preparations preceding the bunch length measurements presented in section 4, the electron beam was aligned through the TDS with the help of dipole steerer magnets between the buncher cavity and the deflecting structure. As was the case in previous measurements, the beam should not receive any net energy gain upon passage through the structure. Moreover, the rf phase of the TDS was adjusted to the zero-crossing, i.e. the phase was set to a value where the central particle of the electron bunch propagates through the structure without experiencing a change in transverse momentum.

Lastly, the peak field of solenoid 6/7 was adjusted to produce a focused beam on the scintillator screen of the dipole spectrometer setup. Due to the fact that the optimal buncher settings for energy spread compensation, especially the buncher gradient, needed to be precisely determined experimentally, the solenoid current had to be adapted according to the respective buncher gradient. This is because the fields of the buncher cavity have a focusing/defocusing effect on the electron beam, and the field of solenoid 6/7 had to be adjusted to preserve a focused beam on the camera image of the spectrometer.

After satisfactory completion of the machine setup procedure, a two-dimensional parameter scan of the buncher cavity parameters was performed. The scan replicates the idea of the simulation results presented in figure 5.4. First, the buncher gradient was fixed to a selected value. Then a scan of the buncher phase around the phase value where the curvature was suspected to vanish was performed.

The parameter range was chosen by visual evaluation of the live camera images on the spectrometer screen. The TDS was active throughout the scan, so that the longitudinal phase space was recorded for each distinct cavity configuration. Due to both beam and dark current jitter on the camera images, the calibration of the TDS bears an uncertainty on the level of 20 %. This can mainly be ascribed to rf jitter of all three cavities, though the exact reason behind the dark current jitter is still being explored.

At each buncher phase setpoint, a total of 10 beam and background images were recorded. Background subtraction and array centering was performed as described in section 4.2.2. Since the resulting image profiles displayed a clear non-Gaussian shape in some cases, the beam intensity cut routine did not always yield reliable results and thus proved to be inapplicable. Therefore, the region growing algorithm outlined in the abovementioned section was utilized.

The recorded camera images do not depict a "pure" representation of the longitudinal phase space. This is because the transverse distribution of the particles in the electron bunch also contribute to the beam signal on the image. Hence the energy axis is, strictly speaking, a convolution of the horizontal beam profile and the energy distribution, whereas the longitudinal axis in the images is actually a convolution of the vertical and longitudinal beam profiles. From a purely mathematical standpoint, it is possible to perform a deconvolution of the longitudinal and vertical charge distributions, since the unstreaked image reflects the unperturbed vertical beam profile. Unfortunately, deconvolution procedures using the transverse distributions recorded without the TDS did not yield conclusive results. This can most likely be ascribed to inaccuracies resulting from dark current jitter, which can falsify the beam signal due to the background subtraction process, or to the presence of internal correlations within the electron bunch between the transverse and longitudinal coordinates of the particles. Deconvolution algorithms were therefore not utilized. A deconvolution of the energy and horizontal distribution was not possible; however, a dispersion-based method to measure the deconvolved energy spread was recently proposed in [114] and could be utilized at REGAE. Studies regarding the feasibility of this method at REGAE will be carried out in the future. The resolution is thus limited by the transverse emittance.

Despite the fact that the axes of recorded camera images are strictly speaking convolved quantities, an analysis based on the fit coefficients of the respective distribution is still possible. A scan of the buncher cavity parameters directly impacts the longitudinal phase space distribution and these changes manifest themselves in the coefficients derived from an applied polynomial fit.

A quantified representation of the results is shown in figure 5.8. The buncher phase was scanned in 0.50 deg steps in a phase interval around ϕ_{lin} at a fixed buncher gradient of $\mathcal{E}_{\mathrm{b}} = 8.85\,\mathrm{MV/m}$. The fit coefficients of the cubic fits are shown for each respective buncher phase setpoint. The first order coefficient a_1 is shown in blue, and the second order coefficient a_2 is plotted in red. In addition to this, a linear fit has been applied to the values of the fit coefficients. The purpose of this is to allow a comparison to the linear progression expected from ASTRA simulations shown in figure 5.5. The general progression is identical, and

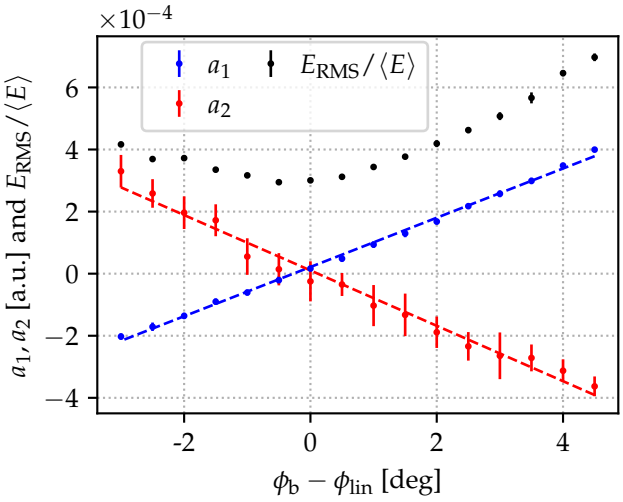

Figure 5.8: Experimental results of the energy spread compensation scheme where the first and second order fit coefficients a_1 and a_2 (blue and red) vanish at nearly the same cavity configuration. The dashed lines mark a linear fit through the data, which constitutes the expected run of the curve dictated by ASTRA simulations. The relative (convolved) energy spread $E^*_{\mathrm{RMS}}/\langle E\rangle$ is also shown as a function of the buncher phase $\phi_\mathrm{b} - \phi_\mathrm{lin}$ with respect to ϕ_lin.

measurement results and ASTRA simulations display the same behavior for both fit coefficients.

Each data point represents the mean value calculated from ten beam signal arrays. The error bars stem from the respective variance and from the covariance matrix determined in the course of the fit routine, combined with an error based on the uncertainty of the region growing algorithm and intrinsic uncertainties of the dipole spectrometer arising from unknown offsets and angles at the entrance to the dipole, which is assumed to be on the level of 1 %.

Nevertheless, it can be seen that the first and second order vanish at nearly the same cavity configuration. The buncher phase values for $a_1 = 0$ and $a_2 = 0$, if deduced from the linear fit, are approximately only 0.60 deg apart from each other. The phase value ϕ_lin marks the setpoint where the data points of the first and second order are closest to zero. Out of all the buncher phase scans performed at different buncher amplitude values, this particular dataset contains the cavity settings where $\Delta\phi_{\mathrm{b,fit}}(a_{1,2}) = \phi_\mathrm{b}(a_1 = 0) - \phi_\mathrm{b}(a_2 = 0)$ assumes its smallest value. In order to effectuate $\Delta\phi_{\mathrm{b,fit}}(a_{1,2}) \to 0$, an even finer adjustment of the buncher gradient is required. This is beyond the currently achievable precision of the rf parameters at the REGAE beamline.

An important aspect to note is the fact that the choice of ϕ_lin for $\Delta\phi_{\mathrm{b,fit}} \neq 0$ is ambiguous for this specific scenario. The buncher phase is uniquely defined in conjunction with the buncher gradient for a distinct gun phase. In other words, if the gun phase is has been fixed, a single unique set of buncher parameters exists in the sense of the linearization model. However, if the buncher amplitude has not been set to the correct value as dictated by the stretcher mode, the nominal theoretical phase value loses its validity. Naturally, this ambiguity vanishes if the buncher gradient has been adjusted accordingly.

The relative (convolved) energy spread as a function of the setpoint values of the buncher phase is also displayed. It should be noted that the energy spread was calculated from data where the TDS was switched off, since activation of the TDS leads to an induced energy spread. Attention must be drawn to the the fact that the plotted energy spread values still contain a contribution of the horizontal beam size. These quantities should therefore rather be referred to as "convolved" energy spread etc, reminiscent of the convolution of energy and horizontal charge distribution as explained at the beginning of this section. In other words, the pure energy spread is most definitely lower than the measured (convolved) energy spread. The minimum value for the relative convolved energy spread reads $E^*_{\mathrm{RMS}}/\langle E\rangle = 2.9 \cdot 10^{-4}$.

The evolution of the longitudinal phase space in a parameter subspace around the optimal energy spread compensation settings is depicted in figure 5.9. The rf parameters of the gun cavity were set to $\mathcal{E}_{\mathrm{g}} = 80.00\,\mathrm{MV/m}$ and $\phi_{\mathrm{g}} = 45.00\,\mathrm{deg}$, respectively. In this particular buncher phase scan, the gradient of the buncher was set to $\mathcal{E}_{\mathrm{b}} = 8.85\,\mathrm{MV/m}$. The buncher phase was scanned with a step width of 0.50 deg. The processed detector images are shown in figure A.1 in the appendix A. Array centering and region growing has been performed on each background subtracted image. However, it is difficult to directly discern curvature changes in the detector images. For visualization purposes, the detector images were divided into longitudinal "slices", where each slice essentially corresponds to one pixel column of the detector image. For each slice, the relative deviation $\delta\gamma_{\mathrm{s}}/\langle\gamma\rangle = (\gamma_{\mathrm{s}} - \langle\gamma\rangle)/\langle\gamma\rangle$ of the mean slice energy γ_{s} from the the mean beam energy $\langle\gamma\rangle$ was computed and plotted as a black dot in figure 5.9. Thus, each slice distribution is reduced to its mean energy, and the evolution of the phase space curvature is clearly recognizable.

To each individual detector image, a cubic fit of the form $f(x) = a_3x^3 + a_2x^2 + a_1x + a_0 = \gamma(x)$ has been applied, where x contains the longitudinal coordinate ζ in the bunch. The pixel intensities of the image were used as relative weights for the fit routine. The fit results are plotted as red lines in figure 5.9. Similar properties as in the ASTRA simulations shown in figure 5.6 are visible. Since the energy axis again bears the same scale for all subplots, the progression of the energy spread can also be seen. As the buncher phase approaches the optimal energy spread compensation value, the energy spread continuously decreases.

The linearization process can be directly observed in the data. While a high degree of curvature is visible in the distributions at the outer limits of the phase scan, the subplot at $\phi_{\mathrm{b}} = \phi_{\mathrm{lin}}$ for instance constitutes a nearly perfectly linearized distribution, where ϕ_{lin} is in accordance with the analysis presented in figure 5.8.

The focusing strength of solenoid 6/7 was not optimized during this specific measurement presented above. In response to this inconvenience, a solenoid scan with solenoid 6/7 was performed to minimize the contribution of the horizontal beam size on the spectrometer screen. The scan was carried out at the cavity configuration determined in the preceding paragraphs, i.e. $\mathcal{E}_{\mathrm{b}} = 8.85\,\mathrm{MV/m}$ and $\phi_{\mathrm{b}} = \phi_{\mathrm{lin}}$. The resulting (convolved) relative energy spread is as low as $E^*_{\mathrm{RMS}}/\langle E\rangle = (2.4 \pm 0.1) \cdot 10^{-4}$ at a mean beam energy of $\langle E\rangle = 3.077\,\mathrm{MeV}$.

In this regard, a measurement of the beam emittance for the unstreaked beam was also performed via the solenoid scan. At the reconstruction point inside

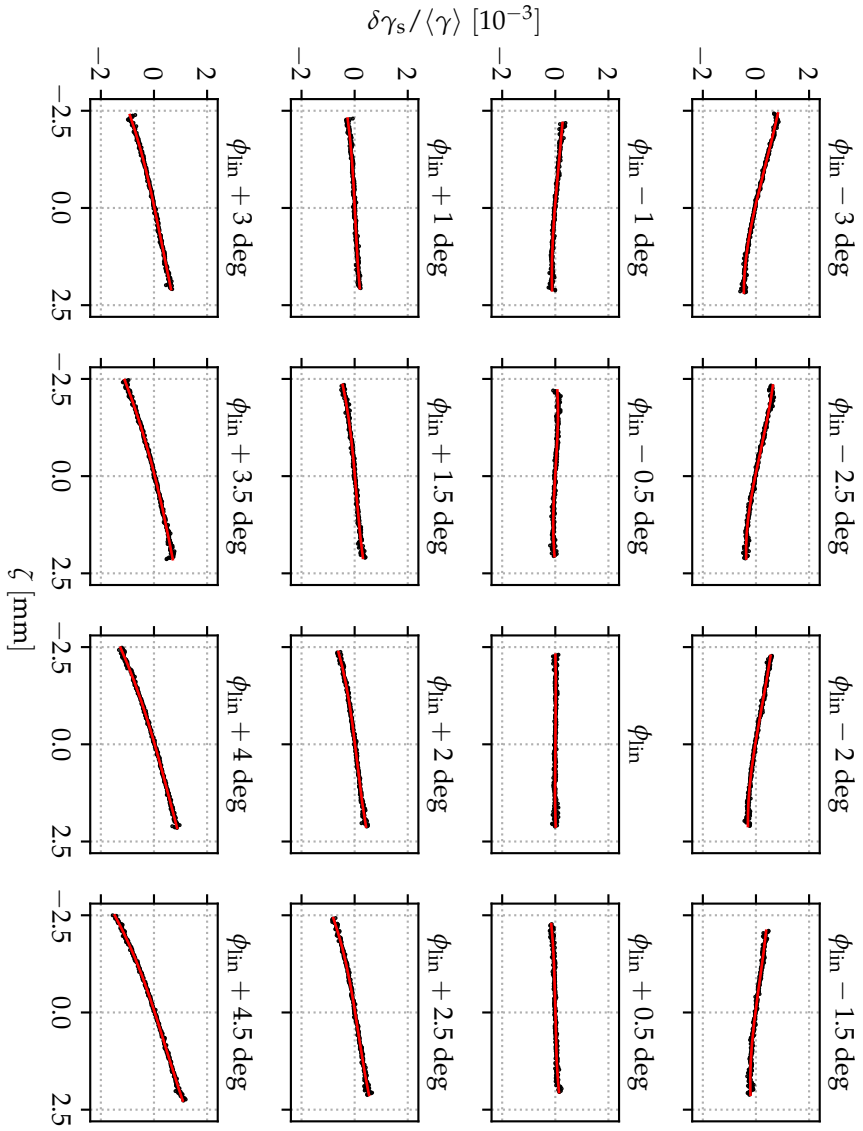

Figure 5.9: Measurement of the longitudinal phase space in dependency of the buncher phase. The gradient of the buncher cavity has been fixed to a setpoint of $\mathcal{E}_b = 8.85\,\mathrm{MV/m}$. The underlying images were recorded at the dipole spectrometer in combination with the streaking effect of the TDS at REGAE (see figure A.1 in the appendix). The black dots mark the relative slice energy deviation $\delta\gamma_s$ with respect to $\langle\gamma\rangle$; see the text for a detailed explanation. A cubic fit (red) has been applied to the distribution where the pixel intensities of the detector images have been used as weights. The general evolution of the longitudinal phase space is very similar to the ASTRA simulations shown in figure 5.6.

Beam property	Measured value
$\langle E \rangle$ [MeV]	3.077 ± 0.001
Q [fC]	29.2 ± 0.9
$E_{\mathrm{RMS}}/\langle E \rangle$ [10^{-4}]	$\leq 2.4 \pm 0.1$
$\epsilon_{\mathrm{n},x}$ [nm]	86 ± 2
$\epsilon_{\mathrm{n},y}$ [nm]	113 ± 4

Table 5.1: Overview of beam parameters measured in the course of the energy spread compensation scheme. Note that the upper limit of the relative energy spread is equal to the convolved relative energy spread.

solenoid 6/7, the normalized emittance reads $\epsilon_{\mathrm{n},x} = (86 \pm 2)\,\mathrm{nm}$ in the horizontal and $\epsilon_{\mathrm{n},y} = (113 \pm 4)\,\mathrm{nm}$ in the vertical direction, respectively. An overview of the beam properties measured in the energy spread compensation scheme are listed in table 5.1. The mean beam energy $\langle E \rangle = (3.077 \pm 0.001)\,\mathrm{MeV}$ is in good agreement with the expected beam energy of 3.084 MeV in ASTRA simulations. This leads to the conclusion that even though the setpoint $\mathcal{E}_{\mathrm{b}} = 8.85\,\mathrm{MV/m}$ for the buncher gradient differs from the simulated value $\mathcal{E}_{\mathrm{b}} = 9.25\,\mathrm{MV/m}$, the machine settings are nevertheless close to the simulated cavity parameters. The discrepancy in the buncher gradient may most likely be ascribed to calibration errors of the cavities.

Finally, an exemplary detector image of a linearized longitudinal phase space measured with the energy spread compensation scheme is shown in the top right subplot figure 5.10 ($\phi_{\mathrm{b}} = \phi_{\mathrm{lin}}$). The detector image corresponding to the reference case for $\phi_{\mathrm{g}} = 0$ without the buncher cavity is shown in the top left subplot (see also figure 5.7). Both detector images share the same axes in ζ and $\delta\gamma/\langle\gamma\rangle$ and represent the particle distributions in the longitudinal phase space. Thus, it can clearly be seen that the electron bunch length is increased in stretcher mode as a result of the controlled expansion between gun and buncher cavity. The colorbar indicates the (normalized) pixel intensity values. The bottom row shows the cubic fit function (red line) for both cases, along with the relative slice energy deviation $\delta\gamma_{\mathrm{s}}/\langle\gamma\rangle$ (black dots). Compared to the reference case (left), the first and second order have been reduced significantly using energy spread compensation (right) and the characteristic S-shape of the now dominant third order contribution can clearly be seen. A close-up representation of the linearized distribution using $\delta\gamma_{\mathrm{s}}/\langle\gamma\rangle$ is shown in figure 5.11.

A number of datasets were recorded and analyzed. The machine setup and subsequent measurement procedure was repeatedly carried out with great success. A relative energy spread $E_{\mathrm{RMS}}/\langle E \rangle \leq 3 \cdot 10^{-4}$ was measured repeatedly in various measurement shifts.

A direct comparison of the measured energy spread and ASTRA simulations is difficult for several reasons. First and foremost, the relative energy spread strongly depends on the initial phase interval occupied in the gun cavity, i.e. on the pulse duration of the photocathode laser pulse. An experimental measurement of the laser pulse duration could not be performed. The pulse duration utilized in the presented simulations is itself based on an ASTRA simulation which produces the

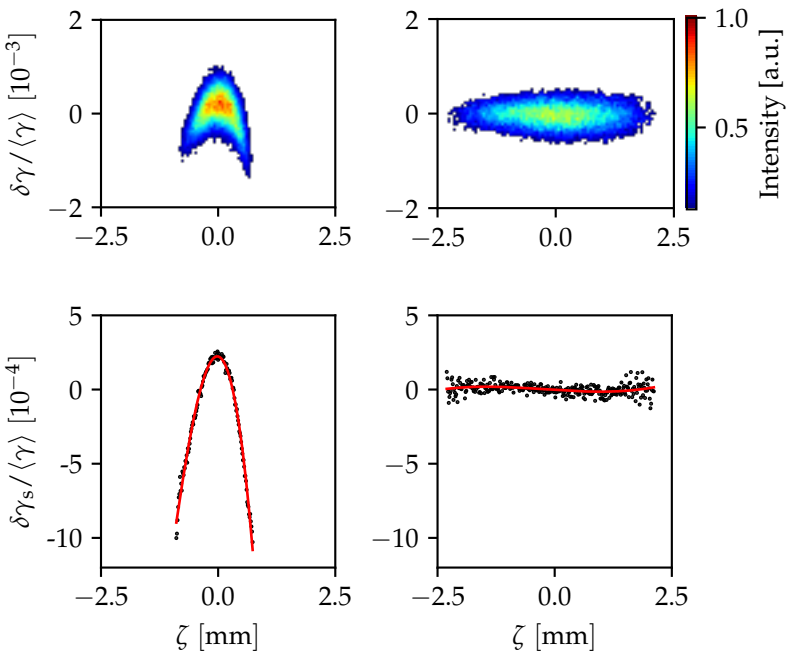

Figure 5.10: Exemplary depiction of the linearized longitudinal phase space (right) recorded as part of the dataset shown in figure 5.9. The reference case corresponding to standard operation mode at $\phi_g = 0$ and without the buncher cavity is also shown (left). The fit function (red) in the bottom subplots has been weighted with the respective pixel intensities of the detector images; the black dots mark the relative slice energy deviation $\delta\gamma_s/\langle\gamma\rangle$. For reasons of comparison, the bottom subplots share the same axis scaling. In the reference case shown on the left, the curvature in the longitudinal phase space can clearly be seen. In contrast to this, the curvature in the stretcher mode (right subplots) has nearly vanished, and the characteristic S-shape of the third order can be seen (bottom right). In addition to this, the bunch length has increased.

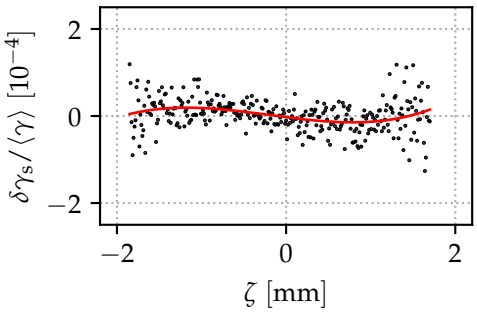

Figure 5.11: Close-up view of the bottom right subplot of figure 5.10 representing a linearized longitudinal phase space of the electron bunch. The black dots mark the relative slice energy deviation $\delta\gamma_s/\langle\gamma\rangle$, and the red line marks the fit through the corresponding detector image where the pixel intensities have been used as relative weights in the fit procedure. Since first and second order contributions have nearly been eliminated, the third order becomes dominant.

measured bunch length of $\xi_{\mathrm{RMS}} = (1.44 \pm 0.10)$ ps. Secondly, the recorded signal distribution on the spectrometer detector contains a contribution arising from the horizontal beam size. The reconstructed energy spread is therefore overestimated. Due to the fact that the the dipole not only causes an energy dependent deflection of the electrons but also has a focusing effect on the beam, it is not possible to use the vertical beam size on the spectrometer scintillator as an approximate estimate for the horizontal beam size.

Recently, a method of reconstructing the pure energy energy spread has been proposed in [114], which is based on measurements of the width of the particle distribution (in the dispersive direction) on the camera image of the spectrometer at different beam energies. By exploiting the different energy dependence of (horizontal) beam size and relative energy spread, the individual contributions can be deconvolved [114]. The potential implementation of this method at the REGAE spectrometer is currently being investigated. If the proposed method proves to be feasible, a reconstruction of the pure energy spread may be possible.

The magnitude of the pure relative energy spread can be estimated by an analytical calculation. The width of the measured distribution $x_{\mathrm{RMS,m}}$ along the dispersive axis on the detector screen contains contributions from the pure energy spread E_{RMS}, the intrinsic horizontal beam size x_{RMS} and the detector screen resolution R_{det}. Assuming these terms are uncorrelated, the pure relative energy spread is given by [114]

$$\frac{E_{\mathrm{RMS}}}{\langle E \rangle} = \sqrt{\frac{x_{\mathrm{RMS,m}}^2 - \frac{m_e c^2 \beta_x \epsilon_{\mathrm{n},x}}{\langle E \rangle} - R_{\mathrm{det}}^2}{D_x^2}}, \tag{5.8}$$

where D_x denotes the dispersion of the dipole spectrometer and the term $\frac{m_e c^2 \beta_x \epsilon_{\mathrm{n},x}}{\langle E \rangle}$ describes the contribution of the intrinsic beam size to the measured distribution width on the spectrometer screen (see [114] for details); β_x denotes the beta function at the position of the screen. Plugging in the measured dispersion from figure 3.5 and using the pixel calibration of the installed camera setup at the spectrometer as the resolution $R_{\mathrm{det}} = 12.9\,\mu\mathrm{m}$ yields a relative energy spread of $E_{\mathrm{RMS}}/\langle E \rangle = 1.6 \cdot 10^{-4}$ for an estimated horizontal beam size of $x_{\mathrm{RMS}} = 40\,\mu\mathrm{m}$ as taken from ASTRA simulations; note that the relation $x_{\mathrm{RMS}}^2 = \beta_x \epsilon_x$ has been used. This would be in good agreement with the relative energy spread of $E_{\mathrm{RMS,sim}}/\langle E \rangle = 1.5 \cdot 10^{-4}$ expected from ASTRA simulations with corresponding cavity and beam parameters.

An important aspect which must also be addressed is the fact that even in the measurement data with the best-case cavity configuration, the zero-crossing of the fit coefficients, i.e. $a_1 = 0$ and $a_2 = 0$, still occur at phase values which are approximately 0.60 deg apart from each other. Strictly speaking, this implies that an optimal linearization was not achieved, i.e. the experimentally determined ϕ_{lin} does not fully eliminate both first and second order contributions. A finer adjustment of the cavity parameters would lead to an even smaller energy spread.

Last but not least, the effect of fluctuations of the cavity rf parameters on the measurement results must be considered. Since the stretcher mode requires an extremely high precision with respect to the cavity settings, the results can be rather sensitive to fluctuations of the cavity parameters. For this purpose, a total

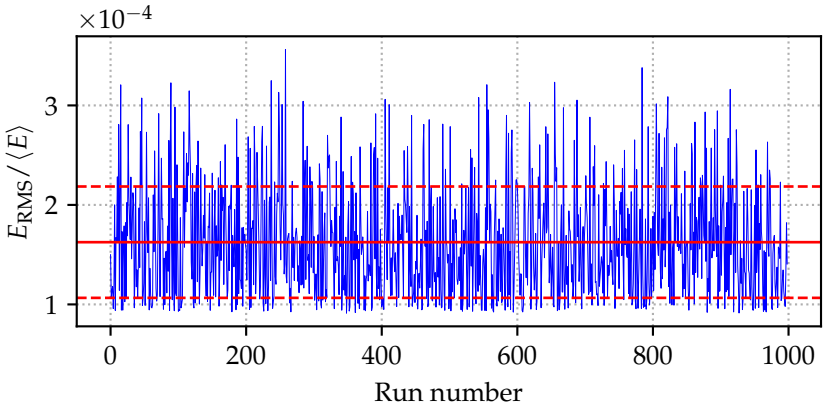

Figure 5.12: ASTRA simulations showing the effect of cavity rf fluctuations on the relative energy spread $E_{\mathrm{RMS}}/\langle E\rangle$ in the energy spread compensation scheme. The initial cavity configuration was set to the linearization parameters, and the cavity fluctuations were set to 0.08 % in amplitude and 0.06 deg in phase. The red line shows the mean relative energy spread of $\bar{E}_{\mathrm{RMS}}/\langle E\rangle = 1.6 \cdot 10^{-4}$, while the dashed red lines indicate the associated standard deviation.

of 999 ASTRA simulations runs were carried out with cavity parameter fluctuations based on the stability observations outlined in figure 4.8. Normal distributions of cavity amplitude and phase values with respective standard deviations of $0.08\,\% \cdot E_{\mathrm{g}}$, $0.5\,\% \cdot E_{\mathrm{b}}$ and 0.06 deg were generated and used as input parameters for the ASTRA simulations. The results of this study are shown in figure 5.12, where the relative energy spread $E_{\mathrm{RMS}}/\langle E\rangle$ is plotted for each separate ASTRA run. The energy spread compensation parameters $\mathcal{E}_{\mathrm{g}} = 80.00\,\mathrm{MV/m}$, $\phi_{\mathrm{g}} = 45.00\,\mathrm{deg}$, $\mathcal{E}_{\mathrm{b}} = 9.24\,\mathrm{MV/m}$ and $\phi_{\mathrm{b}} = -72.80\,\mathrm{deg}$ were used as initial cavity configuration. The relative energy spread for these cavity settings, using an initial pulse duration of 2.1 ps, reads $E_{\mathrm{RMS,sim}}/\langle E\rangle = 1.5 \cdot 10^{-4}$. As a result of the cavity fluctuations, the expected relative energy spread amounts to $E_{\mathrm{RMS,exp}}/\langle E\rangle = (1.6 \pm 0.6) \cdot 10^{-4}$. Both mean and associated standard deviation have been marked with red lines in figure 5.12.

In summary, only the convolved energy spread was accessible in direct measurements, which was equal to $E^{*}_{\mathrm{RMS}}/\langle E\rangle = (2.4 \pm 0.1) \cdot 10^{-4}$. Application of the method presented in [114] may allow the reconstruction of the deconvolved energy spread. An increased precision in tuning the cavity parameters would allow for a more exact linearization, characterized by $a_1 = a_2 = 0$, to be carried out. Elimination of the third order may also be possible, giving rise to an even smaller energy spread.

All in all, the measurement data confirm the applicability of the energy spread compensation scheme in stretcher mode operation of the REGAE beamline in terms of the longitudinal phase space evolution. It has been demonstrated that first and second order contributions in the longitudinal phase space distribution can be reduced significantly using energy spread compensation.

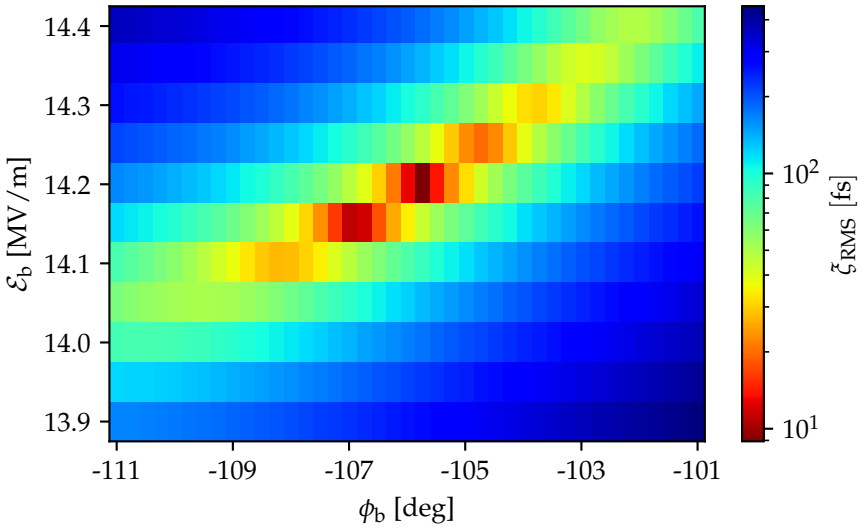

Figure 5.13: Two-dimensional parameter scan of the buncher gradient $\mathcal{E}_b$ and phase ϕ_b performed with ASTRA. The scan was performed around the (suspected) optimal bunch compression cavity configuration of the stretcher mode, where the second order vanishes and both bunch length and longitudinal emittance assume their minimum value at the desired focus position $z = 6\,\mathrm{m}$ inside the TDS. The color code marks the value of the RMS bunch length ξ_{RMS} for each buncher configuration within the scan interval. Logarithmic scaling has been applied to the color bar. Space charge forces were not included in these simulations.

5.2.2 Bunch Length Compression

Naturally, the findings presented above can also be transferred to the application of the stretcher mode to bunch length compression. Since the same generalities still apply, the basic considerations will only be outlined briefly. The measured uncompressed bunch length of $\bar{\xi}_{RMS} = (1.44 \pm 0.10)\,\mathrm{ps}$, obtained from previous measurements, will act as a point of reference for the indicated compression factors.

Figure 5.13 shows ASTRA simulations of the RMS bunch length at the position of the TDS ($z = 6\,\mathrm{m}$) for a selection of buncher settings around the optimum configuration. An initial laser pulse duration of 2.1 ps was used; space charge forces were excluded from these simulations. The pulse duration was taken from an ASTRA simulation which produces a bunch length that coincides with the measured value $\bar{\xi}_{RMS} = (1.44 \pm 0.10)\,\mathrm{ps}$. The existence of a minimal bunch length ($\xi_{RMS} = 8.17\,\mathrm{fs}$) can clearly be seen.

The first and second order contributions b_1 and b_2 to the longitudinal phase space distributions as a function of the buncher phase are shown in figure 5.14 for a refined selection of buncher gradient setpoints, along with the RMS bunch length. The gradient value is again indicated in the title of each respective subplot. The presented curves were taken from ASTRA simulations where space charge effects were neglected. A cubic fit has been applied to each distinctive particle distribution. This time, however, the energy deviation $\delta\gamma/\gamma_r$ was used as the domain. In other words, the function took on the form $f(\delta\gamma/\gamma_r) =$

$b_3(\delta\gamma/\gamma_r)^3 + b_2(\delta\gamma/\gamma_r)^2 + b_1\delta\gamma/\gamma_r + b_0 = \zeta(\gamma)$. As previously explained, a functional description in terms of the longitudinal coordinate, i.e. $\gamma = \gamma(\zeta)$ breaks down around in the region around the longitudinal focus. The reason for this is the occurrence of ambiguities in ζ.

As the buncher gradient approaches the optimal setpoint, the difference $\phi_b(b_1 = 0) - \phi_b(b_2 = 0)$ steadily decreases. In other words, the phase value where the first order vanishes and the phase value where the second order vanishes are moved closer together. From a physical point of view, tuning the buncher phase shifts the position of the bunch length minimum and the position of the longitudinal emittance minimum until both minima positions coincide at the same z-position in the beamline. Application of the linearization procedure yields $\mathcal{E}_g = 80.00\,\mathrm{MV/m}$ and $\phi_g = 34.10\,\mathrm{deg}$ as possible gun parameters, and $\mathcal{E}_b = 14.18\,\mathrm{MV/m}$ and $\phi_b = -106.41\,\mathrm{deg}$ as corresponding buncher parameters, respectively. Finding rf parameters during operation of the REGAE beamline which yield $b_1 = 0$ as well as $b_2 = 0$, combined with a sign change of the curvature, and verifying this through measurements can justifiably be regarded as proof of concept for the bunch compression scheme of the stretcher mode.

In the RMS based focus, the minimum bunch length is as low as 6.23 fs. However, the longitudinal focus in the sense of the linearization model, which results in $b_1 = b_2 = 0$, occurs at a slightly different phase setting. Here, the bunch length reads 10.07 fs. The position of the bunch length minimum is slightly shifted with respect to the position where the first and second order contributions are eliminated. The reason for this is that third order contributions are partially compensated by the nonzero linear term $b_1 \neq 0$ at the position of the bunch length minimum. This results in a shorter longitudinal extent compared to the bunch duration at the position of the linearized phase space distribution.

It is again instructive to observe the evolution of the particle distribution in the longitudinal phase space for a parameter region around the optimum cavity configuration. ASTRA simulations of the longitudinal phase space for a fixed buncher gradient, in this case $\mathcal{E}_b = 14.18\,\mathrm{MV/m}$, are depicted in figure 5.15 for a variety of buncher phase values. Space charge effects were again excluded in order to visualize the unperturbed internal bunch structure and its progression. The buncher phase has been varied in steps of 0.50 deg around $\phi_b = -106.41\,\mathrm{deg} = \phi_{lin}$.

The decrease in bunch length as the optimum cavity configuration is approached can clearly be observed, as all subplots again share the same axes. At $\phi_b = \phi_{lin}$ the distribution appears to resemble an upright line in the longitudinal phase space. Closer inspection of the distribution actually reveals an S-shape dominated by third order contributions. This has already been indicated previously in figure 5.2. At this point, the first and second order contributions nearly vanish completely. It should be noted that the particle distributions depicted in each subplot have been taken at $z = 6\,\mathrm{m}$, which coincides with the position of the longitudinal focus for the optimal cavity parameters and of the TDS. For deviations of the buncher phase value from the optimum, first and second order contributions reoccur and the bunch length may increase. In point of fact, the bunch length minimum changes its position. However, the minimum of the longitudinal emittance also changes its position. An increasing offset of the buncher

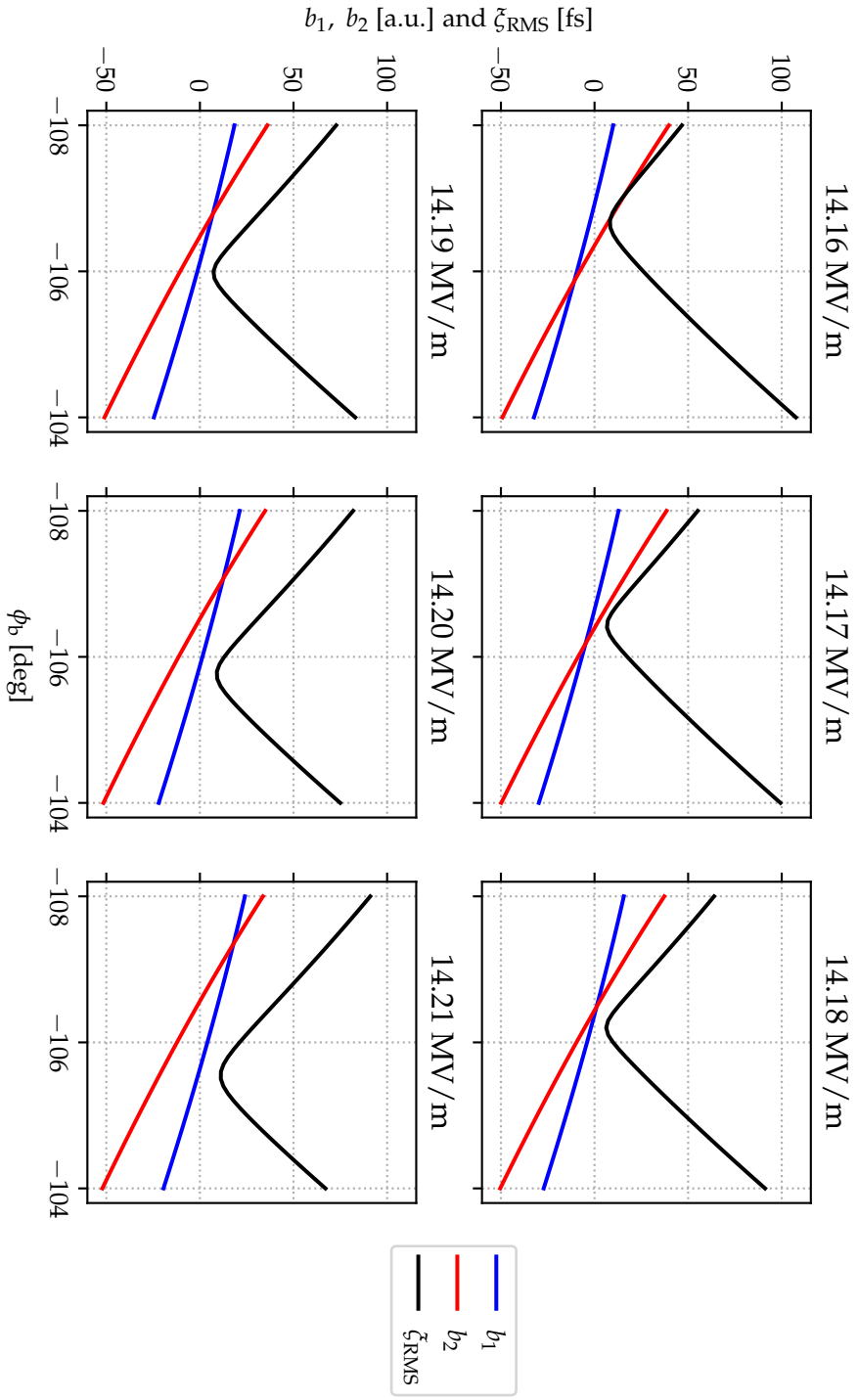

Figure 5.14: ASTRA simulations of the RMS bunch duration ξ_{RMS} (black) as well as first (blue) and second (red) order fit coefficients b_1 and b_2 of a cubic fit to the longitudinal phase space distribution resulting from buncher phase scans for a subset of buncher amplitude values. The values of the fit coefficients have been scaled to the order of magnitude of the bunch length. Space charge forces were not included in these simulations.

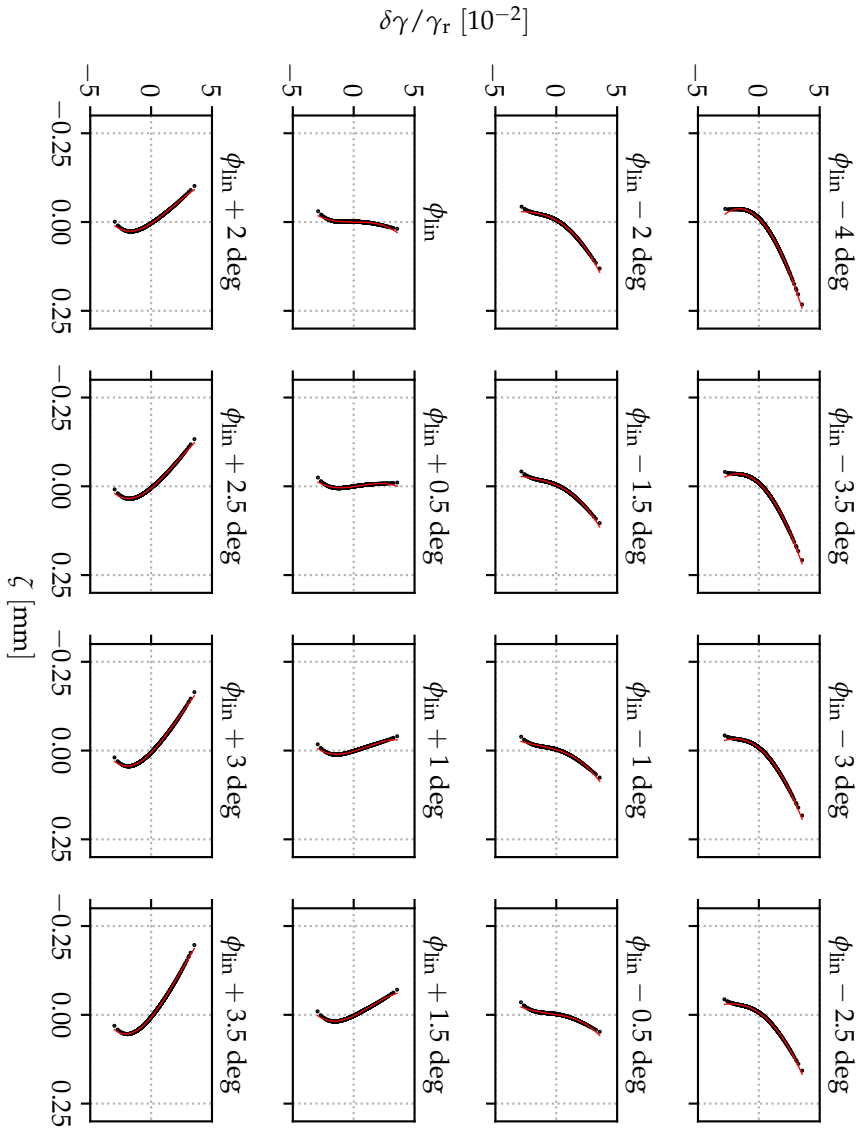

Figure 5.15: Longitudinal phase space simulated with ASTRA for a variety of buncher phase settings around ϕ_{lin} in the bunch compression scheme of the stretcher mode. A cubic fit (red) has been applied to each particle distribution (black).

phase with respect to the optimum causes a shift of bunch length minimum and longitudinal emittance minimum along the z-coordinate. The longitudinal focus in the sense of the linearization model is the characterized by the unique[2] buncher setting where the z-position of the bunch length minimum coincides with the z-position of the longitudinal emittance minimum. In this case, the expected bunch length is equal to $\xi_{\mathrm{RMS}} = 11.95\,\mathrm{fs}$ for an initial laser pulse duration of 2.1 ps and a bunch charge of $Q = 30\,\mathrm{fC}$. This would translate to a compression factor of about 120.

In principle, the machine setup procedure for bunch length compression is the same as for energy spread compensation, which makes sense since both schemes fall into the category of stretcher mode. Furthermore, the idea is once again to make use of the combination of TDS and dipole spectrometer to reconstruct the degree of curvature in the longitudinal phase space and thus experimentally determine the correct cavity rf parameters $\mathcal{E}_{\mathrm{b}}$ and $\phi_{\mathrm{b}} = \phi_{\mathrm{lin}}$.

After stepwise adjustment of the gun phase towards the required value $\phi_{\mathrm{g}} = 34.10\,\mathrm{deg}$, the buncher cavity was activated. In contrast to the procedure used for energy spread compensation, the TDS was switched on already at this point. The purpose of this was to easily visualize the development of the bunch length. Magnet lattice, dipole field and camera properties had to be adjusted continuously in order to keep the beam within the visible area of the scintillator screen. While the buncher cavity was still deactivated, the bunch length was so large that the streaked signal covered an area much larger than the imaged region of the scintillator screen of the dipole spectrometer. According to ASTRA simulations, the expected bunch length at the position of the TDS amounts to $\xi_{\mathrm{RMS}} \approx 9\,\mathrm{ps}$. This result makes sense since the gun cavity is operated at an expanding phase.

The buncher cavity caused a rapid decrease in bunch length as the parameters drew near the optimal settings. Once an approximate parameter range was established, the collimator at DDC1 was driven into the beam path to reduce dark current. In addition to this, some minor adjustments to the focusing solenoids in the REGAE front-end were put into effect. The attenuator in the UV segment of the photocathode laser system was fixed to produce a total bunch charge of $Q = 30\,\mathrm{fC}$. The combination of deflecting structure and dipole spectrometer enabled the reconstruction of the longitudinal phase space on the scintillator screen at the spectrometer setup. The amplitude of the TDS itself had to be increased to the maximum value in order to effectively visualize the curvature of the particle distribution in the longitudinal phase space.

Analogously to the measurement procedure described regarding the energy spread compensation scheme in section 5.2.1, a two-dimensional parameter scan of the buncher cavity rf parameters was carried out. For each fixed value of the buncher gradient, data were obtained for a variety of buncher phase setpoints. A total of 10 beam and background images were recorded at each distinct cavity configuration. Background subtraction and array centering was performed as described in section 4.2.2. Furthermore, the region growing algorithm was applied to the images. As a result of the relatively large area covered by the beam

2 It should be reminded that such a buncher setting exists for multiple gun settings in terms of second order correction, since the gun phase can be chosen somewhat arbitrarily. This "degree of freedom" vanishes for third (and higher) order corrections [16].

signal (compared to images taken during the energy spread compensation measurements), neighboring pixels were grouped together as written in the section describing the region growing algorithm. A bin width of 4 pixels proved to yield a satisfactory balance between required computation time and reconstruction accuracy and reliability. While the binning procedure does affect the reconstructed RMS size of the signal, the effect on the fit parameters is negligible. The reason for this is that the fit is weighted with the respective pixel intensities, and the potentially "false" pixels at the edge of the signal can be safely disregarded with respect to the high intensity pixels in the center of the beam, which are included independent of the bin width.

Since the cavity configuration was chosen to effectuate a linearization of phase space up to the second order, the first and second coefficients of the fit should vanish at the optimal cavity settings. The progression of the fit parameters for the longitudinal phase space evolution discussed above is shown in figure 5.16. In this particular dataset, the gradient of the buncher cavity was fixed at a setpoint of $\mathcal{E}_b = 13.87\,\mathrm{MV/m}$. The buncher phase was scanned in steps of 0.50 deg in a region around ϕ_{lin}. The bunch charge measured at DaMon2 was equal to $Q = 30\,\mathrm{fC}$. A polynomial function of the form $\zeta(x) = b_3x^3 + b_2x^2 + b_1x + b_0$ was fitted to the data of each phase space distribution of the detector images, where the fit variable x contains the energy γ of the particle and the pixel intensities were used as weights for the fit. An inverse functional representation $\gamma(\zeta)$ is not possible at this point because of the existing ambiguities around the longitudinal focus. The plot shows the first and second order fit coefficients b_1 and b_2 of the cubic fit to the longitudinal phase space distribution at the according buncher phase setpoint. More specifically, the plotted data constitute a cavity configuration where a compression of the electron bunch in the sense of the stretcher mode linearization model has been put into effect. This can be deduced from the fact that the zero-crossing phase values of the two datasets for b_1 and b_2 are nearly identical.

Figure 5.17 shows an exemplary evolution of the longitudinal phase space recorded in the course of the buncher parameter scan. The detector images are found in figure A.2 in the appendix A. The buncher phase setting is indicated in the title of the respective subplot, ϕ_{lin} is in accordance with figure 5.16. Due to the large positional jitter on the camera image, the calibration of the TDS was carried out at a lower output power of the amplifier and then scaled to the power used in the measurements. Nevertheless, the uncertainty of the calibration is on the level of 30 %.

The change in bunch length as a function of the cavity parameters, i.e. of the buncher phase ϕ_b, can be observed nicely. The applied fit (red) is plotted together with the energy slice centroid ζ_s (black); this corresponds to the same procedure carried out in context of figure 5.9 in the energy spread compensation scheme. The fit coefficients were used to analyze degree of curvature depending on the current cavity settings. A noteworthy observation is the fact that the curvature of the distribution clearly decreases as the buncher phase approaches the optimal setting in this specific cavity configuration. Here, the curvature appears to have vanished and the phase space distribution strongly resembles an upright line in this representation. The general progression of the measured longitudinal phase

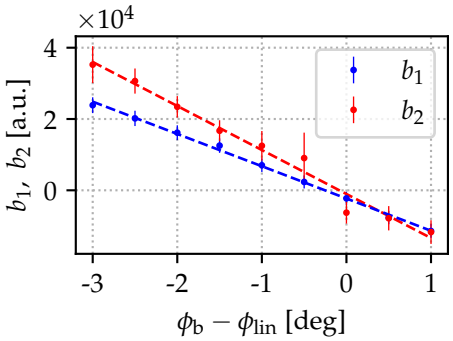

Figure 5.16: Experimental results of the bunch compression scheme of the stretcher mode. The first and second order fit coefficients b_1 and b_2 (indicated in blue and red, respectively) of a cubic fit to the corresponding particle distribution in the longitudinal phase space are shown as a function of the buncher phase $\phi_b - \phi_{lin}$ for a fixed buncher amplitude value, where ϕ_{lin} corresponds to the buncher phase which yields a nearly linearized distribution. The dashed lines mark a linear fit through the data, which constitutes the functional behavior expected from ASTRA simulations. The data were recorded at the eSpec of the REGAE beamline.

space evolution displays a high degree of similarity to the ASTRA simulations presented in figure 5.15

From a purely experimental and operational point of view, attention should be drawn to the fact that the determination of the actual cavity rf settings of the bunch compression scheme "in reality" proved to be far less straightforward compared to finding appropriate settings for energy spread compensation. Admittedly, this can already be adumbrated by comparing the two-dimensional buncher parameter scans simulated with ASTRA as portrayed in figures 5.4 and 5.13, respectively. It appears that the bunch compression scheme of the stretcher mode is more sensitive to the settings of both cavities, i.e. the subspace of parameters where linearization occurs and ultrashort bunch lengths can be achieved, is extremely small. In addition, the optimization must include the placement of the longitudinal focus at the desired position in the beamline. Coupled with the complications of having to continuously adjust various machine setting such as magnet lattice and TDS and spectrometer parameters during the search of the optimal cavity configuration, manually putting the bunch compression scheme into practice requires a great amount of effort. Further investigations geared towards an automated routine may aid the cause of establishing the stretcher mode as a possible standard operating mode of the beamline.

Following the experimental identification of appropriate cavity parameters, a measurement of the electron bunch length in stretcher mode operation of the REGAE beamline was performed. In principle, the actual method of measuring the bunch length with use of the TDS is identical to the other bunch length measurements outlined earlier in this thesis. The same machine setup procedure and data processing techniques were utilized.

The data of the bunch length measurement itself is depicted in figure 5.18; a thorough description of the analysis procedure has been given in earlier sections

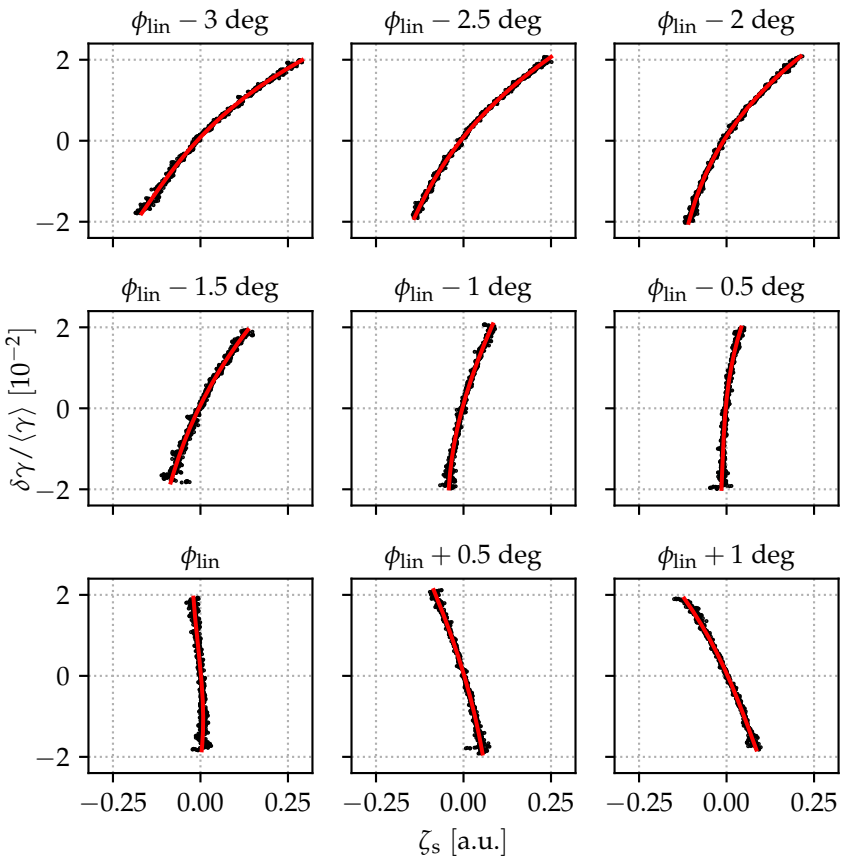

Figure 5.17: Measurement of the longitudinal phase space in dependency of the buncher phase in a region around the linearization setting ϕ_{lin} (with a step width 0.50 deg). The underlying images were recorded at the dipole spectrometer in combination with the TDS operated at maximum power. The images were processed with the binned region growing algorithm. A cubic fit (red) has been applied to each particle distribution where the pixel intensities have been used as weights. The black dots mark the mean longitudinal coordinate ζ_{s} for each energy slice.

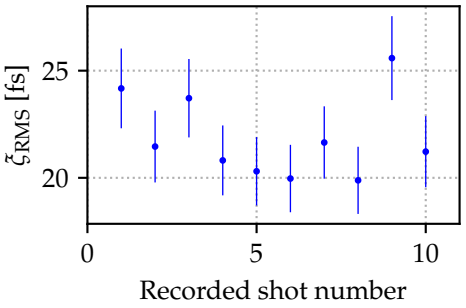

Figure 5.18: Measurement of the RMS bunch length ξ_{RMS} at the D2 detector setup using the bunch compression scheme of the stretcher mode at REGAE. The weighted mean bunch length is equal to $\bar{\xi}_{\mathrm{RMS}} = (21.86 \pm 1.82)$ fs.

Beam property	Measured value
$\langle E \rangle$ [MeV]	2.83 ± 0.04
Q [fC]	32.1 ± 0.6
ξ_{RMS} [fs]	21.86 ± 1.82
$\epsilon_{\mathrm{n},x}$ [nm]	127 ± 35
$\epsilon_{\mathrm{n},y}$ [nm]	140 ± 45

Table 5.2: Overview of beam parameters measured in the course of the bunch compression scheme.

of this thesis. The reconstructed bunch length ξ_{RMS} is shown for a total of 10 recorded shots. The resulting weighted mean value of all recorded shots yields a bunch length of $\bar{\xi}_{\mathrm{RMS}} = (21.86 \pm 1.82)$ fs.

Furthermore, a measurement of the emittance was carried out via a solenoid scan. The normalized transverse emittance reads $\epsilon_{\mathrm{n},x} = (127 \pm 35)$ nm and $\epsilon_{\mathrm{n},y} = (140 \pm 45)$ nm, respectively. The large relative uncertainties are a result of dark current jitter, which impacts the reconstructed RMS values due to significant pixel intensity variations occurring as a result of the background subtraction procedure. The main beam parameters are summarized in table 5.2.

Compared to the uncompressed bunch length, which was determined in previous measurements and found to be equal to $\bar{\xi}_{\mathrm{RMS}} = (1.44 \pm 0.10)$ ps, a compression factor of around 65 has been achieved. To put this into perspective, an previous measurement using the ballistic bunching mechanism for this laser pulse duration was evaluated, which yielded a weighted mean bunch length of $\bar{\xi}_{\mathrm{RMS}} = (133.38 \pm 2.19)$ fs. This implies a compression factor slightly above 10. Simulations with ASTRA predict a bunch length slightly below 130 fs. Considering the fact that the photocathode laser pulse duration could not be measured directly, the agreement between measurement and simulations is very good. In terms of effective compression, it is evident that the bunch compression scheme of the stretcher mode constitutes a significant improvement in comparison to the ballistic bunching mechanism.

Based on ASTRA simulations for a nominal laser pulse duration of 2.1 ps and a bunch charge of $Q = 30$ fC, the linearization method should produce a bunch with

a longitudinal extent of $\xi_{0,\mathrm{RMS}} = 11.95\,\mathrm{fs}$ in the focus in the sense of the model. Incorporating the TDS in simulations and replicating the measurement procedure in ASTRA would yield a reconstructed bunch length of $\xi_{\mathrm{RMS,sim}} = 14.10\,\mathrm{fs}$. Thus, the difference between mean measured value and simulated bunch length is equal to 7.76 fs. Therefore, within the scope of the measuring accuracy indicated by the respective uncertainty, the bunch length expected from simulations with the stretcher mode could not be measured. However, closer inspection of the phase space contribution depicted in figure 5.16 reveals that while the first and second terms have been greatly reduced, they do not entirely vanish at $\phi_\mathrm{b} = \phi_\mathrm{lin}$. Thus, these nonvanishing contributions offer a possible explanation for the slightly larger measured bunch length. In addition to this, it is possible that the laser parameters changed in the time between the measurement shift of the uncompressed bunch and the measurement shift dedicated to the stretcher mode. A longer nominal laser pulse duration could, in turn, lead to a larger expected bunch length in the longitudinal focus

Naturally, the utilized cavity parameters are subject to rf jitter around the nominal setpoints, which can have a significant impact on the linearization results. To quantify the effect of these fluctuations, a total of 999 ASTRA simulation runs have been performed, in which the cavity parameters were sampled from normal distributions with standard deviations of $0.08\,\% \cdot \mathcal{E}_\mathrm{g}$ and $0.5\,\% \cdot \mathcal{E}_\mathrm{b}$ in amplitude, 0.06 deg in gun phase and 0.12 deg in buncher phase, respectively. The standard deviations were calculated from the cavity fluctuations within a time interval of one hour. The optimal linearization settings $\mathcal{E}_\mathrm{g} = 80.00\,\mathrm{MV/m}$, $\phi_\mathrm{g} = 34.10\,\mathrm{deg}$, $\mathcal{E}_\mathrm{b} = 14.18\,\mathrm{MV/m}$ and $\phi_\mathrm{b} = -106.41\,\mathrm{deg}$ were used as mean values of the respective normal distributions. In this case, the longitudinal extent of the bunch reads $\xi_{\mathrm{RMS,sim}} = 13.80\,\mathrm{fs}$ (the TDS has been included in the simulation). Taking the jitter of gun and buncher cavity into account yields a mean expected bunch length of $\bar{\xi}_{\mathrm{RMS,sim}} = (24.94 \pm 16.84)\,\mathrm{fs}$, which is more than double the value for the nominal cavity configuration. In contrast to this, the minimum bunch length obtained in the jitter analysis is as small as 6 fs and thus below the bunch duration expected using the linearization settings. The reason for this is that while the linearization configuration eliminates the first and second order terms, the absolute bunch length minimum is assumed at slightly different cavity parameters which lead to a partial compensation of the third order by a nonzero linear term [17].

It is important to stress the fact that this strong bunch length fluctuation only occurs at the nominal focus position z_f. Previous numerical studies have shown that the overall minimum attainable bunch length is robust against cavity fluctuations, whereas the position of the longitudinal focus can, in fact, be subject to variations on the order of several mm [16].

Based on the measurements data analyzed and presented above, it can be concluded that the longitudinal extent of an electron bunch with ultralow charge was successfully compressed using the bunch compression scheme of the stretcher mode. First and second order contributions to the longitudinal phase space distribution have been reduced significantly using stretcher mode operation settings. Thus, it has been demonstrated that the stretcher mode may be utilized for the compression of electron bunches at few MeV beam energies.

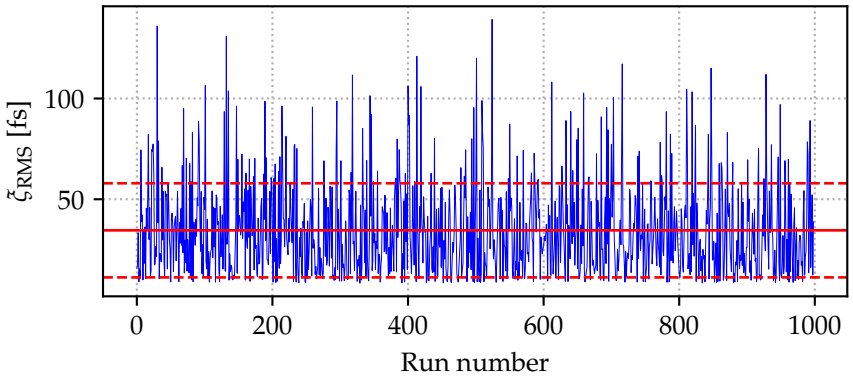

Figure 5.19: ASTRA simulations showing the effect of cavity rf fluctuations on the bunch length ζ_{RMS} at the nominal position $z = 6\,\mathrm{m}$ of the longitudinal focus. The cavity parameters and their standard deviations are specified in the text.. The red line shows the mean bunch length $\bar{\zeta}_{RMS} = 24.95\,\mathrm{fs}$, while the dashed red lines indicate the associated standard deviation. The mean bunch length is more than twice as large as the bunch length expected for ideal cavity settings.

5.3 SUMMARY

Based on previous work presented in [16, 17], a novel phase space linearization method, dubbed *stretcher mode*, has been applied to the REGAE beamline. Instead of using a higher harmonic structure, the linearization method at hand relies on the controlled evolution from the gun cavity to the buncher cavity, which are both operated at the same fundamental rf frequency. More specifically, cavity configurations have been determined which linearize the longitudinal phase space distribution by effectively eliminating first and second order contributions. This has been done for both axes of the longitudinal phase space, i.e. one set of parameters acts on the longitudinal coordinate ζ and minimizes the bunch length, and the other set of parameters acts on the energy coordinate γ and minimizes the energy spread of the bunch.

The transverse deflecting structure installed at the REGAE beamline was utilized in connection with the dipole spectrometer to record camera images representing the particle distribution of the electron bunch in the longitudinal phase space. A two-dimensional scan of the buncher cavity parameters was performed around the suspected optimal cavity settings, and the evolution of the phase space distribution was evaluated. It was successfully shown that cavity configurations exist where the first and second order coefficients of the cubic fit function, applied to the respective distribution, have vanished. Moreover, in the phase space evolution plots it can clearly be seen that curvature changes sign. This was accomplished for both bunch length compression and energy spread compensation schemes. The presented results act as a valid proof of concept for the novel linearization scheme.

In the course of the experimental data collected on the energy spread compensation scheme, measurements of the RMS energy spread itself were carried out and evaluated. For a bunch charge of 30 fC at a mean beam energy of $\langle E \rangle = 3.077\,\mathrm{MeV}$,

the best measured relative energy spread with use of the stretcher mode is equal to $E_{\mathrm{RMS}}/\langle E\rangle \leq (2.4 \pm 0.1) \cdot 10^{-4}$. Relative energy spreads below $3 \cdot 10^{-4}$ have repeatedly been obtained at various measurement shifts. Similarly, measurements of the bunch length in context of the bunch compression scheme were carried out. The phase space evolution verifies the applicability of the stretcher mode as a linearization method to compress the particle bunch, and the measured bunch length is equal to $\zeta_{\mathrm{RMS}} = (21.86 \pm 1.82)\,\mathrm{fs}$ for a charge of $Q = 30\,\mathrm{fC}$. This corresponds to a compression factor of about 65 with respect to the uncompressed bunch length. Compared to the compression factor of 10 using the ballistic bunching mechanism with identical nominal laser parameter, it is apparent that implementation of the stretcher mode offers a significant improvement.

In summary, the results obtained from the measurement data presented in this section verify the stretcher mode as a valid method of linearizing the longitudinal phase space. Further studies regarding the initial parameters of the photocathode laser pulse, optimization of cavity settings for higher order linearization and the reconstruction of bunch length and energy spread values confirming the expected minimum are planned for the future.

6 DISCUSSION AND OUTLOOK

The work presented in this thesis was focused on the operation of the transverse deflecting structure at the REGAE beamline and the demonstration of a novel method for linearizing the longitudinal phase space without the use of higher harmonic structures. A standard procedure for TDS operation and single-shot bunch length measurements at REGAE has been established and discussed. The TDS played an indispensable role for the pilot studies of the novel linearization technique as presented in the preceding section.

A reconstruction of the bunch length using the ballistic bunching mechanism, which only eliminates linear correlations in the longitudinal phase space, was successfully carried out. Given all the general assumptions regarding the beamline model in ASTRA, the agreement between measurement data and simulations is excellent. Thus, the REGAE TDS has been successfully integrated into the beamline and has proven to produce reliable measurement results. Using the ballistic bunching mechanism, a measured bunch length below 10 fs has been reported in an accelerator facility comparable to the REGAE beamline; however, the RMS pulse duration of the photocathode laser was intentionally reduced to 100 fs [20]. An appropriate adjustment of the pulse duration at REGAE should be able to produce similar results.

Apart from space charge, the attainability of even shorter bunches can be limited by nonlinear contributions in the longitudinal phase space. Pilot studies of a novel linearization method presented in [17] were performed in the course of this thesis, during which the TDS was used to measure and analyze the characteristics of the longitudinal phase space distribution. The linearization method is geared towards eliminating nonlinearities in the longitudinal phase space in order to further compress the electron bunch. Alternatively, the method can be used to compensate the energy spread accumulated in the gun cavity. It is based on the controlled expansion of the bunch between gun and buncher cavity, and thus referred to as *stretcher mode*.

Cavity rf parameters of the stretcher mode which eliminate first and second order phase space contributions have been determined for the REGAE beamline at $\mathcal{E}_g = 80\,\mathrm{MV/m}$ with the help of ASTRA simulations. This was carried out for both axes of the longitudinal phase space: one parameter set minimizes the bunch length, the other parameter set minimizes the energy spread. Measurement data portraying a longitudinal phase space distribution where the first and second order have vanished, and the third order becomes clearly visible, have been presented. Based on the results presented for the bunch compression and energy spread compensation schemes, the applicability of the stretcher mode as a method to linearize the longitudinal phase space has been demonstrated successfully.

Transmission electron microscopy (TEM) constitutes an exemplary potential application of energy spread compensation [6, 11]. Substituting the typical $\sim$ 100 keV electrons used in conventional TEMs [115, 116] with MeV beam

energies paves the way for single-shot picosecond resolution TEM by making use of reduced space charge effects [11, 117]. Here, an extremely small normalized transverse beam emittance ($\sim 10\,\mathrm{nm}$) is required, whereas the bunch length can be on the picosecond level ($\sim 10\,\mathrm{ps}$) to reduce space charge repulsion, which can cause emittance degradation. In this case, the chromatic aberrations caused by the energy spread of the beam can be a limiting factor of the microscope resolution. A relative energy spread smaller than 10^{-4} at a mean beam energy around 3 to 5 MeV would prove to be highly beneficial. According to [11], the aforementioned values are the requirements for a microscope capable of recording single-shot images with a spatio-temporal resolution of 10 nm and 10 ps, respectively. A relative energy spread $< 10^{-4}$ is feasible using the energy spread compensation scheme of the stretcher mode. The experimental verification of such a small relative energy spread at REGAE requires the deconvolution of the beam size contribution on the energy spectrometer [114].

In context of bunch length measurements performed with the TDS in stretcher mode, it should be noted that for ultrashort bunch durations on the order of 10 fs at few MeV beam energies, higher order effects such as transverse defocusing and bunch lengthening induced by the TDS can impact the bunch length reconstruction. Since these effects scale with $1/\gamma^2$ [44], the most effective reduction would be achieved by operating the beamline at a higher beam energy. However, the longitudinal shift caused by the buncher cavity in compression schemes based on the ballistic bunching mechanism scales with $1/\gamma^3$, thereby rendering the employment of beam energies $\gg 5\,\mathrm{MeV}$ ineffective for this type of compression. Operation of gun cavity at the design gradient of $100\,\mathrm{MV/m}$ would increase the mean beam energy and thus decrease higher order effects significantly, while preserving the viability of the ballistic bunching mechanism.

It has been conceptually shown that the stretcher mode can be used to produce bunch lengths below 1 fs; similarly, a relative energy spread below 10^{-5} has been obtained in simulations [17]. This translates to approximately an order of magnitude smaller than the measurement results presented in this work. To achieve such narrow distribution widths, the third order term in the longitudinal phase space distribution must be eliminated as well, which has yet to be verified by measurements. Apart from current limitations regarding the resolution of the electron beam diagnostics, this would require an increased level of control of the cavity rf parameters, as well as more stable operating conditions with respect to cavity rf fluctuations.

The bunch compression scheme of the stretcher mode may find its application in UED experiments, which are planned to be carried out at the REGAE beamline. UED requires ultrashort electron bunches on the femtosecond level or below to analyze fast atomic motions [2]. The electron beam is used to probe the target and can thus provide insights on the structural dynamics of matter. Applying the stretcher mode to produce ultrashort bunches may allow the investigation of processes on the sub-femtosecond level. However, this requires a stable and high-precision operation of the beamline and of the pump laser.

Two seemingly decisive deficits of the bunch compression scheme are given by the fact that the longitudinal focus is reached at a fixed position and that the compression itself is essentially based on the ballistic bunching mechanism,

which means that the stretcher mode is not feasible for high mean beam energies. However, these drawbacks can be nullified by injecting the linearized and compressed electron bunch into an accelerating structure, essentially exploiting the fact that both linear and nonlinear contributions scale inversely with higher powers of γ. It has been conceptually shown that this could freeze the longitudinal phase space distribution, which would prevent the expansion of the bunch and thus preserve the focused bunch structure in the entire subsequent beamline segment [17]. Naturally, this also requires careful tuning of the cavity parameters and delicate placement of the longitudinal focus at the optimal position in the accelerating structure.

Instead of an accelerating cavity, simulations have shown that a plasma-based acceleration scheme may be utilized, since the high field gradients in the order of GV/m would rapidly suppress the further evolution of higher order contributions [16]. While the external injection of a linearized and compressed electron bunch into a plasma wakefield has been demonstrated in simulations presented in [16], a detailed analysis of the associated parameters and experimental measurements are yet to be carried out.

At higher beam energies $\gg 5\,\mathrm{MeV}$, compression based on ballistic bunching is no longer feasible. Therefore, high energy accelerator facilities commonly resort to the use of magnetic chicanes, which are based on energy-dependent differences in path length. Measurements of sub-femtosecond bunch lengths using chicane compression have been previously reported [118]. In principle, it should be possible to incorporate the stretcher mode formalism in the matrix description of a magnetic chicane and thus (pre-)compensate nonlinear contributions, including longitudinal effects of the chicane, in the injector section, where the beam energy is sufficiently low [16]. Further studies are required to conclude on this aspect.

Apart from the reconstructed bunch length, the internal longitudinal structure of the linearized bunch may be of further interest, since the parameters space associated with bunches produced in stretcher mode is in uncharted territory. To resolve different characteristics between longitudinal slices, the slice length must be larger than the longitudinal resolution of the TDS. Several options exist for the purpose of resolving bunches with a longitudinal extent in the attosecond range. One possible course of action would be to simply increase the shear parameter of the currently installed TDS by using an amplifier with a greater output power. Another concept relies on the use of a sub-THz-driven dielectric lined waveguide (DLW) as a compact type of deflecting structure [119, 120]. Deflecting structures operated at a higher frequency intrinsically have a larger wave number k, which yields a larger shear parameter due to $S \propto k$. Numerical simulations have shown that such a (sub-)THz TDS should be capable of resolving sub-femtosecond bunches created using the stretcher mode [121]. Using a THz-based setup with a metal slit structure, a resolution of 2.5 fs has been demonstrated for a beam energy around 3 MeV [122]. A setup dedicated to the generation of THz radiation has been successfully tested and characterized in the laser laboratory at REGAE [121]. Implementation of the setup along with installation of the DLW into the REGAE target chamber in the beamline is planned to be carried out in 2021. Following the installation, the concept of the THz-driven DLW TDS will first need to be verified. The measurement data of the DLW TDS could be compared to and validated

by the results obtained with the REGAE TDS, which is already in operation and delivers reliable results.

In this regard, an improvement of the transverse emittance would directly improve the longitudinal resolution of the TDS, since the resolution scales explicitly with the transverse beam emittance. The benefits of a smaller emittance would also extend to the resolution of the energy spectrometer. In both cases, the resolution is proportional to the beam size at the position of the detector screen. At REGAE, the emittance of the beam is essentially defined by the intrinsic emittance of the cathode. A reduction of the emittance after the generation of the bunch is not feasible in the current accelerator setup, apart from using collimators to cut away fractions of the beam charge. Pushing the transverse beam emittance to even lower values requires adaptions of the photocathode laser system.

A number of improvements have been made to the photocathode laser system connected to the measurements performed within this thesis. This includes the integration of a beam stabilization setup, general alignment corrections, and the installation of a pinhole imaging setup to achieve a transverse uniform pulse shape and reduce the transverse emittance. This resulted in a normalized transverse emittance on the order of 30 nm in standard operation mode (without the buncher cavity). However, the overall performance of the laser system has not yet reached the desired level of reliability. An improved control over the pulse duration and profile shape would be beneficial. For instance, tuning the laser pulse to adopt a parabolic line charge density would, combined with a cylindrical uniform transverse shape, linearize the longitudinal space charge field in the electron bunch and thus reduce the influence of space charge effects in the longitudinal focus [10]. In this regard, the implementation of diagnostic elements dedicated to the measurement of the longitudinal pulse properties would be crucial. Fine-tuning longitudinal and transverse properties of the laser pulse can lead to an increased quality of the electron beam by further decreasing the beam emittance or space charge effects, which would consequently improve the resolution of both TDS and spectrometer.

Furthermore, it has been shown that the attainable bunch length in the longitudinal focus using the compression scheme of the stretcher mode depends on the initial pulse duration of the photocathode laser, and that an optimal setting exists which balances longitudinal emittance and space charge effects[16]. A possibility of tuning the laser pulse duration during beamline operation may give rise to even shorter bunches. Simulations with an optimized pulse duration for an extremely low bunch charge of 1 fC predict a bunch length below 100 as [16]. This is comparable to some of the shortest light pulses generated in attosecond science [123, 124]. Before utilizing attosecond electron bunches in UED or other experiments, the production and measurement of an electron bunch with such extreme properties must be carried out.

The bunch compression and energy spread compensation schemes of the stretcher may be put to use at accelerator research facilities where extreme longitudinal beam parameters are required. For instance, the possible application of bunch compression using the stretcher mode at the Berlin Energy Recovery Linac Project (BERLINPRO) [125] has been explored in numerical and analytical studies [126], where UED experiments are planned using a superconducting rf

cavity and a subsequent booster cavity. The beamline will also feature a transverse deflecting cavity to measure the longitudinal properties of the beam [127].

Measurement data presented in this thesis have explicitly shown that cavity settings determined in the stretcher mode can eliminate first and second order contributions in the longitudinal phase space distribution of an electron bunch. The compensation of the energy spread and the compression of the bunch length using the stretcher mode has been verified in measurements performed at the REGAE beamline. Thus, a proof of concept for the novel linearization method presented in [17] has been established based on experiments performed and evaluated in the course of this thesis.

A APPENDIX

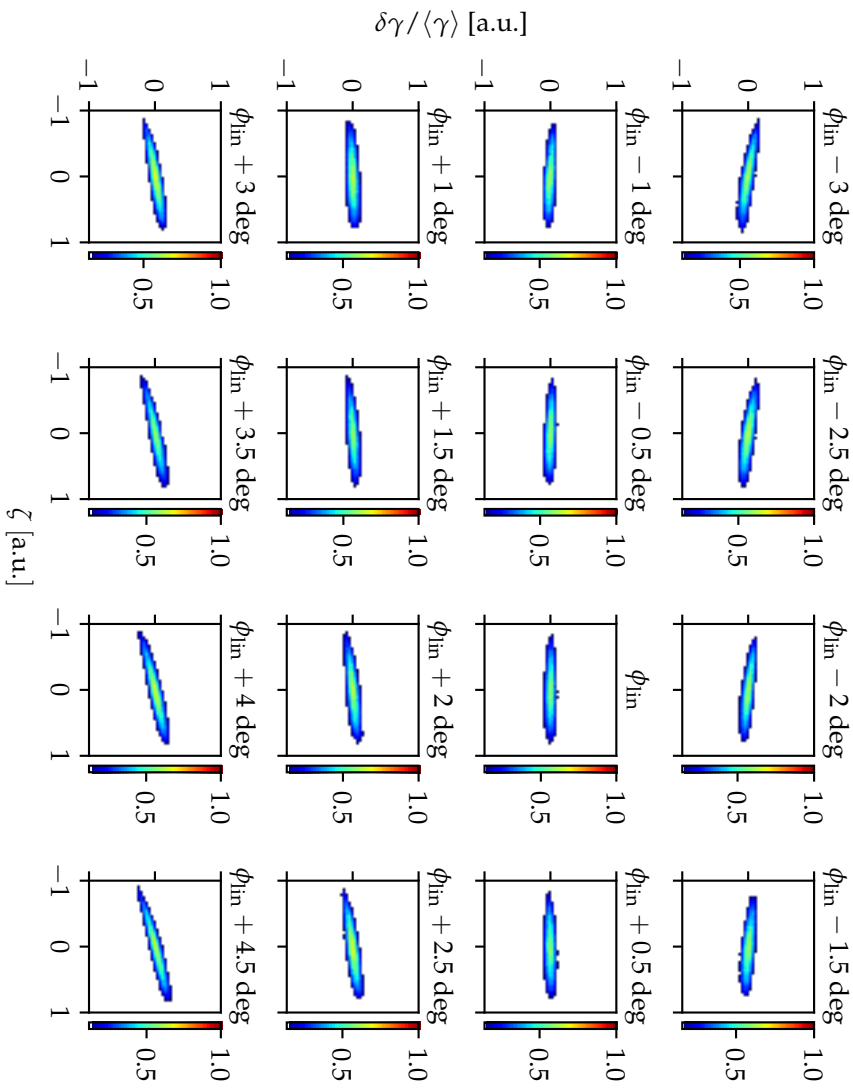

Figure A.1: Detector images recorded using the energy spread compensation scheme of the stretcher mode. The pixel intensity is indicated by the color bars. See figure 5.9 and the corresponding text for details.

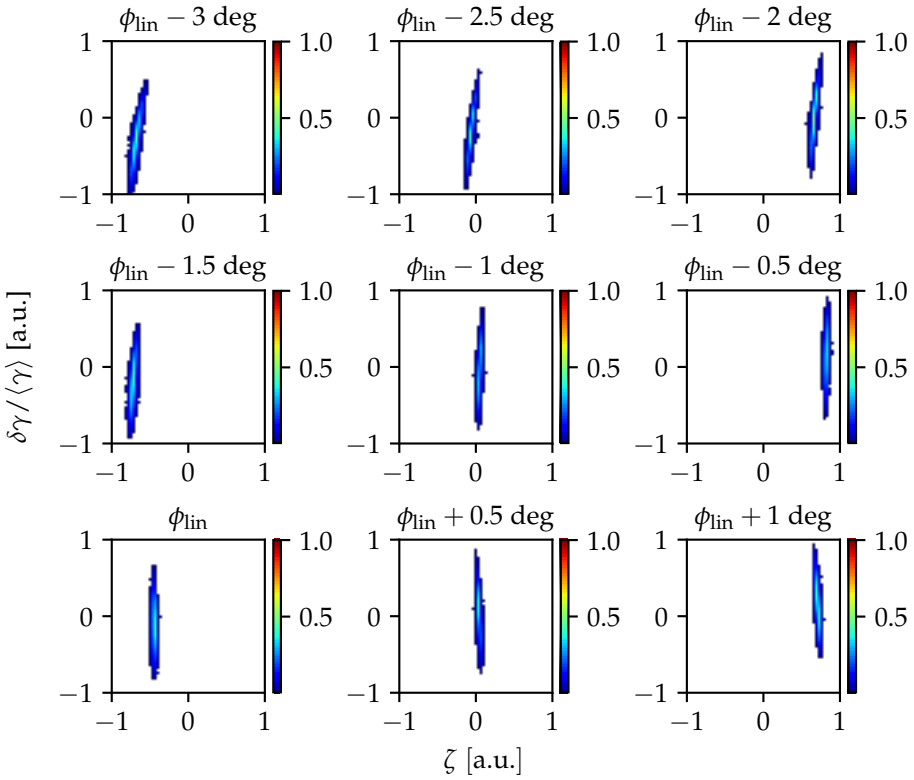

Figure A.2: Detector images recorded using the bunch compression scheme of the stretcher mode. The respective pixel intensity is indicated by the color bars.

BIBLIOGRAPHY

[1] John MJ Madey. "Stimulated emission of bremsstrahlung in a periodic magnetic field." In: *Journal of Applied Physics* 42.5 (1971), pp. 1906–1913.

[2] Jason R Dwyer, Christoph T Hebeisen, Ralph Ernstorfer, Maher Harb, Vatche B Deyirmenjian, Robert E Jordan, and RJ Dwayne Miller. "Femtosecond electron diffraction:'making the molecular movie'." In: *Philosophical Transactions of the Royal Society A: Mathematical, Physical and Engineering Sciences* 364.1840 (2006), pp. 741–778.

[3] Germán Sciaini and RJ Dwayne Miller. "Femtosecond electron diffraction: heralding the era of atomically resolved dynamics." In: *Reports on Progress in Physics* 74.9 (2011), p. 096101.

[4] RJ Dwayne Miller, Ralph Ernstorfer, Maher Harb, Meng Gao, Christoph T Hebeisen, Hubert Jean-Ruel, Cheng Lu, Gustavo Moriena, and German Sciaini. "Making the molecular movie': first frames." In: *Acta Crystallographica Section A: Foundations of Crystallography* 66.2 (2010), pp. 137–156.

[5] T Van Oudheusden, PLEM Pasmans, SB Van Der Geer, MJ De Loos, MJ Van Der Wiel, and OJ Luiten. "Compression of subrelativistic space-charge-dominated electron bunches for single-shot femtosecond electron diffraction." In: *Physical review letters* 105.26 (2010), p. 264801.

[6] Stephanie Manz et al. "Mapping atomic motions with ultrabright electrons: towards fundamental limits in space-time resolution." In: *Faraday Discuss.* 177 (0 2015), pp. 467–491.

[7] M. Hada et al. "REGAE: New Source for Atomically Resolved Dynamics." In: *Research in Optical Sciences*. Optical Society of America, 2012, JT2A.47.

[8] P Emma, J Frisch, and EA Krejcik. *A transverse rf deflecting structure for bunch length and phase space diagnostics, SLAC*. Tech. rep. Report No. LCLS-TN-00-12, 2000.

[9] V Paramonov, V Danielyan, K Floettmann, A Simonyan, and V Tsakanov. "Design, construction and tuning of an RF deflecting cavity for the REGAE facility." In: *Journal of Physics: Conference Series* 1238 (June 2019), p. 012069.

[10] K. Floettmann. "Generation of sub-fs electron beams at few-MeV energies." In: *Nuclear Instruments and Methods in Physics Research Section A Accelerators Spectrometers Detectors and Associated Equipment* 740 (Feb. 2014).

[11] RK Li and P Musumeci. "Single-shot MeV transmission electron microscopy with picosecond temporal resolution." In: *Physical Review Applied* 2.2 (2014), p. 024003.

[12] D Xiang, F Fu, J Zhang, X Huang, L Wang, X Wang, and W Wan. "Accelerator-based single-shot ultrafast transmission electron microscope with picosecond temporal resolution and nanometer spatial resolution." In: *Nuclear Instruments and Methods in Physics Research Section A: Accelerators, Spectrometers, Detectors and Associated Equipment* 759 (2014), pp. 74–82.

[13] R Brinkmann, K Flöttmann, J Rossbach, P Schmüser, N Walker, and H Weise. "TESLA-Technical Design Report, volume II." In: *DESY, March* (2001), pp. 2001–011.

[14] E Vogel et al. "Test and commissioning of the third harmonic RF system for FLASH." In: *Proceedings of IPAC* 10 (2010), pp. 4281–4283.

[15] K Flöttmann, T Limberg, and Ph Piot. "Generation of ultrashort electron bunches by cancellation of nonlinear distortions in the longitudinal phase space." In: *TESLA-FEL Report: TESLA-FEL* 6 (2001), p. 2001.

[16] Benno Zeitler. "Phase Space Linearization and External Injection of Electron Bunches into Laser-Driven Plasma Wakefields at REGAE." Dissertation, Universität Hamburg, 2017. Dissertation. Hamburg: Universität Hamburg, 2017.

[17] Benno Zeitler, Klaus Floettmann, and Florian Grüner. "Linearization of the longitudinal phase space without higher harmonic field." In: *Phys. Rev. ST Accel. Beams* 18 (12 Dec. 2015), p. 120102.

[18] regae.desy.de. [Online; accessed 17-March-2020].

[19] X. Lu, C. Tang, R. Li, Hoson To, G. Andonian, and P. Musumeci. "Generation and measurement of velocity bunched ultrashort bunch of pC charge." In: *Physical Review Special Topics - Accelerators and Beams* 18 (Mar. 2015).

[20] Jared Maxson, David Cesar, Giacomo Calmasini, Alexander Ody, Pietro Musumeci, and David Alesini. "Direct measurement of sub-10 fs relativistic electron beams with ultralow emittance." In: *Physical review letters* 118.15 (2017), p. 154802.

[21] Klaus Floettmann. *ASTRA - A Space Charge Tracking Algorithm*. https://www.desy.de/~mpyflo/. [Online; accessed 19-March-2020].

[22] Klaus Floettmann. *ASTRA - A Space Charge Tracking Algorithm*. User manual, Version 3.2. Mar. 2017.

[23] Bernhard Schmidt. *Accelerator Physics*. Lecture notes WS 2014/2015.

[24] J Rossbach and P Schmüser. "Basic course on accelerator optics." In: DESY-M-93-02 (Feb. 1993), 72 p.

[25] Helmut Wiedemann. *Particle accelerator physics; 4th ed.* Berlin: Springer, 2015.

[26] A.W. Chao. *Physics of Collective Beam Instabilities in High Energy Accelerators*. New York: John Wiley, 1993.

[27] Joseph Liouville. "Sur la théorie des équations transcendantes." In: *Journal de Mathématiques Pures et Appliquées* (3 1838), pp. 337–354.

[28] S Y Lee. *Accelerator Physics*. 3rd. WORLD SCIENTIFIC, 2011.

[29] Klaus Floettmann. "Some basic features of the beam emittance." In: *Phys. Rev. ST Accel. Beams* 6 (3 Mar. 2003), p. 034202.

[30] Klaus Floettmann. "Equivalence of Gouy and Courant-Snyder phase." In: *Physical Review A* 102.3 (2020), p. 033507.

[31] E.D Courant and H.S Snyder. "Theory of the alternating-gradient synchrotron." In: *Annals of Physics* 3.1 (1958), pp. 1–48.

[32] SG Anderson et al. "Velocity bunching of high-brightness electron beams." In: *Physical review special topics-accelerators and beams* 8.1 (2005), p. 014401.

[33] K Schindl. "CERN Accelerator School Intermediate accelerator physics, chapter Space charge." In: *CERN, DESY, Zeuthen, Germany* (2003), pp. 305–320.

[34] R A Akre, Lynn D. Bentson, Paul Emma, and Patrick Krejcik. "BUNCH LENGTH MEASUREMENTS USING A TRANSVERSE RF DEFLECTING STRUCTURE IN THE SLAC LINAC." In: *Proceedings of EPAC 2002*. Paris, France, 2002.

[35] C. Behrens and Ch. Gerth. "Measurement of the Slice Energy Spread Induced by a Transverse Deflecting RF Structure at FLASH." In: 10th European Workshop on Beam Diagnostics and Instrumentation for Particle Accelerators, Hamburg (Germany), 16 May 2011 - 18 May 2011. May 16, 2011.

[36] David Alesini, Giampiero [Di Pirro], Luca Ficcadenti, Andrea Mostacci, Luigi Palumbo, James Rosenzweig, and Cristina Vaccarezza. "RF deflector design and measurements for the longitudinal and transverse phase space characterization at SPARC." In: *Nuclear Instruments and Methods in Physics Research Section A: Accelerators, Spectrometers, Detectors and Associated Equipment* 568.2 (2006), pp. 488–502.

[37] C. Vaccarezza et al. "Slice Emittance Measurements at SPARC Photoinjector with a RF Deflector." In: *Conf. Proc.* C0806233 (2008), TUPC105.

[38] O. H. Altenmueller, R. R. Larsen, and G. A. Loew. "Investigations of Traveling-Wave Separators for the Stanford Two-Mile Linear Accelerator." In: *Review of Scientific Instruments* 35.4 (1964), pp. 438–442.

[39] W. K. H. Panofsky and W. A. Wenzel. "Some Considerations Concerning the Transverse Deflection of Charged Particles in Radio-Frequency Fields." In: *Review of Scientific Instruments* 27.11 (1956), pp. 967–967.

[40] M. Röhrs, B. Beutner, A. Bolzmann, C. Gerth, M. Hüning, and H. Schlarb. "Time-Resolved Measurements using the Transversely Deflecting RF-Structure LOLA at FLASH (DESY)." In: 37th ICFA Advanced Beam Dynamics Workshop on Future Light Sources, Hamburg (Germany), 15 May 2006 - 19 May 2006. May 15, 2006.

[41] C Behrens et al. "Few-femtosecond time-resolved measurements of X-ray free-electron lasers." In: *Nature communications* 5 (Apr. 2014), p. 3762.

[42] V. Paramonov, P. Orlov, and K. Floettmann. "Aberrations reduction in deflecting rf structures for transformation of particle distribution in the bunch." In: *Problems of atomic science and technology* 88 (Jan. 2013), pp. 67–71.

[43] Valentin V. Paramonov. "Effective RF Deflecting Structures for Bunch Rotation and Deflection." In: *Proceedings of RuPAC2016*. St. Petersburg, Russia, 2017.

[44] Klaus Floettmann and Valentin Paramonov. "Beam dynamics in transverse deflecting rf structures." In: *Physical Review Special Topics - Accelerators and Beams* 17 (Jan. 2014).

[45] Valentin Paramonov and Klaus Floettmann. *Fundamental characteristics of transverse deflecting field*. https://bib-pubdb1.desy.de/record/408721. [Online; accessed 28-March-2020]. 2018.

[46] Michael Roehrs, Christopher Gerth, Holger Schlarb, Bernhard Schmidt, and Peter Schmueser. "Time-resolved electron beam phase space tomography at a soft x-ray free-electron laser." In: *Phys. Rev. ST Accel. Beams* 12 (5 May 2009), p. 050704.

[47] Massimo Cornacchia and P. Emma. "Transverse to longitudinal emittance exchange." In: *Physical Review Special Topics - Accelerators and Beams* 5 (Aug. 2002).

[48] Daniel Marx, Ralph Assmann, U Dorda, Barbara Marchetti, and Frank Mayet. "Lattice considerations for the use of an X-band transverse deflecting structure (TDS) at SINBAD, DESY." In: *Journal of Physics Conference Series* 874 (May 2017).

[49] T. Tajima and J. M. Dawson. "Laser Electron Accelerator." In: *Phys. Rev. Lett.* 43 (4 July 1979), pp. 267–270.

[50] Benno Zeitler, Irene Dornmair, Tim Gehrke, Mikheil Titberidze, Andreas R. Maier, Bernhard Hidding, Klaus Flöttmann, and Florian Grüner. "Merging conventional and laser wakefield accelerators." In: *Laser Acceleration of Electrons, Protons, and Ions II; and Medical Applications of Laser-Generated Beams of Particles II; and Harnessing Relativistic Plasma Waves III*. Ed. by Eric Esarey, Carl B. Schroeder, Wim P. Leemans, Kenneth W. D. Ledingham, and Dino A. Jaroszynski. Vol. 8779. International Society for Optics and Photonics. SPIE, 2013, pp. 20–26.

[51] H. Hertz. "Ueber einen Einfluss des ultravioletten Lichtes auf die electrische Entladung." In: *Annalen der Physik* 267.8 (1887), pp. 983–1000.

[52] Matthias Hoffmann, Holger Kay, Uros Mavrič, Holger Schlarb, Christian Schmidt, Wojciech Jałmużna, Tomasz Kozak, and Adam Piotrowski. "Precision LLRF Controls for the S-Band Accelerator REGAE." In: *Proceedings, 4th International Particle Accelerator Conference (IPAC 2013): Shanghai, China, May 12-17, 2013*. 2013, WEPME008.

[53] Matthias Hoffmann. *Sub-10 fs RF Regulation at REGAE*. ARD Subtopic (ps-fs Electron and Photon Beams) ergänzen. Low Level Radio Frequency Workshop 2015, Shanghai (China), 3 Nov 2015 - 6 Nov 2015, Nov. 3, 2015.

[54] Max Hachmann. "Transverse emittance measurement at REGAE via a solenoid scan." MA thesis. Hamburg U., 2012.

[55] A.B. EL-KAREH and J.C.J. EL-KAREH. "Measurement of the Spherical Aberration of Various Electric and Magnetic Lenses." In: *Electron Beams, Lenses, and Optics*. Academic Press, 1970.

[56] Martin Reiser. "Beam Optics and Focusing Systems without Space Charge." In: *Theory and Design of Charged Particle Beams*. John Wiley and Sons, Ltd, 2008.

[57] M. Hachmann and K. Flöttmann. "Measurement of ultra low transverse emittance at REGAE." In: *Nuclear Instruments and Methods in Physics Research Section A: Accelerators, Spectrometers, Detectors and Associated Equipment* 829 (2016). 2nd European Advanced Accelerator Concepts Workshop - EAAC 2015, pp. 318–320.

[58] H. Delsim-Hashemi S. Bayesteh and K. Floettmann. "Beam Profile Monitors at REGAE." In: *Proceedings of IBIC 2013*. 2013, pp. 212–215.

[59] D. W. Cooke, K. J. McClellan, B. L. Bennett, J. M. Roper, M. T. Whittaker, R. E. Muenchausen, and R. C. Sze. "Crystal growth and optical characterization of cerium-doped Lu1.8Y0.2SiO5." In: *Journal of Applied Physics* 88.12 (2000), pp. 7360–7362.

[60] L. Pidol, A. Kahn-Harari, B. Viana, E. Virey, B. Ferrand, P. Dorenbos, J. T. M. de Haas, and C. W. E. van Eijk. "High efficiency of lutetium silicate scintillators, Ce-doped LPS, and LYSO crystals." In: *IEEE Transactions on Nuclear Science* 51.3 (June 2004), pp. 1084–1087.

[61] H. Bethe. "Zur Theorie des Durchgangs schneller Korpuskularstrahlen durch Materie." In: *Annalen der Physik* 397.3 (1930), pp. 325–400.

[62] S. Bayesteh. "Transverse electron beam diagnostics at REGAE." PhD thesis. University of Hamburg, 2014.

[63] M. Seebach D. Lipka J. Lund-Nielsen. "Resonator for charge measurement at REGAE." In: *Proceedings of IBIC 2013*. 2013.

[64] D. Lipka, W. Kleen, J. Lund-Nielsen, D. Noelle, S. Vilcins, and V. Vogel. "Dark Current Monitor for the European XFEL." In: 10th European Workshop on Beam Diagnostics and Instrumentation for Particle Accelerators, Hamburg (Germany), 16 May 2011 - 18 May 2011. JACoW, May 16, 2011.

[65] M. Seebach H. Delsim-Hashemi K. Floettmann and S. Bayesteh. "Charge monitors at the Relativistic Electron Gun for Atomic Exploration - REGAE." In: *Proceedings of IBIC 2013*. 2013.

[66] Klaus Flottmann. "Design and Performance of Printed Circuit Steering Magnets for the FLASH Injector." In: *Conf. Proc. C* 100523 (2010), MOPEB003.

[67] Donna Strickland and Gerard Mourou. "Compression of amplified chirped optical pulses." In: *Optics Communications* 56.3 (1985), pp. 219–221.

[68] https://lux.cfel.de/. [Online; accessed 15-April-2020].

[69] Nils Plambeck. "Vibration Measurements and Frequency Analyses for a TW-class Laser Transport Beamline." MA thesis. University of Hamburg, 2014.

[70] Sol M. Gruner, Mark W. Tate, and Eric F. Eikenberry. "Charge-coupled device area x-ray detectors." In: *Review of Scientific Instruments* 73.8 (2002), pp. 2815–2842.

[71] M. Hachmann, K. Flöttmann, T. Gehrke, and F. Mayet. "Design and characterization of permanent magnetic solenoids for REGAE." In: *Nuclear Instruments and Methods in Physics Research Section A: Accelerators, Spectrometers, Detectors and Associated Equipment* 829 (2016). 2nd European Advanced Accelerator Concepts Workshop - EAAC 2015, pp. 270–273.

[72] Tim Gehrke. "Design of Permanent Magnetic Solenoids for REGAE." MA thesis. University of Hamburg, 2015.

[73] Konstantin Krausert. "Development of Measurement Methods for Transverse Beam Profiles in the Micrometer Range at the REGAE Beamline." MA thesis. University of Hamburg, 2015.

[74] Yannis Papaphilippou. *Transverse Motion*. https://yannis.web.cern.ch/teaching/transverse.pdf. Teaching notes United States Particle Accelerator School. 2008.

[75] *Andor Technology Ltd. iXon EMCCD cameras*. https://andor.oxinst.com/products/ixon-emccd-cameras. [Online; accessed 04-May-2020].

[76] *Andor Technology Ltd. iXon 885*. http://www.bionovatec.com/wp-content/uploads/2014/04/iXon+885+spec+sheet.pdf. [Online; accessed 04-May-2020].

[77] G. F. Knoll. *Radiation Detection and Measurement*. 4th. John Wiley and Sons, 2010.

[78] Hossein Delsim-Hashemi. "Single Shot Transversal Profile Monitoring of Ultra Low Charge Relativistic Electron Bunches at REGAE." In: *5th International Beam Instrumentation Conference*. 2017, MOPG75.

[79] M. Hachmann. "High precision transverse emittance measurement for novel plasma accelerators at the REGAE Linac." PhD thesis. University of Hamburg, 2017.

[80] Dongliang Zhao and Gang Tan. "A review of thermoelectric cooling: Materials, modeling and applications." In: *Applied Thermal Engineering* 66.1 (2014), pp. 15–24.

[81] Don Edwards. "Notes on transit in deflecting mode pillbox cavity." In: (2007). [Fermilab Note].

[82] Valentin Paramonov. "Field distribution analysis in deflecting structures." In: *arXiv preprint arXiv:1302.5306* (2013).

[83] John David Jackson. *Classical electrodynamics*. John Wiley & Sons, 2007.

[84] H. Hahn. "Deflecting Mode in Circular Iris-Loaded Waveguides." In: *Review of Scientific Instruments* 34.10 (1963), pp. 1094–1100.

[85] Yves Garault. *Etude d'une classe d'ondes electromagnetiques guidees: les ondes EH, applications aux structures deflectrices pour les separateurs a onde progressive de particules relativistes*. Tech. rep. 1964.

[86] V Paramonov, L Kravchuk, and K Floettmann. "Standing wave RF deflectors with reduced aberrations." In: *Proc. RuPAC* (2012), p. 590.

[87] A. Skasyrskaya V. Paramonov I. Rybakov. *Physical specifications for technical design and construction of the standing wave RF deflector with the reduced abberrations for REGAE facility*. Tech. rep. Institute for Nuclear Research Russian Academy of Sciences, 2017.

[88] http://candle.am/. [Online; accessed 10-June-2020].

[89] https://mvs.desy.de/. [Online; accessed 29-July-2020].

[90] Michael Röhrs, Christopher Gerth, and Holger Schlarb. "Investigations of the longitudinal electron bunch structure at the flash linac with a transverse deflecting rf-structure." In: *Proc. FEL*. Vol. 6. 2006, p. 300.

[91] C. Behrens and C. Gerth. *The New LOLA/TDS Setup and Results on TDS-induced Energy Spread*. https://flash.desy.de/sites2009/site_vuvfel/content/e870/e85167/infoboxContent85168/FLASH_2011-June_Behrens.pdf. FLASH Seminar 2011. 2011.

[92] Michael Röhrs. "Investigation of the phase space distribution of electron bunches at the FLASH-linac using a transverse deflecting structure." PhD thesis. University of Hamburg, 2008.

[93] Andy Bolzmann. *Investigation of the longitudinal charge distribution of electron bunches at the VUV-FEL using the transverse deflecting cavity LOLA*. Tech. rep. DESY, 2005.

[94] Alexej Grudiev. *Design of compact high power rf components at x-band*. Tech. rep. 2016.

[95] Barbara Marchetti et al. "X-band TDS project." In: *Proc. IPAC'17* (2017), pp. 184–187.

[96] Florian Christie, Juliane Rönsch-Schulenburg, Siegfried Schreiber, and Mathias Vogt. "Generation of ultra-short electron bunches and FEL pulses and characterization of their longitudinal properties at FLASH2." In: *Proc. IPAC'17* (2017), pp. 2600–2603.

[97] Richard D'Arcy, Pau González Caminal, Vladyslav Libov, Alexander Aschikhin, and Jens Osterhoff. "Longitudinal phase space reconstruction at FLASHForward using a novel transverse deflection cavity, PolariX-TDS." In: *9th International Particle Accelerator Conference*. PUBDB-2018-05432. Forschung Linear Accelerator. 2018.

[98] P Craievich et al. "SUB-FEMTOSECOND TIME-RESOLVED MEASUREMENTS BASED ON A VARIABLE POLARIZATION X-BAND TRANSVERSE DEFLECTION STRUCTURE FOR SwissFEL." In: *Proc. 38th Int. Free Electron Laser Conf.(FEL'17)(Santa Fe, NM, USA)*. 2018, pp. 491–494.

[99] Daniel Marx, Ralph Assmann, Paolo Craievich, Ulrich Dorda, Alexej Grudiev, and Barbara Marchetti. "Longitudinal phase space reconstruction simulation studies using a novel X-band transverse deflecting structure at the SINBAD facility at DESY." In: *Nuclear Instruments and Methods in Physics Research Section A: Accelerators, Spectrometers, Detectors and Associated Equipment* 909 (2018), pp. 374–378.

[100] Daniel Marx, Ralph Aßmann, Ulrich Dorda, Barbara Marchetti, and Frank Mayet. "Lattice considerations for the use of an X-band transverse deflecting structure (TDS) at SINBAD, DESY." In: *Journal of Physics: Conference Series*. Vol. 874. 1. IOP Publishing. 2017, p. 012078.

[101] Daniel Marx, Ralph Aßmann, Paolo Craievich, Ulrich Dorda, Alexej Grudiev, Barbara Marchetti, et al. "Reconstruction of the 3D charge distribution of an electron bunch using a novel variable-polarization transverse deflecting structure (TDS)." In: *Journal of Physics: Conference Series*. Vol. 874. 1. 2017, p. 012077.

[102] Daniel Marx, Ralph Aßmann, Richard D'Arcy, and Barbara Marchetti. "Simulations of 3D charge density measurements for commissioning of the PolariX-TDS." In: *Journal of Physics: Conference Series*. Vol. 1067. 7. IOP Publishing. 2018, p. 072012.

[103] Florian Christie. "Generation of Ultra-Short Electron Bunches and FEL Pulses, and Characterization of Their Longitudinal Properties at FLASH2." PhD thesis. University of Hamburg, 2019.

[104] John Gordon Skellam. "A probability distribution derived from the binomial distribution by regarding the probability of success as variable between the sets of trials." In: *Journal of the Royal Statistical Society. Series B (Methodological)* 10.2 (1948), pp. 257–261.

[105] Youngbae Hwang, Jun-Sik Kim, and In So Kweon. "Difference-based image noise modeling using skellam distribution." In: *IEEE transactions on pattern analysis and machine intelligence* 34.7 (2011), pp. 1329–1341.

[106] Brad G Oswood. *EE261 - The Fourier Transform and its Applications*. https://see.stanford.edu/Course/EE261. Standford Engineering Everywhere Online Lecture Notes.

[107] L.G. Shapiro and G.C. Stockman. *Computer Vision*. Prentice Hall, 2001.

[108] Florian Lohl. "Measurements of the transverse emittance at the VUV-FEL." MA thesis. Hamburg U., 2005. DOI: 10.3204/DESY-THESIS-2005-014.

[109] Rolf Adams and Leanne Bischof. "Seeded region growing." In: *IEEE Transactions on pattern analysis and machine intelligence* 16.6 (1994), pp. 641–647.

[110] Pauli Virtanen et al. "SciPy 1.0: fundamental algorithms for scientific computing in Python." In: *Nature methods* 17.3 (2020), pp. 261–272.

[111] Wolfgang Demtröder. *Laserspektroskopie: Grundlagen und Techniken*. Springer-Verlag, 2007.

[112] Feichao Fu et al. "Demonstration of nonlinear-energy-spread compensation in relativistic electron bunches with corrugated structures." In: *Physical Review Letters* 114.11 (2015), p. 114801.

[113] Klaus Floettmann. "rf-induced beam dynamics in rf guns and accelerating cavities." In: *Physical Review Special Topics-Accelerators and Beams* 18.6 (2015), p. 064801.

[114] Eduard Prat, Philipp Dijkstal, Eugenio Ferrari, Alexander Malyzhenkov, and Sven Reiche. "High-resolution dispersion-based measurement of the electron beam energy spread." In: *Physical Review Accelerators and Beams* 23.9 (2020), p. 090701.

[115] Thomas LaGrange et al. "Single-shot dynamic transmission electron microscopy." In: *Applied Physics Letters* 89.4 (2006), p. 044105.

[116] ND Browning et al. "Recent developments in dynamic transmission electron microscopy." In: *Current Opinion in Solid State and Materials Science* 16.1 (2012), pp. 23–30.

[117] D Cesar et al. "Demonstration of single-shot picosecond time-resolved MeV electron imaging using a compact permanent magnet quadrupole based lens." In: *Physical review letters* 117.2 (2016), p. 024801.

[118] Jun Zhu, RW Assmann, M Dohlus, U Dorda, and B Marchetti. "Sub-fs electron bunch generation with sub-10-fs bunch arrival-time jitter via bunch slicing in a magnetic chicane." In: *Physical Review Accelerators and Beams* 19.5 (2016), p. 054401.

[119] Francois Lemery, K Flöttmann, T Vinatier, and RW Assman. "A transverse deflection structure with dielectric-lined waveguides in the sub-THz regime." In: *8th Int. Particle Accelerator Conf.(IPAC'17), Copenhagen, Denmark, 14â 19 May, 2017*. JACOW, Geneva, Switzerland. 2017, pp. 215–218.

[120] RL Kustom, Ch TM Chang, and JW Dawson. "Dielectric loaded waveguides as particle separators." In: *Nuclear Instruments and Methods* 87.1 (1970), pp. 19–27.

[121] Frank Mayet, Franz Kärtner, and Ralph Assmann. *Acceleration and phase space manipulation of relativistic electron beams in nano-and micrometer-scale dielectric structures*. Tech. rep. Beschleunigerphysik Fachgruppe MPY1, 2019.

[122] RK Li et al. "Terahertz-based subfemtosecond metrology of relativistic electron beams." In: *Physical Review Accelerators and Beams* 22.1 (2019), p. 012803.

[123] Eleftherios Goulielmakis et al. "Single-cycle nonlinear optics." In: *Science* 320.5883 (2008), pp. 1614–1617.

[124] Kun Zhao, Qi Zhang, Michael Chini, Yi Wu, Xiaowei Wang, and Zenghu Chang. "Tailoring a 67 attosecond pulse through advantageous phase-mismatch." In: *Optics letters* 37.18 (2012), pp. 3891–3893.

[125] Michael Abo-Bakr et al. "Status Report of the Berlin Energy Recovery Linac Project BERLinPro." In: *IPAC 2018: Proceedings of the 9th International Particle Accelerator Conference*. 2018, pp. 4127–4130.

[126] Simon Koch. “Numerical and analytical optimization of the bERLinPro SRF photoinjector and booster for short pulse applications.” MA thesis. Humboldt-Universität zu Berlin, 2018.

[127] Georgios Kourkafas, Thorsten Kamps, Axel Neumann, and Bjoern Keune. “Transverse Deflecting Cavity for Longitudinal Beam Diagnostics at BERLinPro.” In: *29th Linear Accelerator Conf.(LINAC'18), Beijing, China, 16-21 September 2018*. JACOW Publishing, Geneva, Switzerland. 2019, pp. 875–878.

ACKNOWLEDGMENTS

First and foremost I would like to thank my supervisors Prof. Dr. Florian Grüner and Prof. Dr. Wolfgang Hillert for giving the opportunity to work on the linearization project at REGAE in the course of my Ph.D. thesis.

In addition, I would like to express my deepest gratitude to Dr. Benno Zeitler for the constant support and guidance he provided throughout my work. It has been a pleasure. In this context, I would also like to thank the REGAE mastermind Dr. Klaus Flöttmann for letting me tap into his vast knowledge on accelerator physics.

In this context, I would like to thank Dr. Max Hachmann for the countless shifts we shared. I daresay it was (almost) always enjoyable. I would also like to thank Dr. Hossein Delsim-Hashemi for his knowledge and support on the diagnostic elements of REGAE. Furthermore, I am thankful to both Max and Hossein for their down-to-earth and realistic approach to solving all sorts of machine- and beamtime-related problems. Naturally, I also want to thank the other members of the REGAE team, especially Sadegh Bakhtiarzadeh for his work on the laser system.

For the design of the upgraded UV section of the photocathode laser system and seemingly infinite knowledge on lasers in general, I would also like to thank Dr. Chris Werle of the LUX team. My thanks extend to all members of the LUX team who assisted with the installation of the Laser Transport Beamline.

I would also like to thank the technical groups at DESY and UHH who helped with the beamline upgrade and general upkeep of REGAE. I especially want to thank Nils Plambeck and the MVS team for allowing me to gather hands-on experience in vacuum works.

Moreover, I want to thank a number of people who are not directly linked to my work at REGAE. I am very grateful to have studied with my Physikus crew. I also want to thank every member of the Oldschool group for their diversity and open-mindedness. I truly believe that we can always count on each other - no matter what.

For providing a much needed balance to the trials and tribulations in the life of a physicist, I would like to thank the participants of the many productions of the University Players theater group I was involved in. I also wish to thank my Badminton-friends at the UHH Hochschulsport. For the numerous enjoyable evenings I also want to thank my Doppelkopf-crew Oliver, Roberto, Matthias and Emil.

Lastly, I would like to thank my loving family, especially my parents Niki and Werner, as well as my sister Serena. I would also like to thank my girlfriend Sophie. Thank you all for your love and support.